IMPROVEMENT OF ELECTROCARDIOGRAPHIC IMAGING RECONSTRUCTIONS: A PHYSICS-GUIDED AI APPROACH AND AN EFFICIENT METHOD FOR TRAINING DATA REDUCTION

A THESIS SUBMITTED TO
THE GRADUATE SCHOOL OF NATURAL AND APPLIED SCIENCES
OF
MIDDLE EAST TECHNICAL UNIVERSITY

BY

KUTAY UĞURLU

IN PARTIAL FULFILLMENT OF THE REQUIREMENTS
FOR
THE DEGREE OF MASTER OF SCIENCE
IN
ELECTRICAL AND ELECTRONICS ENGINEERING

AUGUST 2023

Approval of the thesis:

IMPROVEMENT OF ELECTROCARDIOGRAPHIC IMAGING RECONSTRUCTIONS: A PHYSICS-GUIDED AI APPROACH AND AN EFFICIENT METHOD FOR TRAINING DATA REDUCTION

submitted by **KUTAY UĞURLU** in partial fulfillment of the requirements for the degree of **Master of Science in Electrical and Electronics Engineering Department, Middle East Technical University** by,

Prof. Dr. Halil Kalıpçılar
Dean, Graduate School of **Natural and Applied Sciences** _____

Prof. Dr. İlkay Ulusoy
Head of Department, **Electrical and Electronics Engineering** _____

Assoc. Prof. Dr. Yeşim Serinağaoğlu Doğrusöz
Supervisor, **Electrical and Electronics Engineering, METU** _____

Examining Committee Members:

Prof. Dr. Gözde Bozdağı Akar
Electrical and Electronics Engineering, METU _____

Assoc. Prof. Dr. Yeşim Serinağaoğlu Doğrusöz
Electrical and Electronics Engineering, METU _____

Prof. Dr. Tolga Çukur
Electrical and Electronics Engineering, Bilkent University _____

Date:24.08.2023

I hereby declare that all information in this document has been obtained and presented in accordance with academic rules and ethical conduct. I also declare that, as required by these rules and conduct, I have fully cited and referenced all material and results that are not original to this work.

Name, Surname: Kutay Uğurlu

Signature :

ABSTRACT

IMPROVEMENT OF ELECTROCARDIOGRAPHIC IMAGING RECONSTRUCTIONS: A PHYSICS-GUIDED AI APPROACH AND AN EFFICIENT METHOD FOR TRAINING DATA REDUCTION

Uğurlu, Kutay
M.S., Department of Electrical and Electronics Engineering
Supervisor: Assoc. Prof. Dr. Yeşim Serinağaoğlu Doğrusöz

August 2023, 132 pages

Non-invasive Electrocardiographic imaging (ECGI) holds promise as a tool that employs distant measurements of body surface potential (BSP) to reconstruct potential distributions on the heart's surface. Due to the nature of the human thorax, the cardiac potentials get smoothed and attenuated. Thus, estimating the epicardial potentials from the BSPs is an ill-posed problem. Hence, regularization is needed.

Novel regularization techniques require training data to estimate prior distribution and the common approach is using the whole dataset. The first study in this thesis shows that it is possible to achieve comparable performance to that of all dataset by carefully selecting a small subset of data in the Bayesian Maximum A Posteriori (MAP) solution of the inverse problem. The study proposes two methods on beat selection order and training set expansion termination. The point where the condition number of the covariance stops improving can represent the whole training set's performance. 26.9% of the dataset resulted in significantly similar metric distributions (p=0.59). The study showed that condition number provides insight about the sufficiency of the training data.

The second study uses neural networks (NNs) to learn the implicit prior by solving the problem iteratively with analytical solutions and NN-based denoiser. The method employs decoupled spatiotemporal NN blocks. This outperforms MAP, resulting in more consistent performance. The localization error of the 17 test beats in median (IQR) representation was 14.70(16.60) mm for the zero-order-Tikhonov, 17.00(10.54) mm for the MAP using the same data, and 5.80(8.60) mm for the proposed method, resulting in 38.5% improvement.

Keywords: Electrocardiographic imaging, deep learning, neural networks, training data, Bayesian MAP

ÖZ

ELEKTROKARDİYOGRAFİK GÖRÜNTÜLEME GERİÇATIMLARININ İYİLEŞTİRİLMESİ: FİZİK TABANLI YAPAY ZEKA YAKLAŞIMI VE EĞİTİM VERİSİNİN İNDİRGENMESİ İÇİN ETKİN BİR YÖNTEM

Uğurlu, Kutay
Yüksek Lisans, Elektrik ve Elektronik Mühendisliği Bölümü
Tez Yöneticisi: Doç. Dr. Yeşim Serinağaoğlu Doğrusöz

Ağustos 2023 , 132 sayfa

Girişimsiz Elektrokardiyografik görüntüleme (EKGG), vücut yüzey potansiyellerini (VYP) kullanarak kalp yüzeyindeki potansiyel dağılımlarını yeniden oluşturan bir araçtır. İnsan toraksının doğası gereği, kalp potansiyelleri yumuşar ve küçülür. Bu nedenle, VYPlerden kalp potansiyellerin kestirimi kötü konumlanmış bir problemdir. Bu nedenle, klinik olarak anlamlı kalp sinyalleri oluşturmak için düzenlileştirilme gerekir.

Yeni düzenlileştirme teknikleri, önsel dağılımın kestirimi için eğitim verisine ihtiyaç duyar ve yaygın yaklaşım veri kümesinin tamamını kullanmaktır. Bu tezdeki ilk çalışma, Bayes Maksimum A Posteriori (MAP) çözümünde küçük bir veri kümesiyle, tüm veri kümesinin performansıyla karşılaştırılabilir performans elde etmenin mümkün olduğunu göstermektedir. Çalışma, eğitim verilerinin nasıl seçileceği ve veri eklemenin durdurulacağı zaman hakkında yöntemler önermektedir. Kovaryans matrisinin koşul sayısının iyileşmeyi durdurduğu verinin, tüm eğitim setinin performansını

yeterince temsil ettiği gösterilmiştir. Veri kümesinin %26.9u, istatistiksel olarak benzer performans metrik dağılımlarına yol açmıştır (p=0.59). Çalışma, Gauss dağılımlı MAP bağlamında, önerilen metriğin, eğitim verisi içeriği hakkında bilgi sağladığını göstermiştir.

İkinci çalışma, yapay sinir ağlarını (YSA) kullanarak örtük önsel dağılımı öğrenmeyi amaçlar. Bu yöntemde, Tikhonov eniyileme ifadesi, analitik çözüm ile YSA temelli gürültü azaltma adımlarıyla çözülür. Çözüm, uzamsal ve zamansal yönlere ayrılmış YSA bloklarından oluşur. Bu, MAP çözümünü geride bırakmakta ve performans metriklerinin daha yoğun dağılmasına yol açmaktadır. Yerseme hatası, 17 test verisi ve sıfırıncı derece Tikhonov çözümü için ortanca (çeyrekler arası dağılım) şeklinde, mm cinsinden 14.70 (15.80), aynı eğitim verisini kullanan MAP çözümü için 17.31 (10.54) ve önerilen çözüm için 10.65 (6.52) olarak hesaplandı ve MAPe kıyasla atım odağını bulmada %38.5 iyileşme sağladı.

Anahtar Kelimeler: Elektrokardiyografik görüntüleme, derin öğrenme, sinir ağları, eğitim verisi, Bayes MAP

To my family

ACKNOWLEDGMENTS

Firstly, I would like to express my sincere gratitude to my family, who have supported my progress throughout my entire life. Special thanks go to the newest member of my family, İpek, my oldest friend and now my wife. Without her unwavering emotional support, I would not have been able to complete this work.

I am deeply grateful to my supervisor, Assoc. Prof. Yeşim Serinağaoğlu Doğrusöz, for her invaluable guidance, unwavering support, and understanding that she has demonstrated over the course of three years. Under her supervision, I had the privilege of acquiring vast knowledge. Besides my supervisor, I would like to thank Prof. Gözde Bozdağı Akar, for her contributions and insightful comments that guided me.

I extend my appreciation to my colleague, Nika Rasoolzadeh, for the time and effort she devoted to assisting me and being a friend to share this journey with me.

The works presented in this thesis have received support from the Turkish Scientific and Technological Research Council of Turkey (TÜBİTAK) through research grants numbered 118E244, 120N200, and 221N175.

TABLE OF CONTENTS

LIST OF TABLES

TABLES

LIST OF FIGURES

FIGURES

LIST OF ABBREVIATIONS

2D	2 Dimensional
3D	3 Dimensional
AF	Atrial fibrillation
AI	Artificial Intelligence
ANN	Artificial Neural Network
AV	Atrio-ventricular
BEM	Boundary Element Method
BSP	Body surface potential
BSPM	Body surface potential mapping
CNN	Convolutional Neural Network
CT	Computerized Tomography
ECG	Electrocardiography
ECGI	Electrocardiographic Imaging
EGM	Electrogram
FDM	Finite Difference Method
FEM	Finite Element Method
FVM	Finite Volume Method
GNN	Graph Neural Networks
i.i.d.	Independent and identically distributed
ISTA	Iterative shrinkage-thresholding algorithm
IQR	Inter-quartile range
LR	Learning rate
MAP	Maximum A Posteriori

MFS	Method of Fundamental Solutions
MRI	Magnetic Resonance Imaging
PAC	Premature Atrial Contractions
PCA	Principal Component Analysis
PDE	Partial Differential Equation
PVC	Premature Ventricular Contractions
SA	Sinoatrial
SVD	Singular Value Decomposition
TSVD	Truncated singular value decomposition
TTLS	Truncated total least squares

CHAPTER 1

INTRODUCTION

1.1 Motivation and Problem Definition

According to the World Health Organization (WHO), cardiovascular diseases (CVDs) are the leading cause of mortality [14]. In 2019, the CVDs accounted for the 32% of all global deaths, adding up to 17.9 millions. Out of 17 million premature deaths, that are deaths under age of 70, 38% were due to the CVDs. A more recent statistic from Center for Disease Control and Prevention [15] illustrates that 695,000 people died in United States from CVDs in 2021. accounting for 20% of all deaths. Moreover, it shows that one person dies in every 33 seconds from CVDs in US.

Imaging the electrical activity of the heart is a crucial step towards the prognosis, diagnosis and the treatment. 12-lead electrocardiography is the commonly used technique in clinics for diagnosis and treatment. It provides 12 measurement derived from 9 electrodes placed on the surface on the torso. However, it suffers from the attenuation and smoothing, resulting in low sensitivity for the diagnosis of myocardial infarctions (59%), subendocardial myocardial infarction (55%) and transmural infarction (63%) [16]. On the other hand, invasive techniques such as catheter electrodes are used for measurement of the intracardiac electrical activity followed by a surgical operation, such as RF ablation of the arrhythmogenic substrate for the treatment of many arrhytmias [17]. Although this method provides accurate information, it is a medical operation that costs more in time and requires the intervention by skilled medical professionals. Electrocardiographic imaging (ECGI) is a non-invasive imaging tool that aims to treat such CVDs by solving the inverse problem of electrocardiography and reconstructing different pattern that shed light onto the electrical behavior of the

heart. The aim is to estimate the epicardial potential distribution of the heart from the measurements taken from torso electrodes and provide relevant information acquired via post-processing to the physicians before the surgical operation depending on the type of the disease.

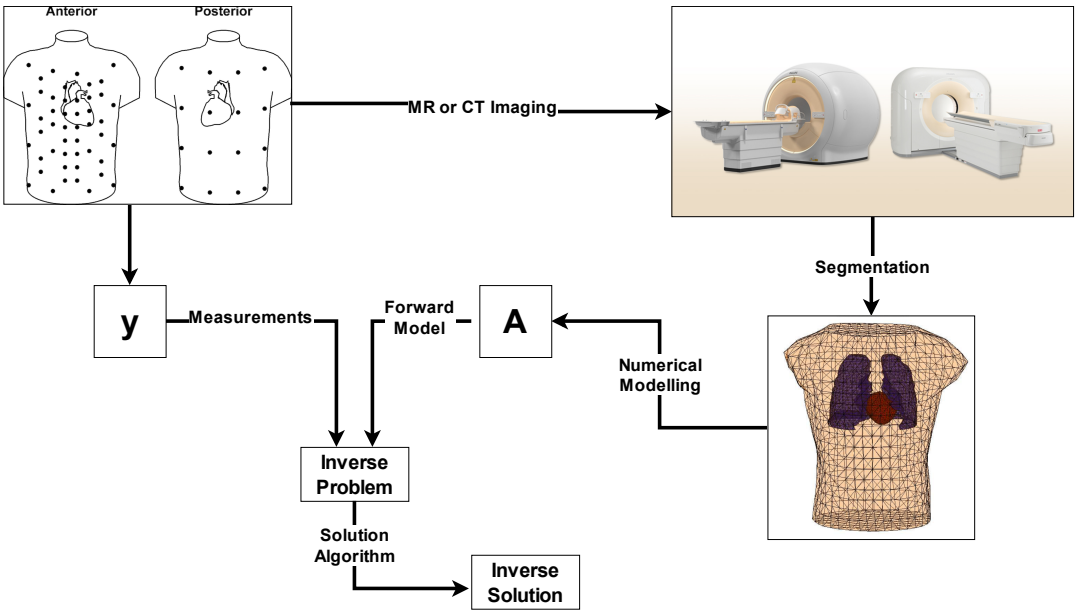

Figure 1.1: The complete workflow of ECGI.

Figure 1.1 summarizes the workflow in ECGI. The electrical measurements on the torso are recorded via a vest consisting of multiple body surface electrodes. Then, the thorax is imaged utilizing modalities such as magnetic resonance imaging or computed tomography. From these medical images, the relative position of the heart and measurement locations are segmented. Following that, the numerical forward model is computed to express the relationship between the sources and measurements. Finally, measurements and the forward model are incorporated to estimate the epicardial potential distribution via the solution algorithm of choice. Any further processing is dependent on the specific task why the imaging is performed, hence is not demonstrated in the figure.

There have been various approaches proposed for the solution of the inverse problem of ECG. These methods include deterministic, statistical estimation and learning-based techniques. Deterministic techniques mainly exploit the properties of the forward matrix and do not usually require any *a priori* knowledge, whereas the statistical

estimation methods models quantities as realizations drawn from probability density functions and utilize the *a priori* knowledge about what is to be reconstructed. Methods that utilize deep learning recently emerged in the field of ECGI to provide better accuracy by discovering more complex non-linear relationships. Most of these techniques solve the problem by using an end-to-end approach and the proposed models learn both the measurement formation process and the prior space in which cardiac potentials lie. Hence, numerous training data and relatively large models are required for model to learn the both tasks. To overcome this, simulated training sets are used to train the models. Then, the models are evaluated on the realistic measured data.

1.2 Contributions and Novelties

The solution methods that require *a priori* knowledge, or training data as its practical counterpart, are widely utilized in ECGI. However, none of the studies has proposed systematic approaches for the performance assessment of the training data prior to reconstruction. Furthermore, the hybrid techniques that combine the system physics and machine learning methods are underinvestigated in the field of ECGI. To tackle these problems, this thesis has the following contributions:

- Evidence and covariance condition number as *a priori* metrics to assess the training data generalization are evaluated in the context of Bayesian MAP based statistical estimation with Gaussian priors.
- The ECGI inverse problem is formulated with Half Quadratic Splitting method and the solution iterations are unrolled to blocks that correspond to solution that require system physics and learning. For the utilization of rectangular kernels in the irregular grids of heart and torso geometries, a method to minimize the neighborhood distance in Euclidean grid is proposed.

1.3 The Outline of the Thesis

The thesis starts with the introduction of both physical and mathematical background on the forward and inverse problem of electrocardiography. Furthermore, the problem

statement is given. Following that, the mutual experimental setup for the developed methods are explained beforehand to make the information flow clearer for the reader. The studies are collected under 2 chapters. In Chapter 4, an efficient data reduction technique is proposed for forming a training data from which the prior model parameters of the Bayesian MAP formulated inverse problem with Gaussian priors are estimated. In Chapter 5, a physics-based AI-assisted solution in Euclidean grids is proposed for the inverse problem of electrocardiography. The findings and the regarding discussion of these studies are presented in their own respective chapters.

CHAPTER 2

LITERATURE AND BACKGROUND

This chapter introduces the background on the electrophysiology and anatomy of the heart. The motion patterns of the different regions of the heart are explained with the corresponding electrical activity that is observed in the electrocardiogram waveform. Furthermore, the representation of the heart voltage data is presented, followed by the mathematical foundation of the inverse problem of ECG.

2.1 Cardiac Anatomy

To solve the inverse problem of ECGI, the basic anatomy and the related working mechanisms of the heart should be understood first. The heart, one of the most vital organs in the human body, is responsible for circulating blood and supplying oxygen and nutrients to all tissues. Understanding the anatomy of the heart is essential for interpreting electrocardiograms (ECGs), which provide valuable insights into cardiac health and help diagnose various heart conditions.

The mammal heart is enclosed in pericardium, a fibroserous sac as in Figure 2.1. The epicardium, also known as visceral pericardium, exists beneath it and covers the surface of the heart. The myocardium is the heart muscle located in the middle layer of the heart walls that is responsible for the contractile function of the pump. The endocardium is the innermost wall of the heart . The Purkinje fibers, which are the structures responsible from propagation the electrical activity to the inner parts of the ventricles, are located at the subendocardium, which forms the boundary between myocardium and endocardium. [18–21].

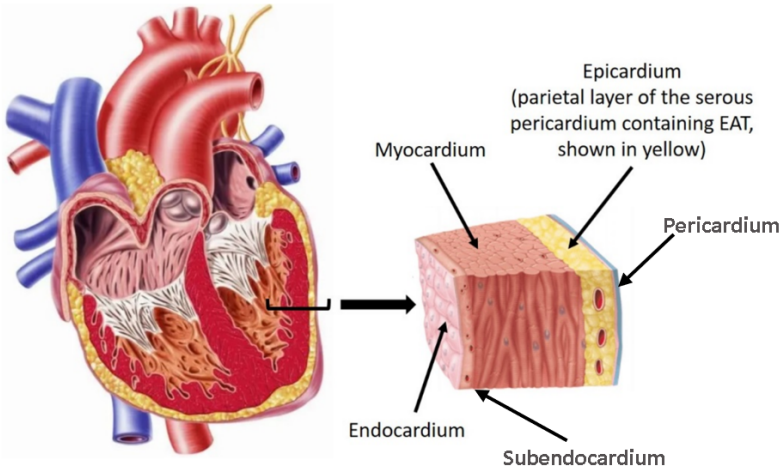

Figure 2.1: Layers of the heart wall (Adapted from [1]).

The heart consists of four chambers: two atria and two ventricles (Figure 2.2). The atria, also known as the upper chambers, are responsible for receiving blood. The right atrium receives deoxygenated blood from the body through the superior and inferior vena cava, while the left atrium receives oxygenated blood from the lungs via the pulmonary veins. When the atria contract, the blood is pumped into the ventricles.

Located below the atria, the ventricles are the lower chambers of the heart and work as the main pumping chambers. The right ventricle receives deoxygenated blood from the right atrium and pumps it through the pulmonary artery to the lungs for blood to be oxygenated. The left ventricle, on the other hand, receives oxygenated blood from the left atrium and propels it into the systemic circulation through the aorta, which is the largest artery in the body. The ventricles have thicker muscular walls than the atria because they need to generate sufficient force to propel blood throughout the body.

To ensure the restricted one-way flow of the blood in the circulation, there are valves strategically positioned between the chambers and major blood vessels. The atrioventricular (AV) valves, including the tricuspid valve on the right side and the mitral valve on the left side, separate the atria from the ventricles. The opening of these valves during the relaxation (diastole) enables blood flow from atria into the ventricles. The closing during the ventricular contraction (systole) of them, on the other hand, prevents blood from flowing backward into the atria.

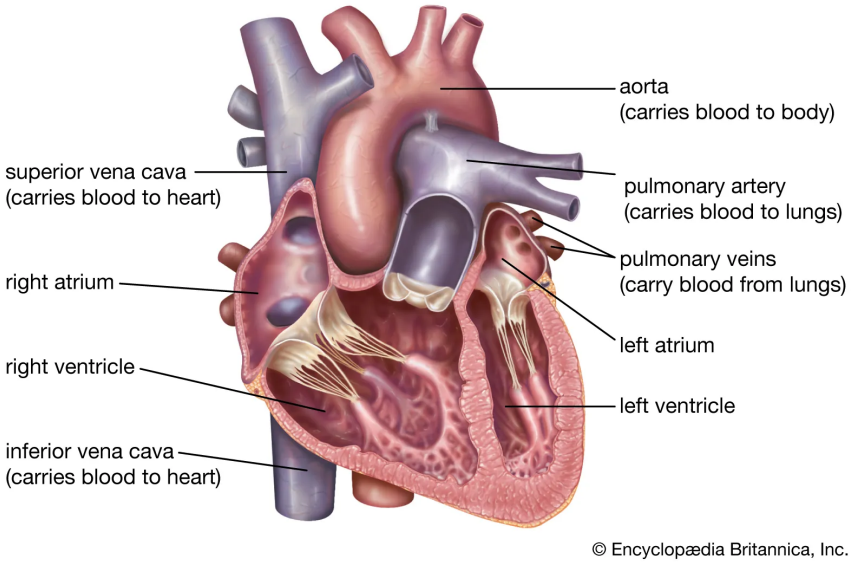

Figure 2.2: Human heart cross section [2].

The semilunar valves (the pulmonary valve and the aortic valve) are positioned at the exits of the ventricles. The pulmonary valve guards the entrance to the pulmonary artery, ensuring the one-way blood flow from the right ventricle to the lungs, whereas the aortic valve prevents blood flowing to the body from returning to the left ventricle by blocking the entrance to the aorta and exit of the left ventricle.

The major blood vessels associated with the heart include the superior and inferior vena cava, which deliver deoxygenated blood to the right atrium from the upper and lower parts of the body, respectively. The pulmonary artery carries deoxygenated blood from the right ventricle to the lungs for oxygenation, while the pulmonary veins bring oxygenated blood from the lungs to the left atrium. Finally, the aorta, the largest artery in the body, receives oxygenated blood from the left ventricle and distributes it to rest of the body, including all the tissues and organs.

2.2 Cardiac Electrophysiology

The harmony of the periodic pumping motion of the heart is explained in Section 2.1. This motion is driven by the proper conduction of the activation potentials on the cardiac surface. Therefore, it is crucial to comprehend the electrophysiology of the

heart.

The cardiac cells are among the electrically active cells in the human body that can generate electrical response if they experience proper stimulus. To characterize this electrical activity, the transmembrane potentials can be defined with respect to the extracellular potentials.

$$\mathrm{V}_{\text{membrane}} = \mathrm{V}_{\text{intracellular}} - \mathrm{V}_{\text{extracellular}} \tag{2.1}$$

The brief changes in transmembrane potentials are called action potentials, and they are generated by a mechanism modelled by nonlinear differential equations of ion channel concentrations and ion currents resulting from the concentration difference. Since, the voltage change from the resting state (ΔV) is the main driving force for ion movement across the membrane, the channel current is modelled by its conductance following Ohm's Law ($I = \Delta V/R = \Delta V g$). In 1952, Hodgkin and Huxley proposed a model to explain the action potential generation in a squid's giant nerve [22]. In 1977, Beeler and Reuter proposed the first model that explains the mammalian ventricle activity [23]. In 1991, Luo and Rudy, improved the accuracy of the Beeler-Reuter model by increasing the number of ionic current variables [24]. With the addition of the calcium ion channels, the model they proposed later in 1994, involved modelling of 15 ionic currents, and it was later improved by Faber and Rudy [25, 26]. The Eikonal model [27] is one of the simplest models used [27, 28]. The model only explains the depolarization phase of the wavefront by relating the local speed, conductivity ratio between longitudinal and transverse directions. FitzHugh and Nagumo modeled excitation and recovery variables using a cubic polynomial [29]. In 1996, Aliev and Panfilov developed a model based on FitzHugh-Nagumo model that explains the cardiac action potentials with two variables [30].

Figure 2.3 shows the phases of the action potentials in electrically active cardiac cells, namely atrial and ventricular myocytes. The inward currents and sodium-calcium exchanger (NCX)[1] are illustrated in yellow boxes, whereas the outward currents are illustrated in gray boxes. Most of the contributions coming from the currents depicted in the gray boxes are neglected in most of the action potential generation models. The

[1] This source is electrogenic and may create inward and outward current [3].

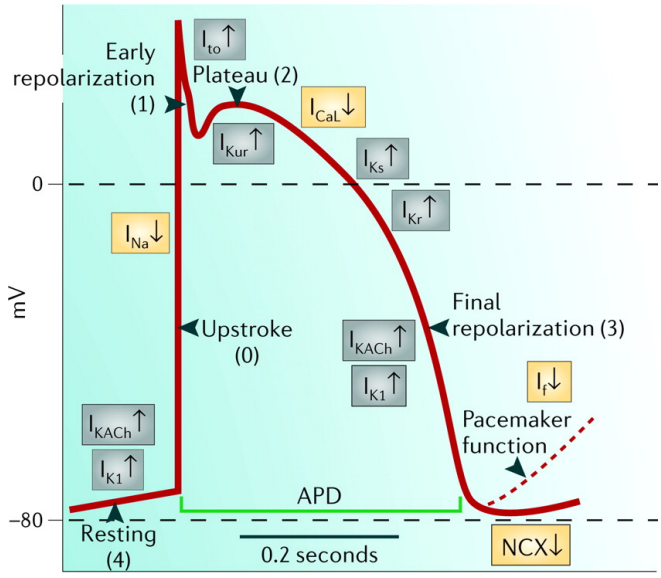

Figure 2.3: Cardiac Action Potential [3].

phases can be summarized as follows:

- **Phase 0 (Upstroke)**: In this rapid depolarization phase, g_{Na^+} increases and g_{K^+} conductance decreases, resulting in an inflow of Na^+ ions.
- **Phase 1 (Early repolarization)**: In the initial or early repolarization phase, the trend reverses and there is a decrease in the g_{Na^+} and increase in the g_{K^+}.
- **Phase 2 (Plateau)** : Unlike the most of the electrically active cells in the human body, there is a plateau phase in the cardiac cell action potential cycle. This is due to the increase in the $g_{Ca^{++}}$ during this phase.
- **Phase 3 (Final repolarization)**: In the repolarization phase, $g_{Ca^{++}}$ decreases and g_{K^+} increases, causing the outflow of K^+ ions.
- **Phase 4 (Resting)**: Due to the increase in g_{K^+} along with the decrease in $g_{Ca^{++}}$ and g_{Na^+}, the cell reaches to resting potential.

The generation mechanism of action potentials explains the single-cell level electrical activity. To explain the cardiac electrophysiology in a physiological level, the propagation of action potentials on the cardiac surface should be examined. The

generic EGM waveform measured on torso is a superposition of propagated, thus time-delayed, action potentials as in Figure 2.4.

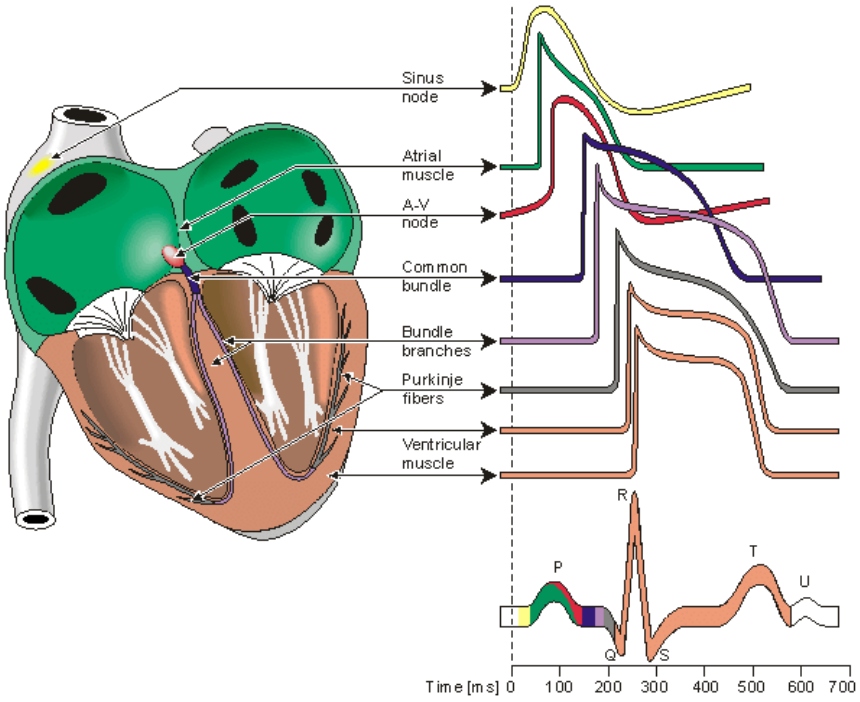

Figure 2.4: Transmembrane potentials for different types of heart cells and the corresponding ECG signal for one cycle [4].

The electrical signal propagation on the heart surface can be explained by these steps:

- Sinoatrial (SA) or sinus node consists of the pacemaker cells that generate the pulses which initiate the heart beat cycles. These cells differentiate from other cardiac cells in their automaticity and the ability to generate rhythmic action potentials.
- From the SA node, the action potentials spread quickly through specialized conducting pathways known as internodal pathways. These pathways help distribute the electrical signal throughout the atria, leading to their contraction. This phase is the main component that contributes to the P wave segment of the electrogram (EGM) wave pattern.
- When the signals reach to the Atrioventricular (AV) node, it briefly delays the conduction of the action potential to ventricles to allow for the completion of

atrial contraction before ventricular contraction begins.

- After the AV node, the electrical waves propagates through left and right ventricles via Bundle of His and the left and right extensions of it into the ventricles.
- Further into the ventricles, the bundles branch further into smaller networks of Purkinje fibers to conduct the propagation to the muscle cells.
- As the waves reach to the ventricular cells, their depolarization is triggered, resulting in a contraction. The simultaneous contraction of ventricles and the relaxation of the atria results in the QRS segment of the ECG waveform.
- The prolonged repolarization of ventricular myocytes results in ventricular relaxation and the formation of the T-wave in the EGM waveform.

2.3 Measuring the Electrical Activity of the Heart

In this section, the methods of measuring the electrical activity of the heart are introduced.

2.3.1 Standard 12-Lead Electrocardiography

12-Lead ECG is a widely used technique that is adopted by the clinicians. It is noninvasive and provides output electrograms with which the clinicians are familiar. The 12 measurements are actually derived from 9 electrodes, as it is observed in Figure 2.5.

However, the limitations of this approach are undisputed. The events happening in the anterior region of the heart can be detected due to the proximity of the electrodes on the chest wall, but the events happening in the other regions, for example ST segment deflection during ischemia, may be underestimated if the activity is weak or nonexistent on the sampled regions of the torso. There is also a probability that the simultaneously superposed events may partially cancel each other and the ECG may not sufficiently represent the extent of ongoing events [31]. Furthermore, the ECG is not always the sole indicator of the disease. For instance, only half of the patients

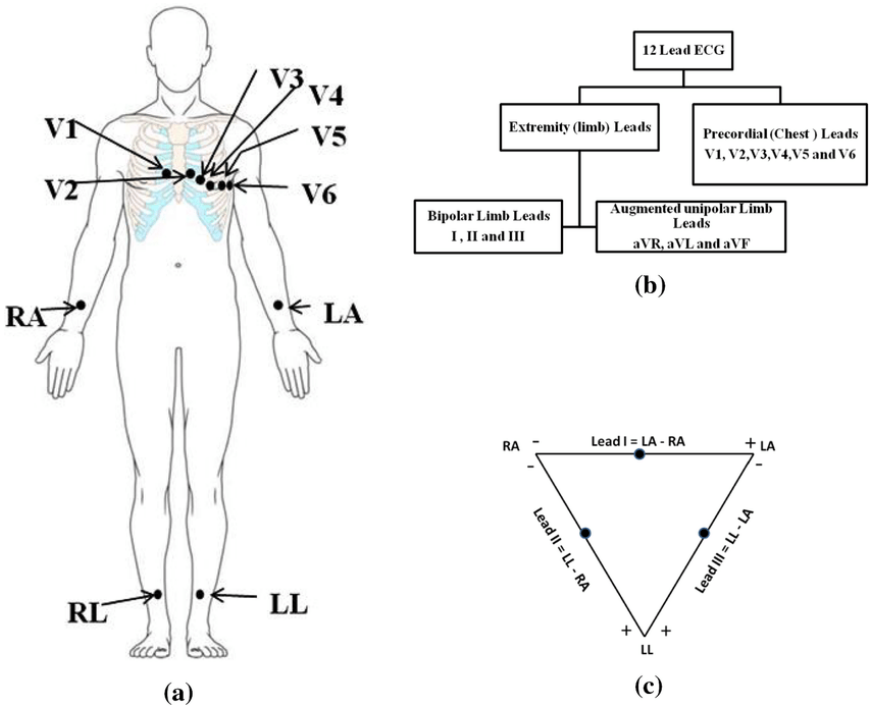

Figure 2.5: 12-lead electrocardiography lead placement [5].

with acute myocardial infraction present with ST segment elevation [32]. Yanowitz *et al.* showed that the areas of maximal ST change were in the torso areas that are not sufficiently sampled by conventional 12-Lead ECG and they concluded that using BSPM provided more quantitative and qualitative assessment for the characterizing the ischemic response to the exercise [33].

2.3.2 Body Surface Potential Mapping

BSPM is a non-invasive and a real-time method that samples the electrical activity more extensively on the thoracic surface than the 12-Lead ECG. There are numerous reviews that are focused on the historical utilization of the BSP mapping systems [34–36]. It provides wider coverage using higher number of densely located surface electrodes as in Figure 2.6 from [6].

Early experiments validated the usage of them on dogs [37, 38]. Later studies confirmed the usage of the BSPM method on humans. McMechan *et al.* detected myocardial infarctions using a multiple logistic regression technique using recording

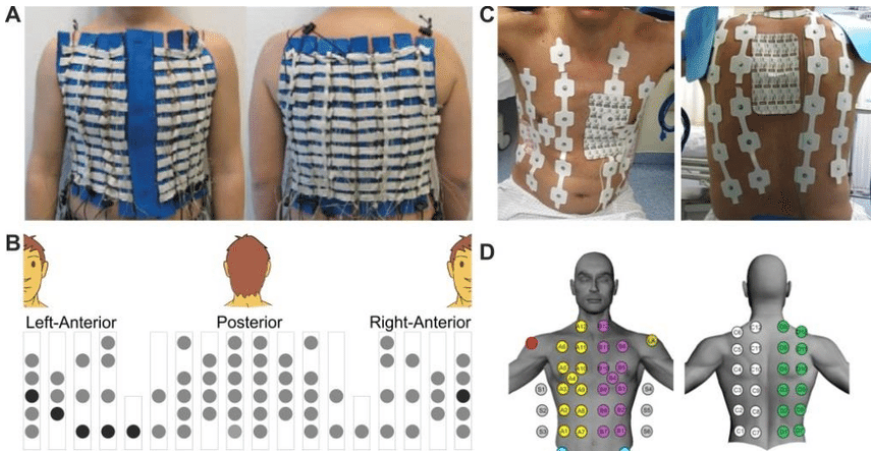

Figure 2.6: Body surface potential mapping vest [6] **(A)** Anterior and posterior view of the vest **(B)** Surface distribution of the leads (Darker dots represent standard V1-V6 derivations) **(C)** Anterior and posterior view of the selected subset of the electrodes **(D)** Surface distribution of the selected subset of the electrodes. Note that some BSPM leads are discarded for recording due to the relevancy of the information they provide in this study. This is not necessarily the case for every recording.

from 90 healthy subjects and 69 patients [39]. Cai *et al.* augmented the BSPM with EEG amplifiers and validated the design on one subject [40].

The discretization of the voltage distribution on the surface, *i.e.*, determining the locations of the measurement electrodes, is another important topic in the forward problem context. Barr *et al.* were among the earliest researchers that worked on the problem [41]. They proposed a 3-step algorithm to quantify the contribution of the leads:

1. Using principal component analysis on the data from 45 subjects to find the coefficients relating the mathematical generators to surface points.
2. Taking data from a subset of points and representing it using these mathematical generators.
3. Selecting the surface points that should be in the subset.

The last step in the outline of the procedure was considering the extensions to the new subjects, in other words, generalization. They found that for consistent accuracy, a

minimum of 24 properly placed leads are required. At this accuracy, the difference between the generated and measured potentials are found to be comparable to the differences in the successive measurements from the same subject. Later, Lux *et al.* confirmed these findings and concluded that 30 leads are required to present the maps to an accuracy of 32 μV [42]. Recently, Parreira *et al.* conducted a study to illustrate the number of required leads to assess the accuracy of ECGI, rather than the lead configuration [43]. They found that the reduction of the number of the leads was associated with the lower agreement rate in the detection of premature ventricular contractions (PVC) and premature atrial contractions (PAC). It was also resulted in reduction of spatial resolution.

Once the measurements are acquired, there are three primary methods of processing and interpreting the BSPMs [44]:

1. **Signal-based approaches:** This approach solely exploits the time and frequency domain characteristics of the ECG signals, including deviations in the ST-segment or peak values of QRS and T wave as well as the morphological features such as P, QRS, or T-wave shapes, duration and symmetry. There is no explicit attention given to the spatial correlation coming from the electrode placements.

2. **Mapping approaches:** The body surface potential mappings that show the voltage values in isopotential-contours-seperated colored regions are plotted using scientific visualization techniques. In other words, the voltage distribution is plotted on the epicardial surface, where the intensities are visualized with colors. The lines having the same potential are detected and the region between them is visualized with the same color. The plotted values can also be specific amplitudes and features derived from raw ECG signal such as integral values taken in duration like QRS complex, ST segment, or T wave. In addition, it is possible to observe how these maps of the selected feature evolve through time interactively. However, clinicians have usually training and expertise in analyzing the classical 12 Lead electrocardiography and there is very little training available on how to interpret the information that BSPM yields.

3. **Reconstruction approaches:** Similar to X-ray CT, which takes multiple mea-

surements to reconstruct the distribution of X-ray absorption coefficients within an image, ECGI takes the raw BSPM measurements, and combines them with the knowledge of torso anatomy, electrode locations and tissue conductivity within the thorax to reconstruct the bioelectrical source distribution in the heart. The reconstruction methods are based on the physical laws such as Laplace's and Poisson's equation [45, 46].

2.3.3 Invasive Epicardial Mapping

There are invasive tools that aim to measure the electrical activity by direct contact to the heart surface and perform the ablation, the process of intentionally creating lesions or scars to deteriorate the conductivity map, such as CARTO mapping [47]. These systems require medical procedures to record the electrical activity by directly contacting the heart tissue. On the other hand, they are much more reliable than the reconstruction techniques in terms of measurement accuracy.

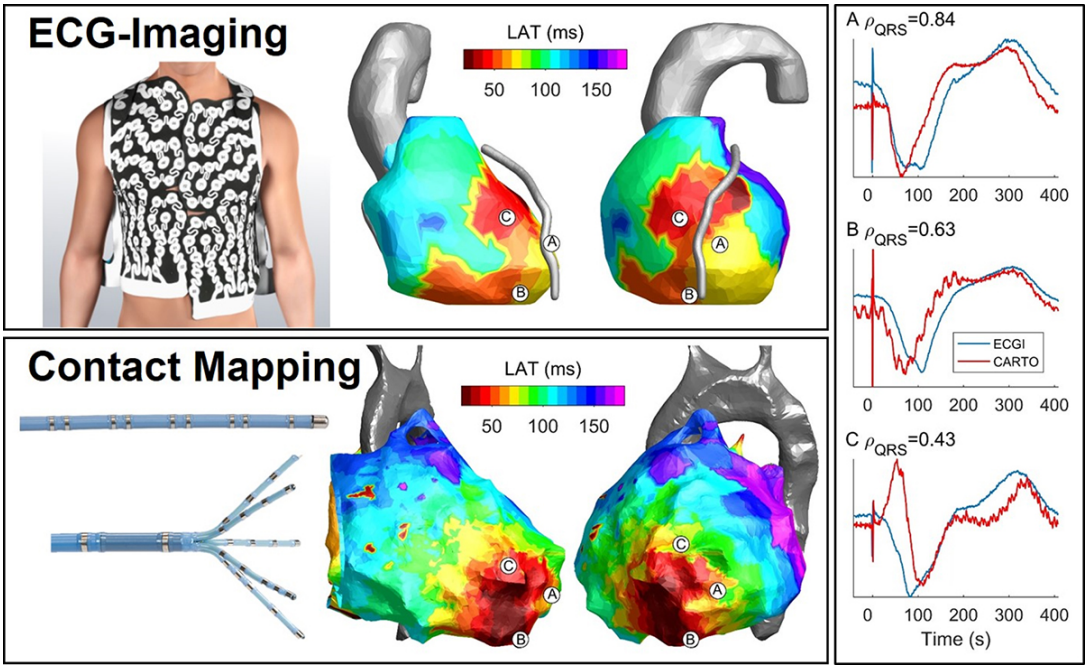

Figure 2.7: ECGI vs CARTO: Both the spatial distributions (left) and EGMs on the right show that the invasive mapping are able to localize the origin of the propagation and capture the sharp transitions better than ECGI, as expected [7].

ECGI efforts emerged to provide better imaging resolution than the current clinically available non-invasive techniques without requiring any medical intervention to the body, catching a trade-off between the invasive mapping approaches and the 12-Lead ECG.

2.4 Equivalent Cardiac Source Representations

The source vector explained in the previous section cannot be determined uniquely if the active region is not accessible, since the electric field caused by any source can be replaced by a single or double layer on a closed surface that entirely encloses the sources [48]. Hence, most of the studies utilized an equivalent cardiac generator in the problem formulation. Early studies used multipole [49] and multiple dipole [50] as equivalent point sources. Multipole approach considers multiple multipole sources at a fixed location, whereas the multiple dipole approach provides location flexibility for the dipoles.

Several studies attempted to reconstruct surface voltage, namely epicardial potentials. The most significant advantage of this approach is that, although the inverted epicardial potential distribution is an ”equivalent” source, this distribution will be the same as the actual (in situ) distribution on the epicardial surface, since this formulation guarantees mathematically unique solution [48]. According to [51], computing the epicardial potentials as the form of solution has two advantages:

- No source specification is required. This prevents restrictive assumptions on the nature of the heart generator from affecting the proceeding of the theoretical development. Hence, only variables with physiological significance end up in the formulation.
- One of the most significant inhomogeneities, the intracavity blood mass, is implicitly included in the formulation. As a result, the homogenous torso assumption is not as restrictive as in other methods.

In this thesis, due to the nature of the data being recorded from the surface of the heart (epicardium), BEM is used to obtain the forward model and the sources are modelled

as epicardial potential sources using the approach introduced in [52]. The forward problem formulation with the selected equivalent source representation is explained in the next section.

2.5 Forward Problem of ECG

The forward problem of ECG is computing the potential distribution on the thorax, or the body surface potential mapping (BSPM) given the distribution of the bioelectrical sources on the cardiac surface. The procedure can be conducted as 2 steps of computation:

- Finding the forward model (forward operator) that relates the voltage distribution on the measurement surface to the distribution of the bioelectrical sources
- Applying the found operator on the given source distribution

The voltage inducing mechanism of sources on the measurement surface is the electric field and it is highly affected by the conductivity of the media in between [45]. To increase the accuracy of the forward problem, the media that was found to be most useful are lungs, intraventricular cavities and muscles [53]. In [54], the blood and the anisotropic skeletal muscles are found to be the most significant inhomogeneity, in terms of accuracy of producing closer potential amplitudes to the ground-truth data. Some recent studies have also shown the importance of liver in inhomogeneity modelling of the torso [55, 56]. When the inhomogeneous media is expressed in volumes of different conductivities, the Maxwell's equations relating the voltages are simplified under the assumptions that the propagation and inductive effects are negligible in the volume conductor of human body [57]. The region Ω bounded by closed surfaces Γ_T and Γ_H, which are respectively torso and heart surfaces, is source-free, hence Laplace's equation is valid [31].

$$\nabla \cdot \sigma \nabla \phi(\mathbf{r}) = 0, \ \forall \mathbf{r} \in \Omega \tag{2.2}$$

where $\mathbf{r}$ represents the three-dimensional spatial coordinates, σ is the conductivity

of the medium Ω and Φ is the volume voltage distribution. Eqn. (2.2) is solved by introducing the Neumann and Dirichlet boundary conditions:

$$\phi = \phi_H, \ \forall \mathbf{r} \in \Gamma_H \tag{2.3}$$

$$(\sigma \nabla \phi) \cdot \mathbf{n} = 0, \ \forall \mathbf{r} \in \Gamma_T \tag{2.4}$$

where ϕ_H is the source voltage distribution on the heart, $\mathbf{n}$ is the outward oriented surface normal [58]. To obtain an expression that relate the potentials across these two surfaces, the geometry modelling followed by a numerical solution is required. Eqn. (2.3) enforces the voltage distribution on epicardial surface whereas Eqn. (2.4) corresponds to source-free body surface constraint.

2.5.1 Geometric Modelling

To obtain the geometric models of the domain where Eqn. (2.2) is solved, the heart and torso volumes are required, along with their conductivities. To generate individual forward models, the common approach is to use segmentation on the magnetic resonance imaging (MRI) and computerized tomography (CT) images [31]. Some recent techniques also utilizes CT-MRI image fusion for segmentation [59, 60]. The need for generating the forward model in every inference case is considered to be one of the major drawbacks of the ECGI, due to the increased time needed for the complete imaging procedure. The conductivity of the tissues are usually determined experimentally, although it is also possible by electrical impedance tomography [61,62] or electrical impedance spectrography measurements [63, 64].

2.5.2 Numerical Solution

The problem stated in Eqn. (2.2) can be solved for any arbitrary shaped volume by numerical computing, *i.e.*, discretization of the problem [65]. Following the segmentation, the volumes are discretized using either one of surface or volume techniques. In surface methods, only the interfaces of the regions are discretized and represented in the numerical model. In volume methods, the whole torso model is represented

numerically [45]. There are different forward modelling techniques that allows the reconstruction of the discrete forward problem including Boundary Element Method (BEM), Finite Element Method (FEM), Finite Difference Method (FDM), Finite Volume Method (FVM) and Method of Fundamental Solutions (MFS) [66]. In addition, there are recent approaches that utilize and benefit a combination of them [67].

FDM models the relationship between source and measurements as resistive elements. FEM, on the other hand, utilizes tetrahedral or hexahedral elements. The anisotropy, or the varying conductivity in individual regions, can only be incorporated by the utilization of FEM, since BEM only approximates the potentials on the boundary surfaces of different conductivity regions [45, 68]. Seger *et al.* showed that the FEM matrices needed less memory than BEM matrices, although FEM reconstructs higher number of unknowns, due to the sparsity of forward matrix generated by FEM. For the same discretization level at the boundary surfaces, it was shown that FEM resulted in higher errors [68]. The BEM is considered to be more suitable and accurate for linear inverse problems with rapidly changing variables, whereas the FEM is more established particularly for non-linear complex problems [69]. MFS is a meshless method that estimates the solution as the superposition coefficients of fundamental solution to Eqn. (2.2).

For the FEM and the BEM, solution vector and measurement vector represents the source coefficients and BSP recordings respectively. For the MFS, solution vector is a vector of weighting coefficients that allows the reconstruction of the source distribution and measurement vector represents the concatenation of BSPs and a zero vector that represents the non-flux boundary condition [67]. In this thesis, BEM is used to generate the forward model due to the reasons mentioned above.

The computation of forward problem has been described in this section. To perform the imaging task, the inverse problem of ECG should be solved to obtain the electrical potential distribution non-invasively.

2.6 Inverse Problem of ECG

The inverse problem of ECG is estimating or reconstructing the source distribution of the heart using a set of remote measurements recorded from the body surface. With the linear relationship between heart and body potentials, the problem can be represented in a matrix-vector equation form after discretization [45].

2.6.1 Data representation

$$\mathbf{y_k} = \mathbf{A}\mathbf{x}_k + \mathbf{n}_k,\ k = 1, 2, 3, \ldots, T \tag{2.5}$$

Here, $\mathbf{y}_k$ represents the torso measurements for M torso electrodes at the time instance k, $\mathbf{A}_{M\times N}$ is the BEM-generated forward model and $\mathbf{x}_k$ is the epicardial distribution or cardiac voltage at N discretized source location at the time instance k. Considering that the beats are represented as a sequence of vectors that correspond to instantaneous voltages on the heart nodes, they can also be represented as a matrix whose columns stack the different time instances:

$$\mathbf{Y} = \mathbf{A}\mathbf{X} + \mathbf{N} \tag{2.6}$$

where $\mathbf{Y} = \left[\mathbf{y}_1\mathbf{y}_2 \ldots \mathbf{y}_k \ldots \mathbf{y}_T\right]$, $\mathbf{X} = \left[\mathbf{x}_1\mathbf{x}_2 \ldots \mathbf{x}_k \ldots \mathbf{x}_T\right]$ and T is the number of time instances the beat is sampled during recording.

2.6.2 Ill-posed Nature of the Inverse Problem of ECG

It has been known that the potentials recorded on the body surface are attenuated and smoothed due to the volume conductor properties of the body. As a result, the measurements carry less spatio-temporally detailed information than the corresponding EGMs. [70]. This implies that, regardless of the number of the measurements and sources, multiple EGM distributions can result in the same measurement, due to low-pass behavior of the human thorax. This causes inverse ECG problem to have an ill-posed nature [70–73]. In other words, even a small perturbation in the measurements can lead to unbounded errors in the estimated solution [45].

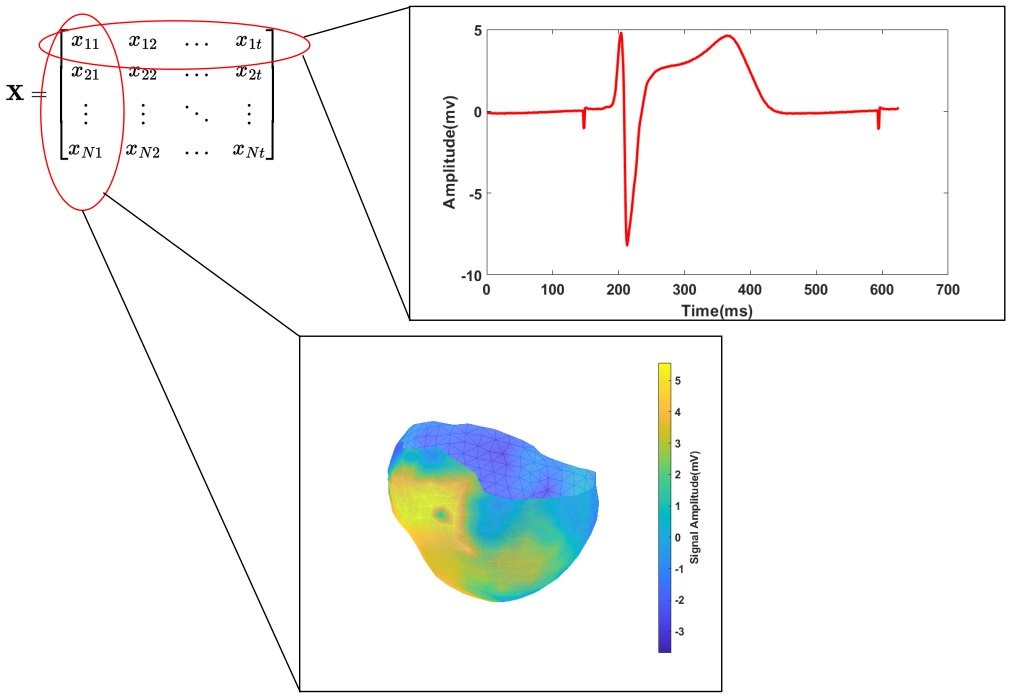

Figure 2.8: Epicardial potential matrix $\mathbf{X}$: The rows represent the EGMs vs time and the columns represent the spatial distribution of epicardial signals for a single time instance (The edge colors are interpolated in the spatial distribution for better visualization.).

The forward models condition number is known to be a measure of the problem's ill-posedness [74]. The closer the condition number of the forward model is to 1, the more well-conditioned the matrix is, hence the more well-posed the problem is. It is crucial to point out that, apart from the nature of the problem, there are some error sources contributing to the ill-posedness of the problem, including geometric segmentation and registration error [71, 75], signal noise, conductivity uncertainty and choice of source model [75].

2.7 Solution Approaches to the Inverse Problem of ECGI

Several deterministic [76–78] and stochastic [79] estimation frameworks are available for the solution of the inverse problem with regularization. Deterministic methods utilize an optimization approach mostly exploiting the matrix properties, whereas statistical estimation techniques impose statistical constraints on the solution. The deterministic solution methods include truncated singular value decomposition (TSVD), total truncated least squares (TTLS), the least-squares QR factorization method and GMRes [72, 80–83]. In this section, the most common approaches to solving the inverse problem are covered under two main categories: physics-based traditional methods and learning-based methods.

2.7.1 Physics-based Traditional Methods

Due to the ill-posed nature of the problem, using regular linear-algebra techniques such as minimum-norm or least-squares solution result in poor estimations of the solution due to noise amplification. Hence, confining the solution to space of the solution, *i.e.* regularization, is needed to estimate meaningful solutions.

2.7.1.1 Regularization

The linear problem in Eqn. (2.5) is usually an under-determined problem where the number of measurements electrodes are lower than the number of source locations. Hence, the problem does not possess a unique solution. In the context of an ill-posed problem, minimizing the error between the measurements and the forward-model-operated data usually results in amplification of the noise and yields poor results. Hence, to overcome the ill-posedness of the problem, one should enforce extra constraints on the solution in addition to the data-model mismatch. One solution to both uniqueness and ill-posedness problem is regularization [67]. The general optimization expression can be stated as:

$$\hat{\mathbf{x}} = \arg\min_{\mathbf{x}} \mathbf{J}(\mathbf{x}) \tag{2.7}$$

where $\mathbf{J}$ is a vector-valued cost function that outputs the total penalty of the solution.

In the inverse problem setting, the cost function J is generally composed of two parts as:

$$\mathbf{J}(\mathbf{x}) = \underbrace{\mathcal{L}(\mathbf{y}, \mathbf{x})}_{\substack{\text{Data-fidelity} \\ \text{term}}} + \underbrace{\lambda}_{\substack{\text{Regularization} \\ \text{parameter}}} \underbrace{\mathbf{R}(\mathbf{x})}_{\substack{\text{Regularization} \\ \text{term}}} \tag{2.8}$$

The data-fidelity term measures how much the solution matches the measurements, whereas the regularization term enforces a condition by adding a cost to the minimization expression utilizing a penalization. The regularization parameter λ is a trade-off parameter that provides a balance between the measurement noise and the prior knowledge imposed on the solution.

2.7.1.2 Tikhonov Regularization

There are many regularization techniques proposed for the inverse problem of ECGI. Tikhonov regularization [84] is a technique that is widely used in the regularization of the inverse problem of ECGI [75,77,85,86]. The solution to the Tikhonov regularized inverse problem is in the following form:

$$\hat{\mathbf{x}}_{\mathbf{Tikhonov}} = \arg\min_{\mathbf{x}} \|\mathbf{y} - \mathbf{A}\mathbf{x}\|_2^2 + \lambda \|\mathbf{R}\mathbf{x}\|_2^2 \tag{2.9}$$

where the regularization term is discretized and given in the matrix form. The solution to the regarding expression is found by optimization and is expressed in the closed form as follows:

$$\hat{\mathbf{x}}_{\mathbf{Tikhonov}} = \left(\mathbf{A}^{\mathbf{T}}\mathbf{A} + \lambda \mathbf{R}^{\mathbf{T}}\mathbf{R}\right)^{-1} \mathbf{A}^{\mathbf{T}}\mathbf{y} \tag{2.10}$$

The regularization matrix $\mathbf{R}$ determines the order of the regularization:

- $\mathbf{R} = \mathbf{I}$ corresponds to the zero-order Tikhonov solution where the solution is confined to have bounded energy.
- $\mathbf{R} = \mathbf{D}$, where $\mathbf{D}$ is a spatial gradient operatir matrix, corresponds to the first-order Tikhonov solution. The solution to enforced to have smoother surface gradients.
- $\mathbf{R} = \mathbf{L}$, where $\mathbf{L}$ is the Laplacian matrix that penalizes surface smoothness using second order derivative approximations between the center node and its first-order neighbors [87].

It is important to note that the regularization part can also be composed of multiple terms.

2.7.1.3 Truncated Singular Value Decomposition

One of the deterministic approaches to regularize the solution is to eliminate the contributions of the smaller singular values to the solution. In singular value decomposition, the matrix is decomposed into its left and right eigenvectors and singular values as follows:

$$\mathbf{A} = \mathbf{U}\mathbf{\Sigma}\mathbf{V}^{H} \tag{2.11}$$

where unitary matrix $\mathbf{U}_{M\times M}$ stacks the left singular vectors of $\mathbf{A}_{M\times N}$ in its columns, $\mathbf{\Sigma}_{M\times N}$ is usually a rectangular matrix that stores the singular values in the diagonal entries and unitary matrix $\mathbf{V}_{N\times N}$ stores the right singular vectors. In the case of matrix $\mathbf{A}$ being real, the hermitian operation can be switched to transpose. In this case, the solution to Eqn. (2.5) can be expressed as:

$$\mathbf{y} = \mathbf{A}\mathbf{x} \tag{2.12}$$

$$\mathbf{y} = \mathbf{U}\mathbf{\Sigma}\mathbf{V}^{\mathbf{T}}\mathbf{x} \tag{2.13}$$

$$\mathbf{x} = \mathbf{V}\mathbf{\Sigma}^{-\mathbf{1}}\mathbf{U}^{\mathbf{T}}\mathbf{y} \tag{2.14}$$

where subscript k is dropped for convenience. Equations (2.13) and (2.14) can be decomposed into a summation of vectors.

$$\mathbf{y} = \sum_{i=1}^{N} \sigma_i \mathbf{u}_i {\mathbf{v}_i}^T \mathbf{x} \tag{2.15}$$

$$\mathbf{x} = \sum_{i=1}^{N} \frac{\mathbf{v}_i {\mathbf{u}_i}^T \mathbf{y}}{\sigma_i} \tag{2.16}$$

$$\tag{2.17}$$

where N is the number of the singular values or rank of the matrix $\mathbf{A}$. The smaller singular values have smaller contributions to the $\mathbf{y}$ in Eqn. (2.15). When computing in the inverse, conversely, the contribution of the smaller singular values is reversed by the inversion hence making the contribution of the signal to measurement insignificant with respect to the noise in the measurement. TSVD is a method to inspect the singular value distribution of the matrix $\mathbf{A}$ as in Figure 3.3 and determine a cut-off index for the singular values to be used in the reconstruction.

The zero-order Tikhonov has a corresponding SVD interpretation. Eqn. (2.9) with $\mathbf{R} = \mathbf{I}$ can be rewritten as follows:

$$\mathbf{J}(\mathbf{x}) = || \underbrace{\begin{bmatrix} \mathbf{A} \\ \sqrt{\lambda}\mathbf{I} \end{bmatrix}}_{\tilde{\mathbf{A}}} \mathbf{x} - \underbrace{\begin{bmatrix} \mathbf{y} \\ \mathbf{0} \end{bmatrix}}_{\tilde{\mathbf{y}}} ||_2^2 \tag{2.18}$$

$$\mathbf{J}(\mathbf{x}) = ||\tilde{\mathbf{A}}\mathbf{x} - \tilde{\mathbf{y}}||_2^2 \tag{2.19}$$

When the singular value decomposition of the system matrix is utilized, we can achieve a diagonal system matrix as follows:

$$\mathbf{Ax} = \mathbf{y} \tag{2.20}$$

$$\mathbf{A} = \mathbf{U\Sigma V^T} \tag{2.21}$$

$$\mathbf{U\Sigma} \underbrace{\mathbf{V^T x}}_{\tilde{\mathbf{x}}} = \mathbf{y} \tag{2.22}$$

$$\mathbf{\Sigma \tilde{x}} = \underbrace{\mathbf{U^T y}}_{\tilde{\mathbf{y}}} \tag{2.23}$$

$$\mathbf{\Sigma \tilde{x}} = \mathbf{\tilde{y}} \tag{2.24}$$

where $\mathbf{y}$ represents the noisy measurements. When Eqn. (2.24) is inserted into Eqn. (2.10) with $\mathbf{R} = \mathbf{I}$, one can obtain the spectral filtered version of the Tikhonov solution:

$$\mathbf{x} = \sum_{i=1}^{\#\text{SVs}} \frac{\sigma_i}{\sigma_i^2 + \lambda^2} \mathbf{u_i^T y v_i} \tag{2.25}$$

where σ_i's are in the descending order, $\mathbf{u_i}$ and $\mathbf{v_i}$ are the left and right singular vectors, respectively.

Besides deterministic techniques, the approaches that formulate the problem in stochastic framework are also available. Statistical inversion methods represent the solutions in terms of probability distributions, from which either a single solution, or samples from the posterior distribution can be obtained [88]. It is also possible with statistical methods to assess estimation error in terms of confidence intervals [89, 90] and error bounds [91–93]. Bayesian Maximum A Posteriori (MAP) estimation and Kalman filtering are among the most popular methods used to estimate the solution in the statistical framework.

2.7.1.4 Bayesian Maximum A Posteriori (MAP) estimation

In this approach, both $\mathbf{y}$ and $\mathbf{x}$ are assumed to be random with a joint probability density function (pdf), $\mathbf{p}(\mathbf{y}, \mathbf{x})$. Then, the solution is chosen to maximize the posterior

probability density function (pdf) of the epicardial potentials [94]:

$$\begin{aligned}\hat{\mathbf{x}} &= \arg\max_{\mathbf{x}} \ \mathbf{p}(\mathbf{x}\backslash\mathbf{y}) \\ &= \arg\max_{\mathbf{x}} \ \frac{\mathbf{p}(\mathbf{y}\backslash\mathbf{x})\mathbf{p}(\mathbf{x})}{\int \mathbf{p}(\mathbf{y}\backslash\mathbf{x})\mathbf{p}(\mathbf{x})d\mathbf{x}}\end{aligned} \tag{2.26}$$

One of the most common assumptions for the prior distribution in the MAP estimation is to use Gaussian distribution. Furthermore, noise is also assumed to have i.i.d. Gaussian distribution. Under these assumptions, the Bayesian MAP solution can be expressed in closed form as:

$$\hat{\mathbf{x}}_{\mathbf{MAP}} = \left(\mathbf{A}^{\mathbf{T}}\mathbf{C}_{\mathbf{n}}^{-\mathbf{1}}\mathbf{A} + \mathbf{C}_{\mathbf{x}}^{-\mathbf{1}}\right)^{-1}(\mathbf{A}^{\mathbf{T}}\mathbf{C}_{\mathbf{n}}^{-\mathbf{1}}\mathbf{y} + \mathbf{C}_{\mathbf{x}}^{-\mathbf{1}}\bar{\mathbf{x}}) \tag{2.27}$$

With the Gaussian assumption, the Bayesian MAP solution also corresponds to the minimum mean square error (MMSE) estimate:

$$\hat{\mathbf{x}} = \bar{\mathbf{x}} + \mathbf{C}_{\mathbf{x}}\mathbf{A}^{T}\left(\mathbf{A}\mathbf{C}_{\mathbf{x}}\mathbf{A}^{T} + \mathbf{C}_{\mathbf{n}}\right)^{-1}(\mathbf{y} - \mathbf{A}\bar{\mathbf{x}}) \tag{2.28}$$

The detailed derivation of the solution can be found in Section 7.1. This type of statistical formulation also allows the estimation of error bounds via error bounds and error covariance [89, 92]:

$$\mathbf{C}_{\epsilon} = \left(\mathbf{A}^{T}\mathbf{C}_{n}^{-1}\mathbf{A} + \mathbf{C}_{x}^{-1}\right)^{-1} \tag{2.29}$$

Note that this is not an a posteriori error metric that measures the error between the reconstruction and the ground truth, instead it is a statistical average of the reconstruction error [90].

Given the i.i.d. Gaussianity assumption for the noise and prior models along with a zero-mean prior, the solution expression Eqn. (4.5) is equivalent to zero-order Tikhonov solution with regularization parameter equal to inverse SNR [90], which is commonly utilized in ECGI [75, 77, 85, 86].

Eqn. (4.5) requires the covariance matrix $\mathbf{C}_{\mathbf{x}}$ and the mean vector $\bar{\mathbf{x}}$ to be defined statistically from the prior information about the distribution of epicardial potentials. The common way to do so is to infer these parameters utilizing the realizations coming from the prior distribution, or in the implementation scenario, a training

dataset which composes of previously measured or recorded ground truth oracles. The dataset formation techniques for the estimation of prior model parameters are explained in Chapter 3.

2.7.1.5 Kalman Filter

In Kalman filtering, solutions are represented as state-space formulation and spatio-temporal relations are implicitly considered by the utilization of non-linear state transitions [95–97]. The major drawback of the Kalman filter approach is to estimate the state transition matrix [98]. The formulation of the problem in Kalman filtering setting is as follows:

$$\mathbf{y}_k = \mathbf{A}\mathbf{x}_k + \mathbf{v}_k \tag{2.30}$$

$$\mathbf{x}_{k+1} = \mathbf{F}\mathbf{x}_k + \mathbf{w}_k \tag{2.31}$$

$$\tag{2.32}$$

where A is the forward matrix in Eqn. (2.5), $\mathbf{F}$ is the state transition matrix, $\mathbf{v}_k$ is the measurement noise and $\mathbf{w}_k$ is the process noise at time instance k.

The solution algorithm to the problem formulated this way is as follows:

$$\mathbf{x}_k = \mathbf{F}\mathbf{x}_{k-1} \tag{2.33}$$

$$\mathbf{P}_k = \mathbf{F}\mathbf{P}_{k-1}\mathbf{F}^T + \mathbf{C}_\mathbf{w} \tag{2.34}$$

$$\mathbf{K}_k = \mathbf{P}_k\mathbf{A}^T(\mathbf{A}\mathbf{P}_k\mathbf{A}^T + \mathbf{C}_\mathbf{v})^{-1} \tag{2.35}$$

$$\mathbf{x}_k^+ = \mathbf{x}_k + \mathbf{K}_k(\mathbf{y}_k - \mathbf{A}\mathbf{x}_k) \tag{2.36}$$

$$\mathbf{P}_k^+ = (\mathbf{I} - \mathbf{K}_k\mathbf{A})\mathbf{P}_k \tag{2.37}$$

where $\mathbf{x}_k$ is the state vector , $\mathbf{P}_k$ is the covariance matrix of the state vector at time k, $\mathbf{F}$ is the state transition matrix, $\mathbf{A}$ is the forward transfer matrix, $\mathbf{K}_k$ is the Kalman gain, and $\mathbf{Q}$ and $\mathbf{R}$ are the covariance matrices of process and measurement noises at

time k. The superscript $^+$ represents the updated variable at time k. The equations correspond to state time update, state covariance time update, Kalman gain calculation, state measurement update and state measurement covariance update respectively.

2.7.1.6 ECGI Applications of Traditional Methods

The deterministic and statistical estimation methods are extensively used to solve the inverse problem of ECGI. Tikhonov regularization has been employed in many studies [75, 77, 85, 86]. Some studies employed Tikhonov regularization on both spatial and temporal dimension (spatio-temporal) and multiple spatial constraints on the problem Eqn. (2.6), where the temporal prior is based on the discrete derivative operators acted on rows of $\mathbf{X}$, or as unit sample responses of high-pass filters [99] and the spatial regularizations were zero and second order Tikhonov. In this study they also proposed the L-surface method, a 2D extension of the L-curve method, to determine the pair of regularization parameters. They found that incorporation of the temporal prior produced more accurate results when compared to the post-processing filtering results, *i.e.*, confining solution to a smoother temporal space was a better idea than imposing spatial constraints and applying smoothing filters after the reconstruction. A later approach [100], utilized the weighted autocovariance matrix of columns of lexicographically flattened $\mathbf{X}$ as what they named a proto-prior and computed the solutions from the decomposition of this matrix, that are calculated with the measurement, forward model and modelled noise. It is also possible to estimate the solution on a beat by beat basis by using different regularizations and use averaging on the computed solutions [101]. There have been attemps to improve the statistical solutions by extracting the features of the space where epicardial potentials lie using a dataset. Cluitmans *et al.* formed a basis for the reconstruction space and conduct the calculation in the transformed domain [102]. The projection-on-realistic-basis approach ended up improving the correlation coefficients of the solution by approximately 2.5% on the solution computed by Tikhonov and GMRes, and approximately 8% on the solution computed by TSVD method. Milanic *et al.* compared the regularization techniques under three main categories: Tikhonov (zero,first and second order), iterative (zero,first,second order conjugate gradient and SVD) and non-quadratic techniques (first and second order total variation). They found that there is little dif-

ference among their performance on average over all source models they used.

One of the most used statistical estimation techniques in ECGI with direct inversion is Bayesian MAP estimation. Serinagaoglu *et al.* combined the body surface potentials and the measurements taken from coronary veins to augment the inverse problem and computed the reliability of the solution by error covariance in Bayesian MAP estimation. They found that the addition of direct measurements did not significantly improve the statistical error expectation [89]. In a later study, they again used the sparse epicardial potentials to augment the inverse problem and computed solutions using 4 different inverse problem techniques: MAP and Tikhonov regularization with and without the sparse measurements. They concluded that the incorporation of sparse epicardial potentials resulted in much smaller predicted error standard deviation when compared to solutions that did not use the sparse measurements. They also found out that Tikhonov results produced smooth spatial results and did not illustrate the wave shape in detail [90].

Kalman filter is another statistical estimation approach to estimate the epicardial potentials. In fact, it is one of the maain methods to incorporate the temporal relationship between the epicardial potentials at consecutive time instances by utilization of state transitions. In [103], authors used the epicardial potentials to estimate the state transition matrix by formulating the problem such that the entries of the state transition matrix became unknowns and the epicardial potentials became the measurements, following the approach proposed by [98]. They investigated three different scenarios where the epicardial potentials were the measured ground truths, Tikhonov solutions and MAP solution. They concluded that the Kalman filtering approach that utilizes the real epicardial potentials outperformed other Kalman-filter based approaches that use inverse solutions to estimate the state transition matrix. MAP solutions were better than the Kalman-Tikhonov solutions in terms of both correlation coefficient and relative difference measurement star. Dogrusoz *et al.* used simulated training dataset to estimate the initial estimate for the state vector and the covariance matrix for the Kalman filter using ML and MAP-based techniques. In spatial and temporal correlation metrics, the Kalman filtering approach with MAP-based estimated priors outperformed the Tikhonov regularization [104].

Almost all the approaches mentioned in this section require training data for different purposes. Cluitmans *et al.* used a realistic training dataset to form a basis for the span of possible EGM solutions and incorporated this prior information to project their solutions into this domain in their deterministic approach. In [89, 90], the realistic training data was used to estimate the mean and covariance of the previously assumed Gaussian pdf using unbiased maximum likelihood estimators. In Kalman filtering approach, the training data is utilized to estimate the state transition matrix in [103] and for the estimation of prior model parameters in the Bayesian MAP solution to estimate the initial state vector of the Kalman filter in [96]. Erenler *et al.* used two different training dataset for the MAP estimation of Kalman-filter related parameters [105]. In the first dataset, they included the beats whose excitation origins are in the range of 20 mm of the ground truth beat's initial stimulation point, whereas the second dataset included the beats that are at most 40 mm distant than the test beat's excitation origin. They concluded that using a wider range region that covers the pacing locations of the beats resulted in slightly improved electrogram reconstructions, stating that the diverse training set provided more regularized results. In another study, they compared the usage of generated (or simulated) training data and measured training data in the context of MAP and maximum likelihood based estimation. They concluded that even using a simple simulation method with a large coverage of pacing locations 80 mm, can sufficiently represent the prior distribution in Kalman-filter-based-ECGI [104]. In [106], the authors used a neighborhood based training data selection process, similar to [105]. In this study, they concluded that using beats from the first or second order neighbors of the ground truth beat generally resulted in sufficient accuracy of reconstruction. The inclusion of further beats resulted in a slight decrease in the performance. It is important to point out the common drawback of these approaches. In these studies, the pacing location of the test beats are known previously from the stimulated node information. In the real life scenario, this approach would require the estimation of ground truth excitation origin via inverse reconstruction that does not require any training data, *e.g.* Tikhonov solution. The created datasets' coverage will depend on this first initial estimate and the accuracy of excitation origin finding algorithm. Hence, the accumulated in the first reconstruction may lead to a dataset that is not properly composed for the ground truth excitation origin.

All the estimation techniques introduced here have not yet been shown to have any significant superiority to the others. The formulations of them impose the relationship to be linear in measurement formation process and state transition. Although, under ideal circumstances the measurement formation process is linear, the state transition have known to be non-linear. Learning-based methods, especially neural networks, have shown significant performance in capturing the non-linear patterns in the data. Hence, it is also a promising tool in imaging inverse problems.

2.7.2 Learning-based Methods

Machine learning methods are known for their success for predicting the relationships between a given set of outputs and inputs in the supervised learning, or the patterns in the input in unsupervised learning. The earliest efforts in the medical domain was concentrated on medical image processing to draw conclusions on already computed medical images [107]. Mostly linear models like SVMs or their non-linear extensions such as SVMs with kernels are utilized for the tasks like image classification. With the increasing availability of the data and computing infrastructure, neural networks and deep learning started to be highly investigated in the field [108]. The trend for years between 2010 and 2015 can be seen in Figure 2.9.

Lots of different architectures have emerged and been experimented. Review papers are published on which architecture to use [109] and whether to fully train the network for medical image analysis [110]. Graph neural networks (GNNs) are also utilized in different bioinformatics tasks and there is an increasing trend in the number of published papers for each of these tasks [111]. With the introduction of vision transformers [112], they are utilized in many medical image processing tasks in different modalities [113, 114]. Thanks to their architectural properties that stack components corresponding to affine transformations, *i.e.* linear transformations and translations, and point-wise nonlinearities, neural networks can learn the complex conditional probability distributions, and recently prior probability distributions with generative models, accurately. The usage of these tools and techniques in medical imaging inverse problem are explained in the next section.

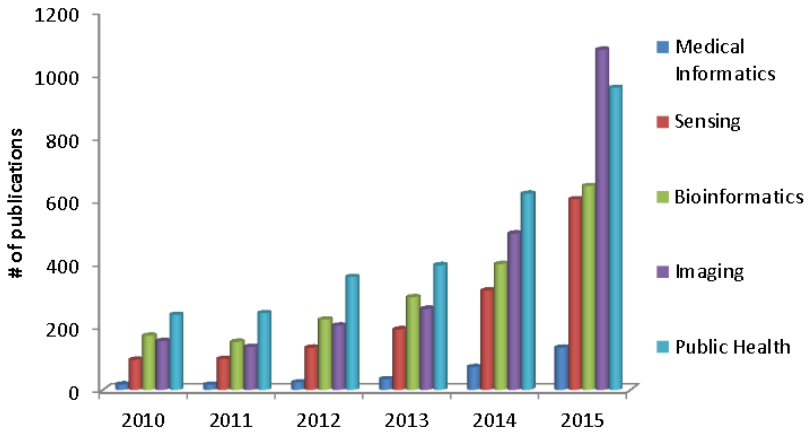

Figure 2.9: Distribution of published deep-learning papers in healthcare between 2010 and 2015 [8].

2.7.2.1 General Medical Imaging Inverse Problems

In the last decade, machine learning methods have emerged to exhibit outstanding performance in different fields of computational imaging. McCann *et al.* published a review study on the usage of CNNs in the inverse problems and claimed that CNNs can generalize all shift-invariant algorithms [115]. They reviewed the applications of denoising [116], deconvolution [117], superresolution [118] and plain reconstruction in modalities such as MRI [119, 120] and CT [121, 122]. There are also different fields of imaging inverse problems where researchers applied learning based techniques such as electrical impedance tomography and sparse synthetic aperture radar imaging [123, 124]. The utilization of neural networks in medical imaging problem is not only encountered in image formation process, but also in regularization parameter selection. Afkham *et al.* used deep neural networks (DNNs) to estimate the regularization parameters based on the measurements (or observations) [125].

The most concrete perspective on CNNs generalization to inverse problem comes from the idea of unrolling. The idea of unrolling, which was first originated in the study where authors unrolled the iterative shrinkage thresholding algorithm (ISTA) for sparse coding into a neural network [9], provides a general perspective that nearly all iterative reconstruction algorithms that alternate between linear steps and point-

wise nonlinear steps. Therefore, CNNs should be to perform similarly provided that they are trained properly [115]. In 2017, Jin *et al.* provided a narrower condition on the applicable forward operators and showed that the normal operator of the operators that inherently carry isometry, multiplication and change of variables operations can be expressed as convolutions. Hence, they used CNNs along with the sparse-view back-projection to outperform the total-variation regularized computerized tomography problem [10]. They showed the structural relationships between ISTA method with sparsifying transforms and the convolutional neural networks. The review study also suggested that the spline theory results show that the rectified linear unit (ReLU) functions can approximate any continuous function, resulting in that CNNs utilizing ReLUs can closely approximate the proximal operators utilized in conventional iterative techniques [115].

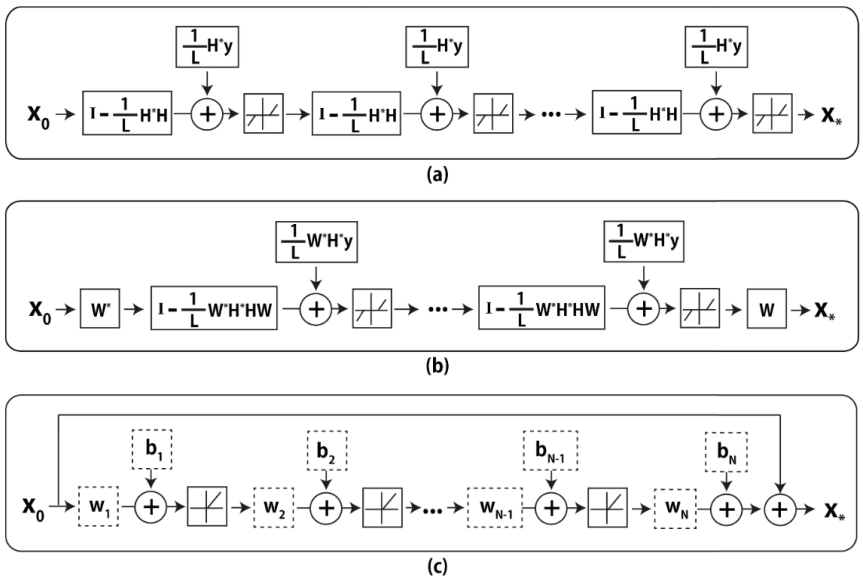

Figure 2.10: Block diagrams for (a) ISTA [9], (b) unfolded version of ISTA with sparsify transform, (c) convolutional neural network with residual skip connection [10].

The structural similarity of ISTA and CNN for imaging problems is shown in Figure 2.10. All methods use a linear transformation (gradient update, sparsifying tranformation's gradient update, linear convolutional layer), a bias term and a point-wise nonlinearity (shrinkage and ReLU). The CNN method, additionally utilizes a residual skip connection to improve and accelerate the learning.

Recently, generative models are introduced to tackle the inverse problems. Starting from the study of Bora *et al.* , there has been numerous work proposing deep generative priors in the linear inverse problems [126, 127]. Duff *et al.* named three forms of generative regularizers for the inverse problems [128]. These methods usually included confining solution to the range of the operator, *i.e.*, the set of solutions that the generative model is trained to generate. One extension to this is to relax the solution by extending the range space of the generator. Another approach is to add extra analytical constraints that matches the prior of the latent space, such as bounded energy. Normalizing flows learn the bijective mapping between a latent space and an image space of same dimension and provide a generated distribution with tractable density [129].

One of the most recent advancements that can be considered as the extension of the variational auto-encoders are variational diffusion models [130]. These models learn how to predict the original ground truth image from an arbitrarily noisified version of it [131]. This approach has recently emerged as powerful generative priors for solving inverse problems [132]. Graikos *et al.* used diffusion models conditioned on the measurements as plug-and-play priors for semantic image segmentation and conditional image generation tasks. Conditional generative models for inverse problems are modelled such that forward operator and measurements impose some constraints during the reverse diffusion step [133], analogous to gradient update and proximal steps in iterative methods. Chung *et al.* showed in [134] that any contraction mapping such as projection onto convex sets and gradient steps, can be utilized to impose the data-fidelity constraint. The utilization of diffusion models are demonstrated in a set of inverse problem including MRI [135, 136], image in-painting, colorization, sparse-view computed tomography [133].

2.7.2.2 ECGI Applications of Learning-based Methods

So far, a summarized literature review has been given on the usage of learning-based methods in medical imaging inverse problems to provide an overview. This section focuses on the recent advancements resulted from these techniques in the field of ECGI.

In [137] used a simulated training set on six cardiac anatomies and on single pacing site to train the conditional variational autoencoder model that reconstructs the activation pattern throughout the myocardium in a volumetric manner. They use 2D convolutions to capture spatiotemporal correlations in the data. This approach resulted in mean absolute error of 11.33 ± 4.10 ms of error in computed activation maps.

Pilia *et al.* generated a simulated dataset to train the Convolutional Neural Networks (CNNs) to localize the ventricular excitation origin in a two-step process [138]. They first processed BSPMs to a Cartesian grid. Following that, the first network learned the activation time boundaries in temporal direction whereas the networks in the second step learned to output the ventricular coordinates in cobiveco that correspond the excitation origin [139]. Although they were able to achieve 1.5 ± 1.3 mm localization error on the generated test data in the best case, the best result on the clinical data was 32.6 ± 25.3 mm with the SVD post-processing. The classical methods like Tikhonov performed 26.1 ± 21.6 mm LE on the clinical data, proving that the trained networks do not generalize to the clinical test data.

Tenderini *et al.* used a partial differential equation (PDE) aware deep learning model for the inverse solution [108]. In this physics-based hybrid approach, the physical awareness was pursued by the projection of the epicardial potentials on a subspace spanned by the solutions of the governing PDEs and the inclusion of a tensorial reduced basis solver. To train their networks, they simulated and used a synthetic training data using Aliev-Panfilov model for the EGMs and the corresponding 12-lead ECGs.

Chen *et al.* proposed an end-to-end training approach to relate the epicardial and torso potentials of the pigs. They proposed 2 ways to utilize the common neural network operations like convolutions and LSTM layers [140]. In the first part, they matched the directly recorded 1D torso ECG data and 1D EGMs by training a network that is composed of LSTM and fully connected layers. In the second part, they registered the 3D torso geometry on a 2D plane. They upsampled the 1D ECG data on this 2D plane by bilinear interpolation and used a CNN to match the transformed torso data to the 1D EGMs. They found that CNNs were better at reconstructing the activation

time maps. They also pointed out that training patterns they utilize in different cross validation trials (data coming from different pigs) have shown great variability in the performance.

The geometric meshes are represented as graphs and convolutions operations are redefined on this non-Euclidean geometry framework in [141]. In this spatio-temporal graph convolutional neural network, the spatial convolutions are defined with spline-based kernels, whereas the temporal convolutions are kept same as the standard 1D convolutions after the spatial convolution. The signals are directly represented on their own domain, that is to say, heart and torso geometries. The physics-based inverse imaging function was designed to be learned by a bipartite graph assuming that the linearity between heart and torso potentials in the latent space still holds. The latent heart potentials on the vertices of the latent heart geometry is expressed by the linear combination of the vertex voltages of the latent torso geometry. A later study [142] showed that this methodology showed similar uncertainty with Tikhonov regularization in reconstructed cardiac sources resulting from cardiac and torso geometry variability. It was also concluded that the graph neural network (GNN) based method was less sensitive to the modelled geometric uncertainty. However, the authors stated that the reported generalization metrics were the results of the fine-tuning experiments conducted with little amount of data. Even with fine-tuning on the geometries that only differs from the training data in terms of rotation patterns, the performance drop is observed in the GNN-based technique [143]. In end-to-end learning-based techniques the training data is used to optimize the reconstruction metrics directly, *i.e.*, the training configuration is based on learning the conditional probability distribution, or regularized image reconstruction in the practical imaging scenario, unlike in traditional methods where the training data is usually used to estimate the prior distribution of the oracle. Within the ECGI literature, there is a notable absence of learning-based studies that separate image reconstruction and regularization into distinct steps, while also incorporating the learning of prior distribution.

2.8 ECGI Validation

To prove the benefit of the imaging modality, ECGI methods should be experimentally validated so that it can be utilized in human clinical applications and have a socioeconomic effect. The validation timeline can be seen in Figure 2.11.

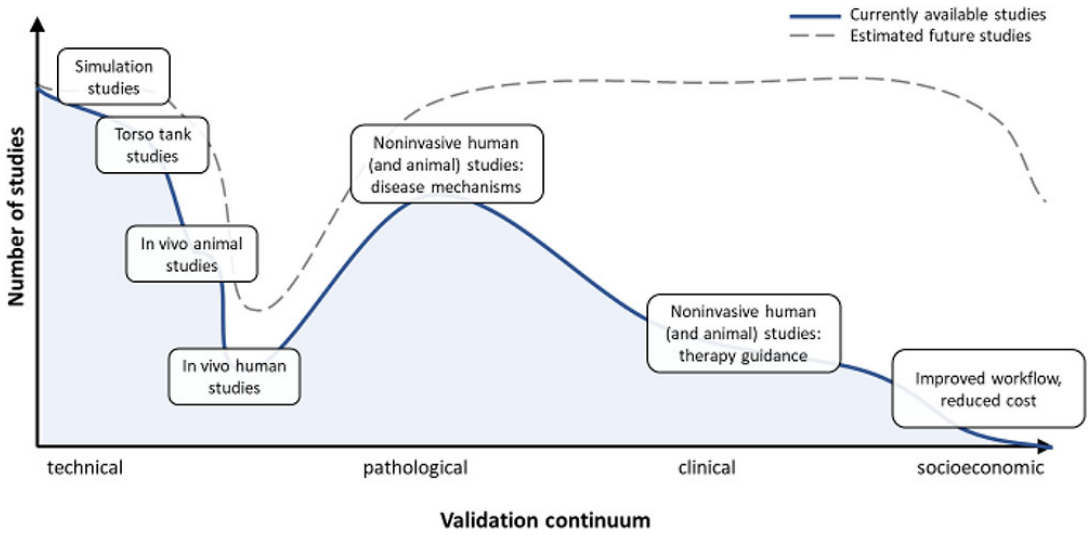

Figure 2.11: Development and validation of ECGI studies [11].

In the experimental ECGI literature, the main ways of data acquisition can be listed as follows:

- **Torso-tank:** In this setup, the heart of an animal is isolated from the body and suspended within a human shaped torso tank. To maintain proper operation of the heart, it is perfused via blood coming from the arteries of a second support dog as in Figure 2.12. The blood was returned to the support dog from a right ventricular cannula to the jugular vein [12, 143, 144]. The torso tank is filled with an electrolytic solution of 500 Ω-cm resistivity to approximately mimic the conductivity behavior of human thorax. A flexible sock array is placed on the surface of heart to capture electrical activity via surface electrodes. The cardiac activation is generated with stimulation electrodes and signals on both surfaces are recorded simultaneously. This experimental environment has been also set by utilizing pig hearts as in Figure 2.13 [13].

- ***in-vivo:*** These setups include invasive recordings coming from the living or-

ganisms. In [145], 2 silicone bands with 99 electrodes are inserted in 4 normal anesthetized dogs' basal and mid-basal ventricular epicardium. After chest closure, body surface electrodes are attached to the chest and the unipolar potential recordings are recorded simultaneously. These experiments are conducted on a CT table so that during the imaging to avoid a modification in the relative positions of the electrodes or disconnection of them.

- ***in-situ:*** Unlike *in-vivo*, the *in-situ* experiments utilized isolated heart preparations, and it does not provide information about the electrical activity in its natural physiological state within the body. However, it is free of the interference effect of the surrounding tissues and researchers have direct access to the heart, allowing them to manipulate it more.

- **Simulation:** Most of the studies that require training data generate synthetic data to develop the proposed method using the methods explained in Section 2.2.

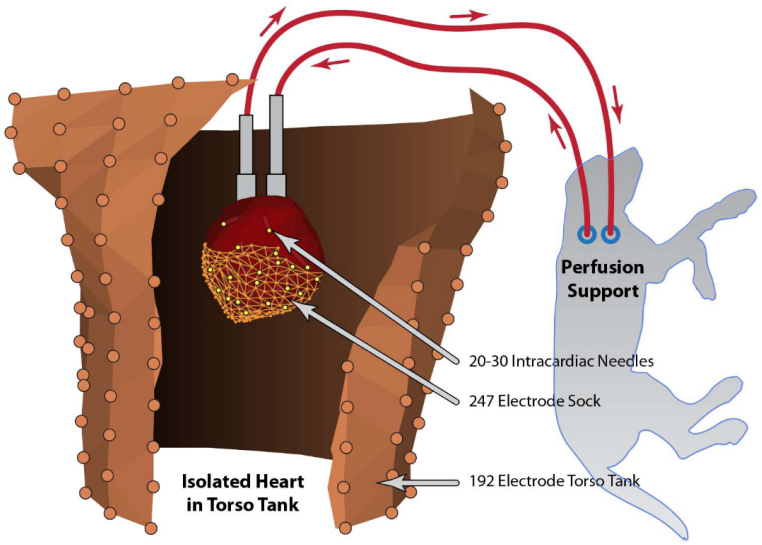

Figure 2.12: Langendorff perfusion setup with canine hearts [12].

All of these validation experiments are conducted to provide a safe basis for the human clinical operations. The next section will cover the clinical application of ECGI in humans along with the possible use cases of the methodology.

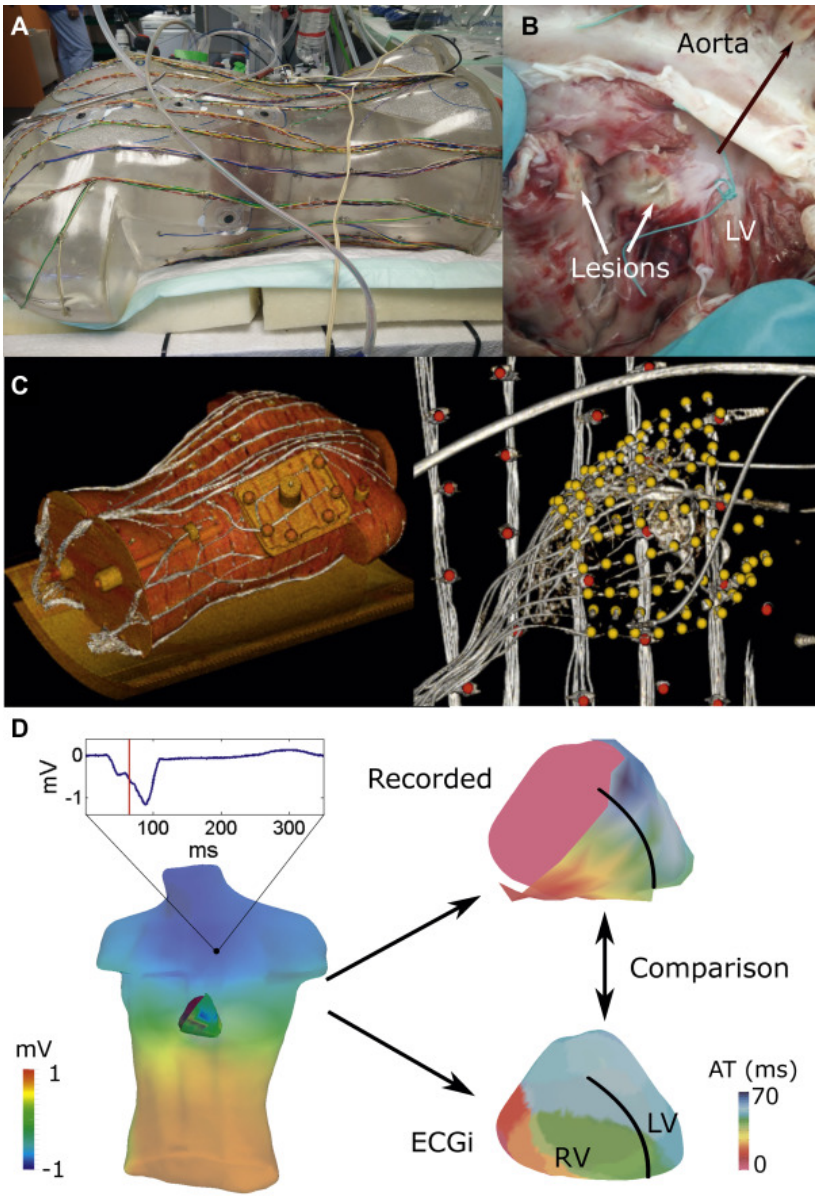

Figure 2.13: Acquisition workflow followed in [13]. **A:** Torso-tank setup with Langendorff perfused pig heart. **B:** Ablation lesions **C:** 3D fluoroscopy scan of full torso and segmented electrode positions **D:** ECGI step and comparison to ground-truth recordings.

2.9 Clinical Applications

The most common CVDs that require the reconstruction of the electrical activity are atrial tachycardia (AT), atrial fibrillation (AF), ventricular tachycardia (VT), ventricular fibrillation (VF), premature ventricular contraction and Wolf-Parkinson White Syndrome. For AF, ECGI is currently used to detect the activation patterns during the arryhtmia thorough phase mapping to localize the mechanisms of this activation via the estimated dominant frequency or singularity points in phase mapping [146]. This method is shown to be successful in terms of correlation to the ablated regions. In PVC, ECGI can provide useful presurgical guideline by localizing the arrhythmogenic site or at least estimating a region of interest before the catheterization. For VF, the contribution of ECGI to diagnosis is provided by a very similar process to that of AF [146]. Recently, Dogrusoz *et al.* investigated the methods of ECGI for PVC localization in humans. They compared dipole and potential based source configurations with different inhomogeneity models in the context of Tikhonov zero-order regularization [54]. They found that dipole-based methods provided more accuracy, however they do not provide detailed progress of the EGMs over the QRS region and T wave. In this case, the potential based solution should be used with edge-presevering inverse and activation time computations.

2.10 Current State of the Art

The most recent research on ECGI is mainly focused on increasing accuracy of the inverse solutions and generalization among different patient geometries. End-to-end training approaches like [147] results in uninterpretable behavior in the signal reconstructions. In [141, 143], the authors propose a physics-based reconstruction by learning the mapping between latent heart and torso potentials in terms of coefficient-weighted source-to-measurement distances, that resembles to the forward operator of MFS [66]. By utilization of graph neural networks, the authors claim to generalize to new geometries by using a small dataset of heart potentials on the new geometry. Although there is a performance drop in the inference time when they use the trained network directly, this fine-tuning strategy resulted in sufficient performance. It is also

important to note that this approach still requires fixed-size inputs, hence the generalization to new geometries are limited to rotated or shifted versions of the training geometries. The authors state that this approach has advantage over the methods that use Euclidean networks, *i.e.*, traditional CNN structures. However, physics-based hybrid Euclidean approaches and how the modelling can be modified to apply Euclidean networks remain underinvestigated.

Although it has been shown that the statistical estimation and learning-based techniques can achieve higher accuracy and performance under proper training situations, there has been a little study on how to systematically select the training data based on the available dataset or based on the measurement in the inference time. The existing methods provide intuitive and greedy approaches to this problem, however the conclusions of those studies was only based on a posteriori reconstruction metrics. Hence, for both of the frameworks, the assessment of the training data are rarely conducted before the model training. There has been recent developments in the area of artificial intelligence (AI) on the selection of training data to alter the performance. Jarrahi *et al.* states that the data should be taken care of considering the whole life cycle of AI systems, beyond "preprocessing". By adopting a data-centric approach, rather than a model-centric approach which tries to optimize the model based on the given data, more accurate solutions and less biased systems can be created [148]. However, this systematic approach has not yet been introduced to the field of ECGI, neither in statistical estimation nor in AI-assisted studies which has recently emerged.

This thesis investigates the usage of variable splitting and unrolling method to augment the physical knowledge about the system with neural networks. Furthermore, in the Bayesian MAP inverse problem with Gaussian priors, the effect of prior model composition is explored in a systematic way.

CHAPTER 3

EXPERIMENTAL SETUP AND VALIDATION

3.1 Experimental Data

In this thesis, the data from seven *in-situ* experiments conducted at University of Utah is utilized for the estimation of prior model parameters in Chapter 4 and training the denoising neural network in Chapter 5 [149]. In these experiments, the isolated heart from one canine, which was perfused by a support dogs' circulatory system, was suspended in a torso tank full of electrolytic solution. All experiments are performed under deep anesthesia via procedures approved by the Institutional Animal Care and Use Committee of the University of Utah conforming to the Guide for the Care and Use of Laboratory Animals (02-03010). A sock that contains 490 electrodes was placed on the surface of the heart and the measurements are sampled at 1kHz sampling frequency. The heart is stimulated from different pacing sites that cover the epicardial surface. The total number of beats in the dataset was 380. After removing the data that contain artifacts, the number of beats dropped to 326. Afterwards, the dataset is split into two parts as training and test dataset such that the beats in the test data have unique pacing site locations from 4 experiments. The distribution of these pacing site locations can be seen in Figure 3.1 All the beats from the remaining 3 experiments are included in the training data.

Since there was no access to the simultaneously recorded torso data, we simulated the BSPs from the EGMs. The forward problem, *i.e.*, the process of computing the BSPs from the EGMs, is conducted using an inhomogeneous thorax model, whereas the inverse problem is computed with a homogenous model which does not include the lung inhomogeneity, to avoid inverse crime [150]. After the generation of BSPs,

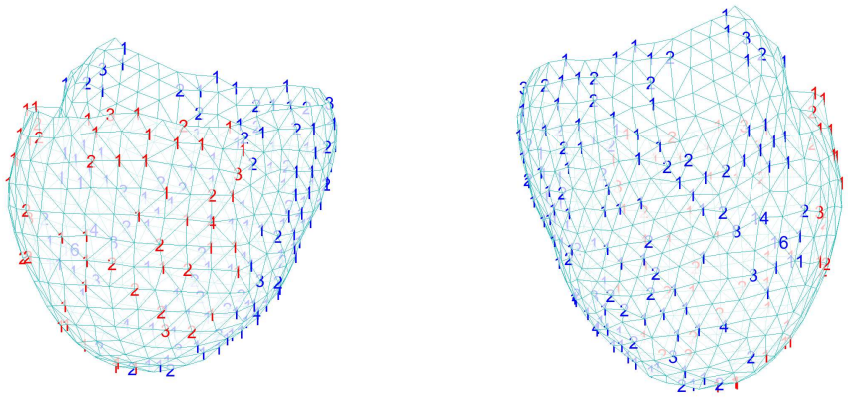

(a) Left. (b) Right.

Figure 3.1: The pacing site distributions of the utilized training data in different ventricles. **(a)** Number of training data that is paced from the labeled nodes on the left ventricle shown in red **(b)** Number of training data that is paced from the labeled nodes on the left ventricle shown in blue.

they are distorted with 30dB SNR i.i.d. noise for each of the time instance separately, where SNR definition is ratio of the signal variance to noise variance, $\frac{\sigma_x^2}{\sigma_n^2}$.

3.2 Geometries

Recordings from only some specific leads were used in the simulations. Hence, from the fine-meshed torso geometry we have, these leads are labelled and extracted to generate the coarse-meshed geometry. For the forward model, a simplified torso geometry with vertices as only recording leads was utilized as in Figure 3.2. The same torso lead configuration that was proposed by Lux *et al.* was used [42]. By using triangulated meshes of the heart and the body surface, the forward transfer matrix is calculated by solving Laplace's equation using the Boundary Element Method (BEM) [45, 151, 152].

The forward models corresponding to these torso geometries are shown in Figure 3.2 and the condition number of them along with the distribution of the singular values

are computed and plotted in Figure 3.3.

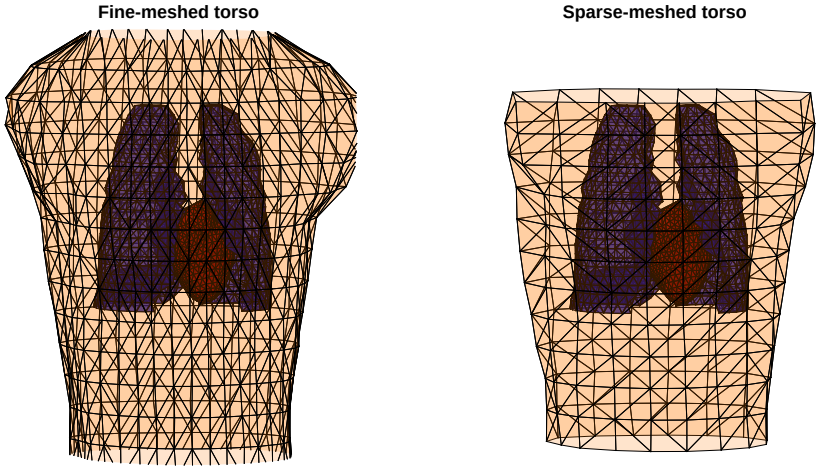

(a) Front view.

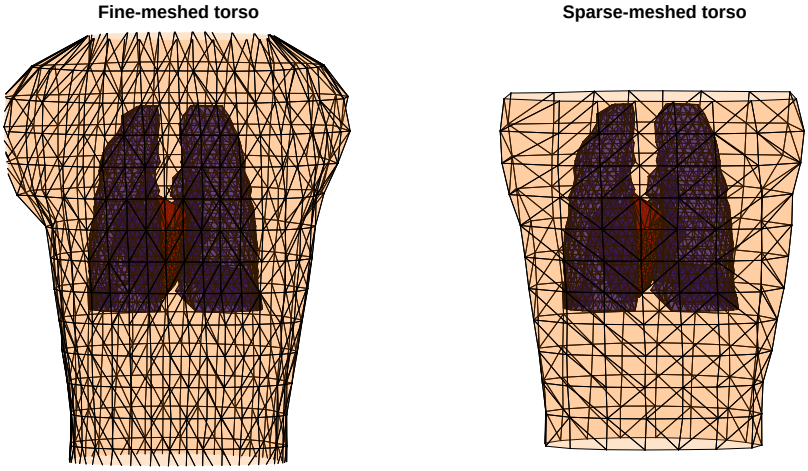

(b) Back view.

Figure 3.2: Fine and sparse-meshed torso geometries.

The fine-meshed torso contains 1538 triangular elements whereas the sparse-meshed torso has 352. Mean node-to-node distance is 11.57 ± 8.56 mm for the fine-meshed torso and 22.13 ± 16.77 mm for the sparse-meshed torso. The number of nodes (vertices) they have is 771 and 192 respectively.

In fine-meshed torso case, the forward matrix $\mathbf{A}$ is of size 771×490, whereas the

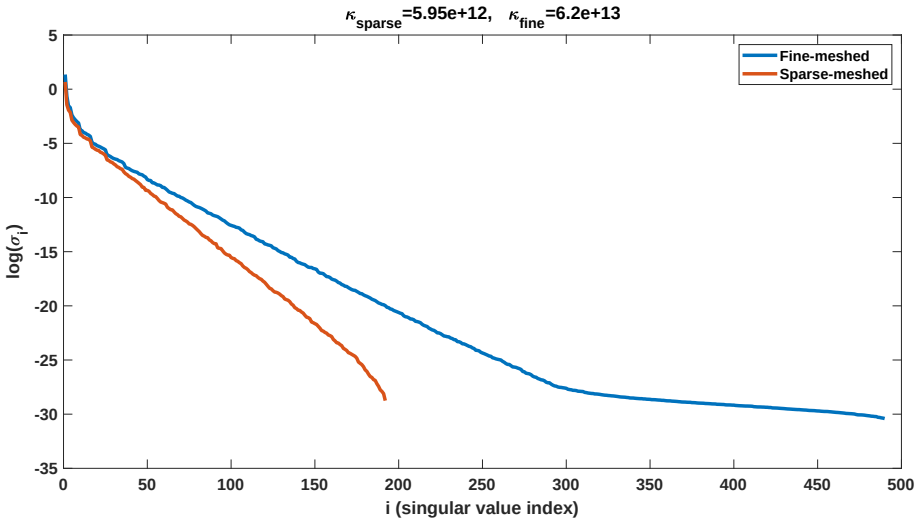

Figure 3.3: Singular value distribution of forward model corresponding to geometries in Figure 3.2.

sparse-meshed torso model results in a forward model of size 192×490 where 192 leads are selected based on the configuration proposed by [42]. The singular value distributions and the condition numbers show that, regardless of the system being under-determined or over-determined, the problem is ill-posed. Aforementioned phenomenon about the uniqueness of the solution is still valid for the over-determined solution, since the matrix of size 771×490 is rank-deficient to the working precision ($rank(\mathbf{A}) = 355$), hence even for the multiple measurement case, the inverse solution has both existence and uniqueness problems. The $\mathcal{L}_2$-norm condition numbers $\boldsymbol{\kappa}_{sparse}$ and $\boldsymbol{\kappa}_{fine}$ are also given in the title of the figure as 5.95×10^{12} and $6,2 \times 10^{13}$ respectively, which validates the ill-conditionedness of the system matrix regardless of the over-determined or under-determined properties of the matrix. Hence, regardless of the number of measurements, the uniqueness problem persists due to the nature of the forward problem.

3.3 Evaluation Metrics

This section is devoted to the evaluation methods of the results that will be presented in the next two sections. The ground-truth will be denoted as $\mathbf{z}$ and the solution matrix to the equation Eqn. (2.6) will be denoted as $\hat{\mathbf{z}}$. For post-reconstruction performance

evaluation of the imaging problem, two metrics are used. The first one is relative error (RE) metric that is measure of the Euclidean distance between the reconstruction and the ground-truth:

$$\text{RE} : \frac{||\hat{\mathbf{z}} - \mathbf{z}||}{||\mathbf{z}||} \tag{3.1}$$

The second metric is Pearson's correlation coefficient (CC), which is defined as follows:

$$\text{CC} : \frac{(\hat{\mathbf{z}} - \bar{\hat{\mathbf{z}}})(\mathbf{z} - \bar{\mathbf{z}})^T}{N\sigma_{\hat{\mathbf{z}}}\sigma_{\mathbf{z}}} \tag{3.2}$$

where N is the dimension of the vector $\mathbf{z}$ and σ is the standard deviation with the following definition:

$$\sigma_{\mathbf{z}} = \sqrt{\sum_{i=1}^{n} \left(\mathbf{z}(i) - \bar{\mathbf{z}}(i)\right)^2} \tag{3.3}$$

where $\mathbf{z}(i)$ represents the i^{th} entry of the vector $\mathbf{z}$.

Note that $\mathbf{z_i}$ vectors in Equations (3.1) and (3.2) can be in the column format as in Eqn. (2.5). If this format is adapted, the computed metric is the spatial metric. If, on the other hand, vector $\mathbf{z}$ is defined as ${\mathbf{x}_k}^T$, then the temporal metric is computed. These metrics can be evaluated in both spatial and temporal direction of the reconstruction. Referring to Figure 2.8, the temporal metrics corresponding to measuring the correlation and error between the rows of the matrix, whereas the spatial metrics is defined to compare the spatial distribution of the signals, which is represented by the rows. Therefore, each time temporal metrics are computed, a vector of length N is generated whose entries represent the performance of the reconstruction of each lead. In the spatial case, the dimension of the vector is the number of time instances T in the reconstruction. When presenting the results, a summarized metric (using either mean$\pm$std or median(IQR)) is used.

The accuracy of the inverse solution only determines the quality of the reconstruction. However, to obtain clinically meaningful and impactful results, some post-processing

techniques are applied to the inverse solution depending on the nature of the inverse ECG task. Pacing site localization, *i.e.* locating the origin of signal propagation on the cardiac surface, is one of the most used post-processing technique to provide clinicians with meaning information prior to pre-surgical operations to treat diseases such as PVC and AF. For localization, the activation time method is used.

3.3.1 Activation Time

By definition, activation time is the time instance when the sharpest drop in the voltage is observed throughout the EGM. Once the activation times of all the heart nodes are computed, the node having the smallest activation time is considered to be the origin of the beat propagation (or pacing site) and labelled as such.

The naïve method to find the activation time maps is to apply first order derivative to the EGMs. The time index having the minimum (negative) value is marked as the activation time. Due to the noise and the smoothing in the inverse reconstruction, the activation time maps computed with the naïve approach are usually erroneous. To overcome this, some regularization methods have been proposed using the features of the geometry. In [153], the authors used Laplacian of the geometries on the computed solution as spatial regularization and the distance to the naïve solution as temporal regularization. In another study, Duchateau *et al.* utilized the graph-incidence matrix to impose the latency constraint computed from the signals using cross correlation [154]. A more detailed review and the comparison of these approaches can be found in [155]. In this thesis work, the spatially coherent activation time mapping approach in [154] is used for the computation of activation times, due to the amount of balanced regularization it applies.

The database already have the ground-truth stimulation site, hence the ground-truth pacing locations are already known. Hence, in the following sections, the correlation coefficient of activation time maps and the localization error will be presented as a performance comparison metric. For localization error, the Euclidean distance between the ground-truth and the found pacing site is calculated. Since the geometry is an open epicardial heart geometry and the accuracy of the localization is sufficient, geodesic distance, the distance calculated from the surface, is not utilized for the

calculation of the localization error in this study.

CHAPTER 4

PRIOR MODEL SELECTION VIA EVIDENCE AND COVARIANCE

4.1 Introduction

In Section 2.7.1.6, the statistical approaches to solve the inverse problem of ECG was explained. For these methods, the main usage of training data is to infer the parameters that determine the distribution of the prior pdf. Methods developed so far employed greedy approaches to form the training set, such as sampling the prior pdf from the proximity of the Tikhonov-estimated solution's pacing site. In this section, a procedure to assess the representation capability of a subset of data and finding a subset as performant as the whole database is presented. One of the earliest attempts to quantify the performance of the training data prior to reconstruction was in [89]. The authors used evidence, *i.e.* the marginal pdf of the measurement $\mathbf{y}$, to numerically sort the likelihood of the training set's representation capability of the measurement. Following this idea, this chapter introduces two metrics and regarding selection strategies that can be utilized to determine the representation capability of a subset of the training data before the reconstruction process. The strategies are built upon the Bayesian MAP framework. To introduce the assumption, Eqn. (2.5) is revisited to remind the system formulation:

$$\mathbf{y_k} = \mathbf{A}\mathbf{x}_k + \mathbf{n}_k,\ k = 1, 2, 3, \ldots, T \tag{4.1}$$

In this study, $\mathbf{x}$ is assumed to be Gaussian distributed with mean $\bar{\mathbf{x}}$ and covariance matrix $\mathbf{C_x}$; *i.e.*, $\mathbf{x} \sim N(\bar{\mathbf{x}}, \mathbf{C_x})$. The noise vector $\mathbf{n}_k$ is assumed to be independent and identically distributed (i.i.d) with a Gaussian distribution, $(\mathbf{n}_k \sim N(\mathbf{0}, \mathbf{C_n}))$, where $\mathbf{C_n} = \sigma_n^2\mathbf{I}$. Furthermore, it is assumed to be uncorrelated with the epicardial

potentials. With these definitions, the marginal distributions of epicardial potentials $\mathbf{x}$, measurements $\mathbf{y}$ and noise $\mathbf{n}$ is as follows:

$$p(\mathbf{x}) = \frac{1}{(2\pi)^{\frac{N}{2}}|\mathbf{C_x}|^{\frac{1}{2}}} e^{-\frac{1}{2}(\mathbf{x}-\bar{\mathbf{x}})\mathbf{C_x}^{-1}(\mathbf{x}-\bar{\mathbf{x}})^T} \tag{4.2}$$

$$p(\mathbf{n}) = \frac{1}{(2\pi)^{\frac{M}{2}}|\sigma_\mathbf{n}^\mathbf{2}\mathbf{I}|^{\frac{1}{2}}} e^{-\frac{1}{2}(\mathbf{n})\sigma_\mathbf{n}^\mathbf{2}\mathbf{I}(\mathbf{n})^T} \tag{4.3}$$

$$p(\mathbf{y}) = \frac{1}{(2\pi)^{\frac{M}{2}}|\mathbf{A}\mathbf{C_x}\mathbf{A}^T + \sigma_n^2 I|} e^{-\frac{1}{2}(\mathbf{y}-\mathbf{A}\bar{\mathbf{x}})(\mathbf{A}\mathbf{C_x}\mathbf{A}^T+\sigma_n^2\mathbf{I})^{-1}(\mathbf{y}-\mathbf{A}\bar{\mathbf{x}})^T} \tag{4.4}$$

where $\mathbf{A}$ is an $M \times N$ forward system matrix, and the time subscripts of the variables are dropped for convenience since the prior model is assumed to be stationary throughout the beat.

The Bayesian MAP solution can be expressed in closed form as:

$$\hat{\mathbf{x}}_\mathbf{MAP} = \left(\mathbf{A^T}\mathbf{C_n^{-1}}\mathbf{A} + \mathbf{C_x^{-1}}\right)^{-1}(\mathbf{A^T}\mathbf{C_n^{-1}}\mathbf{y} + \mathbf{C_x^{-1}}\bar{\mathbf{x}}) \tag{4.5}$$

The two parameters that completely define the multivariate Gaussian prior pdf, mean $\bar{\mathbf{x}}$ and covariance $\mathbf{C_x}$, appear in the solution expression. The motivation of selecting a performant set of prior model parameters is based on the idea that increasing the value of the marginal pdf at the measurement location is possible by shaping the marginal pdf by tuning the prior model's parameters. In other words, the training data that results in higher evidence provides better match to the observed measurement, hence is a better representation of the solution that caused the measurement formation. The hypothesis is that the performance of the reconstruction can be improved by carefully selecting a subset of data from which the estimated mean and covariance maximize the evidence.

The evidence formulation, given the prior model parameters $H^{(i)} = (\bar{\mathbf{x}}^{(i)}, \mathbf{C_x^{(i)}})$ is as follows:

$$p(\mathbf{y}|H_i) = \frac{1}{(2\pi)^{\frac{M}{2}}|\mathbf{C_y}^{(i)}|^{\frac{1}{2}}} \cdot e^{-\frac{1}{2}(\mathbf{y}-\mathbf{A}\bar{\mathbf{x}}^{(i)})^T(\mathbf{C_y}^{(i)})^{-1}(\mathbf{y}-\mathbf{A}\bar{\mathbf{x}}^{(i)})} \tag{4.6}$$

where M is the measurement domain dimension and $\mathbf{C_y} = \mathbf{A}\mathbf{C_x}\mathbf{A}^T + \mathbf{C_n}$. The

detailed derivation is given in Chapter 7. By representing the evidence parameters in terms of prior model parameters, one can control the prior model performance. The numerator in this equation measures the inverse-covariance-weighted prior mean match to the measurements. The denominator is the normalization term. Taking the logarithm of this expression has advantages in the working numerical precision in the computation of the determinant using the eigenvalues.

$$\begin{aligned}\log(p(\mathbf{y}|H_i)) = &-\frac{M}{2}\log(2\pi) - \frac{1}{2}\log(|{\mathbf{C}_\mathbf{y}}^{(i)}|) \\ &-\frac{1}{2}\log\left((\mathbf{y}-\mathbf{A}\bar{\mathbf{x}}^{(i)})^T({\mathbf{C}_\mathbf{y}}^{(i)})^{-1}(\mathbf{y}-\mathbf{A}\bar{\mathbf{x}}^{(i)})\right)\end{aligned} \tag{4.7}$$

In this section, the proposed procedure to find the best representative set without first performing the inverse reconstruction is presented. The procedure is composed of two steps:

1. **Dataset Expansion:** In the first step, the training beats in the available database are sorted by the proposed metrics.
2. **Termination:** The proposed termination criterion specifies under what circumstances related to the metrics in the first step the dataset expansion should stop.

The proposed metrics heavily depends on the utilization type of the training data. To comprehend why these metrics are proposed, how the prior model parameters are estimated using training data should be inspected.

4.2 Estimating the prior model parameters

In this study, the unbiased maximum likelihood estimators of mean and covariance are utilized to determine the prior model parameters from the training set, as in [89,90, 106,156,157]. To estimate the parameters, the training dataset explained in Chapter 3 is used. In this approach a subset of training beats are concatenated in the temporal dimension, treating them as different realizations of the same multivariate random

variable. The steps to perform the expansion of training data can be summarized with sample beats $\mathbf{X_1}$ and $\mathbf{X_2}$ in these steps:

- The beats concatenated along the time axis (in horizontal direction) to form the new training data $\mathbf{X} = [\mathbf{X}_1\mathbf{X}_2]$.
- The mean along the time axis $\bar{\mathbf{x}}$ is calculated by averaging the different realizations of random variables, *i.e.* the columns of the matrix $\mathbf{X}$.
- The covariance $\mathbf{C_x}$ is calculated using the unbiased maximum likelihood covariance estimator $\frac{N}{N-1}(\mathbf{X} - \bar{\mathbf{x}})(\mathbf{X} - \bar{\mathbf{x}})^T$, where N is the signal domain dimension or the number of epicardial sources.

4.2.1 Variance in the training set

The dataset used in this study contains beats stimulated from different regions of the epicardial surface. The distribution of these locations are plotted in Figure 3.1. It is observed that the variance of EGMs along the time axis (temporal variance) in different training beats have different patterns. The temporal variance across the beats is observed to exhibit dependent pattern on the stimulation location, *i.e.* pacing site, as in Figure 4.1.

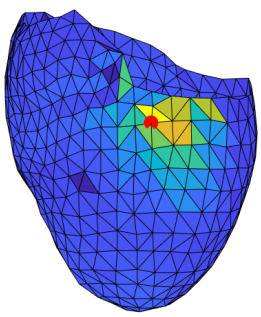

(a) Left ventricle stimulation.

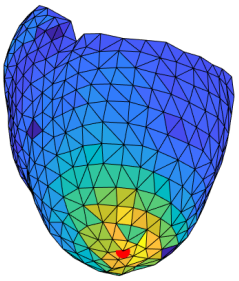

(b) Apex stimulation.

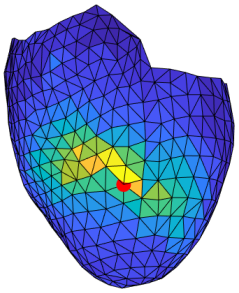

(c) Right ventricle stimulation.

Figure 4.1: Spatial map of the temporal variance of the EGM signals in different training beats are shown. The red dot represents the stimulation point where the signals start to propagate on the epicardial surface. The patterns illustrate that the amplitude of the fluctuations in the proximity of the pacing site is higher than the rest of the epicardial surface.

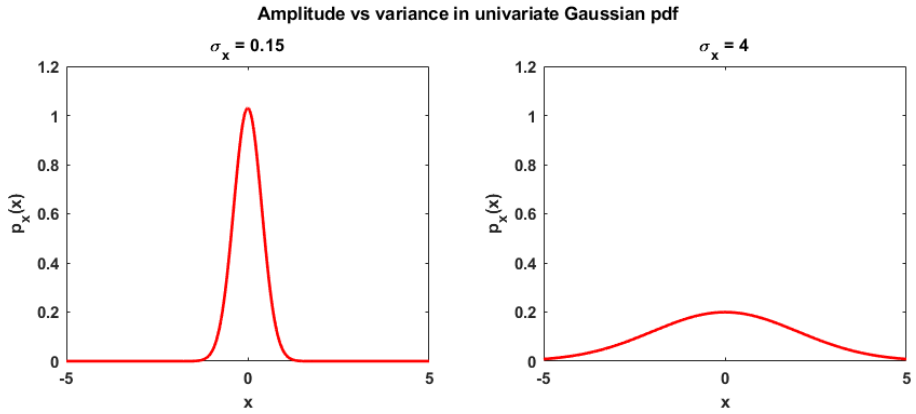

Figure 4.2: The voltage distribution in one epicardial node has univariate normal distribution. Concatenation of different realizations for this random variable using beats having different variances as in Figure 4.1, results in increased variance, hence attenuated marginal pdf.

Including beats in the training set paced from diverse locations on the heart surface increases the variance of the distribution, hence results in a decreased value of evidence due to pdf normalization. This relationship for one univariate random variable is shown in Figure 4.2. The evidence for a test beat is calculated for every time instance in a single computation and evidence for each time instance is generated. In the following sections, the expansion algorithms will be explained. Before that, the reader is encouraged to have a look at Figure 4.5 to gain an immediate and concrete understanding of the training set expansion.

4.2.2 Evidence

The first metric utilized in this study whose relationship with dataset's prior representation is evidence. In Figure 4.3, the logarithm of the evidence is plotted against time for a sample test beat, for two arbitrarily composed training set from the available training database.

Since, the evidence has tendency to fluctuate thorough out the beat as in Figure 4.3, the median is used as a comparison metric to evaluate the evidence differences of training beats.

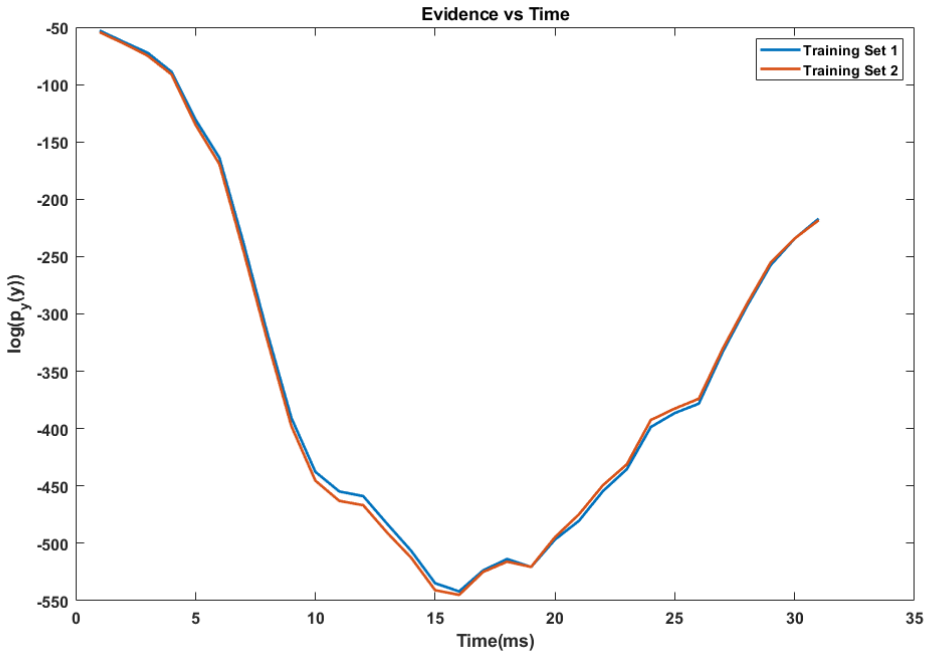

Figure 4.3: Logarithm of evidence vs time for two training sets. Depending on the time instance of the measurement, the "best" model in terms of evidence may change.

To test the hypothesis that higher median evidence match is an indicator of a better representative training set, Algorithm 1 is implemented. This algorithm starts by including the training beat that results in the highest evidence of the given measurement into the cumulative training set, which will be the final training set once the iterations are completed. In the second iteration, the algorithm expand the cumulative training set that is only composed of one beat with every other beat in the training set and calculate the resultant evidence. Although the value of the median evidence decreases in the second iteration, the algorithm maximizes the evidence for fixed-level of variance in the training set, assuming that the number of included beats are proportional to the variance within the cumulative dataset. Hence, it maximizes the evidence in a variance-aware manner.

4.2.3 Covariance

Due to the spatially dense discretization of the heart, the signals sampled from the surrounding nodes of an arbitrary node on the epicardial surface are expected to be

Algorithm 1 Iterative Variance-Aware Evidence Maximization.

Require: N training beats, test beat, forward model

1: Allocate empty array for cumulative training set
2: **for all** Training beats **do**
3: Calculate evidence given by Eqn. (4.7)
4: Sort the evidence according to the median values along the time axis.
5: Include the beat that has the highest mean evidence in the cumulative training set
6: **end for**
7: **while** Beats in database > 0 **do**
8: Concatenate each of training beats to the cumulative training dataset.
9: Include the one resulting in the highest evidence in the cumulative training dataset.
10: Exclude the beat from the database.
11: **end while**
12: **return** Sorted cumulative training set

correlated with the center node. Hence, the cross correlations are observed to be nearly close to the variance, *i.e.* off-diagonal entries corresponding to these neighboring nodes are comparably as large as the diagonal entries of the covariance matrix. Hence, especially within a single beat, the covariance matrix tends to be ill-conditioned with $\boldsymbol{\kappa}(\mathbf{C}_{\mathbf{x}}) \approx 10^9$. In addition to the role of covariance in normalizing the evidence implicitly, the determinant of the ill-posed (or nearly-rank deficient) covariance matrices results in the amplification of the pdf (see Eqn. (4.7)), hence the value of the evidence thorough the covariance of the measurements. Furthermore, the inverse of the epicardial covariance matrix the appears in the solution expression (Eqn. (4.5)), it is important to have a stable inverse to estimate a stable solution. Thus, a stabilized inverse of the covariance matrix is needed for the proper estimation of the solution.

The second metric to assess the dataset representation of the prior is determined as the $\mathcal{L}_2$-norm condition number of the covariance matrix. By using this approach, the biased estimation of the prior model parameters due to the unbalanced temporal variance across the surface in the training data can be avoided. The algorithm that

exploits this property is presented in Algorithm 2.

Algorithm 2 Iterative Covariance-Condition-number minimization.

Require: N training beats

1: Allocate empty array for cumulative training set
2: **for all** Training beats **do**
3: Calculate the condition numbers of the covariance matrices
4: Sort the condition numbers in the ascending direction
5: **end for**
6: **while** There exist remaining beats in the dataset **do**
7: Concatenate each of the training beats to the cumulative training dataset.
8: Include the beat resulting in the lowest condition number of the covariance matrix in the cumulative training dataset.
9: Exclude the beat from the database.
10: **end while**
11: **return** Sorted dataset

Algorithm 2 starts by finding the beat that has the most-balanced temporal variance distribution among the nodes by the utilization of condition number. Following that, each of the training beats are concatenated to this "best" beat and the condition numbers of the covariance matrix for this concatenated training set is calculated iteratively until there is no remaining beat in the dataset.

So far, the expansion of the training set has been illustrated. The subsequent section will delve into an explanation of the termination criterion.

4.2.4 The Termination of the Expansion

For both of the algorithms, the termination criterion is determined as the saturated condition number of the covariance. For this, Algorithm 3 is implemented.

The algorithm employs a greedy approach to find when to stop the expansion process. For this, the condition number of the covariance is tracked during the expansion strategies. The ratio between the condition number of the covariance matrix between the consecutive iterations is observed. The expansion is terminated by the saturation

Algorithm 3 Termination of Training Set Data Expansion.

Require: A training set composed of N training beats sorted by either Algorithm 1 or Algorithm 2, Hyper parameters: ϵ (margin), n (number of occurrences).

1: **for all** Prefix subsets of the cumulative training set **do**
2: Calculate the $\mathcal{L}_2$ norm condition number of the training set's covariance matrix.
3: **end for**
4: Calculate the ratios of condition numbers between the consecutive levels of expansion.
5: **while** $N > 0$ **do**
6: Search for n consecutive occurrences where ratio remains between $1 \pm \epsilon$ starting from the end of the training set.
7: **if** n occurrences found **then**
8: **return** Index of the first occurrence
9: **else**
10: $n \leftarrow n - 1$
11: **end if**
12: **end while**

condition. The saturation condition is satisfied when the consecutive ratio of the condition number of the covariance matrix remain between the range $1 \pm Margin$ for N consecutive occurrences. The hyperparameters n and ϵ of Algorithm 3 is determined experimentally as 20 and 0.05. A high margin provides better stabilization to the termination, whereas the high number of occurrences provides reliability of saturation of the condition number. The effect of a better conditioned covariance matrix can be seen in Eqn. (4.5), where in the ill-conditioned cases the inverse of it dominates the first factor in the expression and hence the contribution of the forward matrix. The point where the covariance gets well conditioned may indicate a point where a good trade-off between the prior and forward matrix is caught.

4.3 Results

The evidence algorithm is run for every test beat, whereas the covariance algorithm is run only once, since it is independent of the measurement. The results regarding

one particular test beat can be seen in Figure 4.5. The training set index is a measure of how large the accumulated training set index at that iteration, since the algorithm performs expansion including one beat at each iteration.

In Figure 4.4, the reconstruction metrics of all the test are concatenated and plotted together. The data utilization ratio of the evidence selection algorithm can be seen in Table 4.2. On average, the evidence algorithm used 81% of the available database whereas the covariance algorithm found a dataset composed of 82 beats, resulting in a utilization ratio of 26.5%. The results show that it is possible to achieve the reconstruction on the overall test dataset with the generalization of the whole training dataset with a careful selection of the training data.

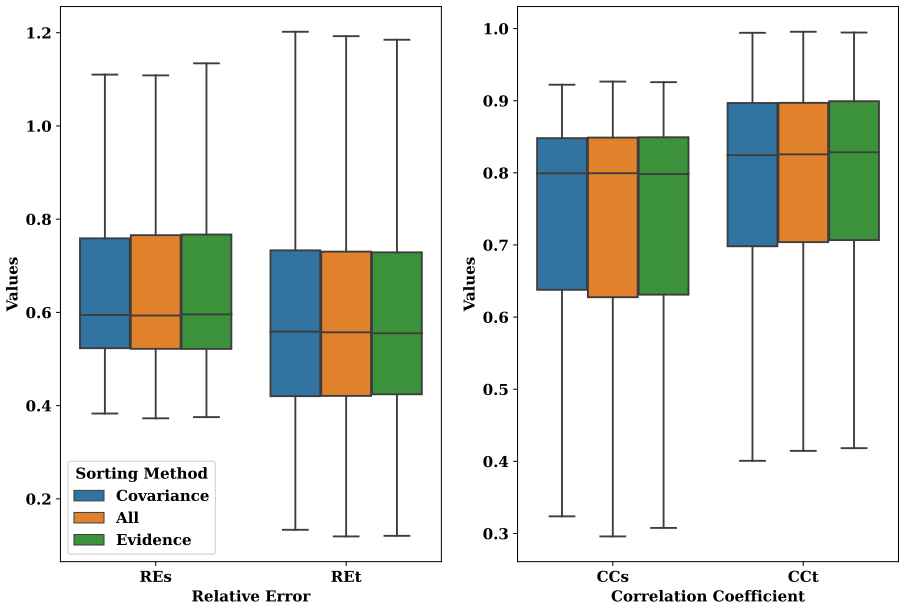

Figure 4.4: RE and CC comparison for the whole test dataset's reconstruction. (Outliers are not shown.)

For quantitative analysis, paired-sample Student's t-test is utilized to investigate if there is statistically significant difference between the metric distributions given by the whole dataset. The results have shown that covariance algorithm was able to find a single training set from the available training database for all test beats that matches distribution of the performance metrics given by the whole dataset, except for test

data 6. Evidence on the other hand, have exhibited similar performance that matches that of all training set except for test data 6 and 8, with alpha-significance level 0.05. In Figure 4.5, the mutual outlier result, test data 6, is inspected. Although the t-test did not yield statistically significant similarity, the summarized metrics (mean $\pm$ std) produce similar results, with performance loss by 1.4% in temporal RE and 2% in temporal CC. Likewise, the temporal CC distribution of test data 6 in Figure 4.7 exhibits significant similarity to the metric distribution provided by the whole dataset. Hence, although the t-test results may indicate similar performance to the all training set, the scenarios where t-test indicated statistically significant difference do not necessarily imply poorer performance. For the temporal RE and temporal metrics' distribution for the whole test data, see Section 7.2.

Table 4.1: p-values for Student's t-test for concatenated metric distributions.

Test Data	Covariance	Evidence
1	0.698	0
2	0.917	0.05
3	0.684	0.729
4	0.935	0.623
5	0.443	0.073
6	0.027	0.006
7	0.065	0.862
8	0.555	0.023
9	0.785	0.318
10	0.802	0.568
11	0.884	0.406
12	0.284	0.816
13	0.756	0.567
14	0.378	0.671
15	0.802	0.346
16	0.156	0.479
17	0.192	0.693

As mentioned earlier in Chapter 3, solely presenting the epicardial voltage map re-

constructions are not sufficient for the datasets utilized in this study, since the main aim is to localize the pacing site. For this, activation time maps are calculated, and the corresponding metrics are illustrated in Table 4.2.

Table 4.2: Activation CC and localization error (**Evi**: Evidence, **Cov**: Covariance)

Test	LE (mm)			AT-CC			Evidence Data
Data	Evi	Cov	All	Evi	Cov	All	Usage (# Beats)
1	9.58	7.66	7.66	0.82	0.93	0.93	249
2	12.03	10.35	10.35	0.93	0.96	0.97	280
3	9.38	13.53	13.53	0.97	0.98	0.99	248
4	10.02	4.1	4.1	0.97	0.99	0.99	265
5	11.7	11.19	11.19	0.97	0.99	0.99	253
6	26.52	8.39	8.39	0.97	0.99	0.99	271
7	0	8.45	8.45	0.92	0.98	0.98	275
8	6.95	3.85	3.85	0.96	0.99	0.99	254
9	7.55	5.16	5.16	0.84	0.92	0.88	245
10	0	19.87	16.71	0.84	0.93	0.93	238
11	4.69	5.73	5.73	0.89	0.94	0.94	239
12	8.8	0	0	0.83	0.96	0.95	259
13	7.26	5.24	5.24	0.92	0.99	0.99	254
14	7.13	5.13	5.13	0.98	1	1	172
15	4.07	5.82	5.82	0.88	0.89	0.91	243
16	0	5.67	5.67	0.89	0.87	0.83	258
17	4.61	8.76	9.6	0.81	0.9	0.91	257
mean	7.66	7.58	7.45	0.91	0.96	0.95	250.29
std	6.19	4.48	4	0.06	0.04	0.05	23.52

Although the correlation is 1% higher in the covariance case on average, the localization error is slightly higher. When the results are inspected separately for each test data, we observe that covariance-produced results matched that of the all training set except for test data 10, which is the reason for the difference of 0.13 mm LE on average. This specific case can be seen in Figure 4.6. Furthermore, evidence-produced results show similar localization performance to the remaining algorithms, although

it results in 5% lower average correlation coefficient. However, the standard deviation in LE is 38% and 51% higher than the covariance and all dataset standard deviations respectively.

It is observed from the wide-spread blue region (the earliest activated) that all the solutions smooth out the activation time maps and loosens the isochrones, indicating that the Bayesian MAP inverse operator delays the solution. From Figure 4.5, it is possible to observe the difference in the convergence speed of standard deviation ranges. The standard deviation of the temporal metrics are ceases to decrease. For temporal metrics, this implies that the reconstruction are more stable on the whole surface of the heart, *i.e.*, in between the heart nodes. In the covariance algorithm, the temporal metrics' standard deviation stabilizes after a couple of iteration, whereas in the evidence scenario, the stabilization required approximately 40 iterations. This might indicate that the balanced estimation of the spatial covariance prior resulted in a faster convergence of spatially balanced performance over the epicardial surface.

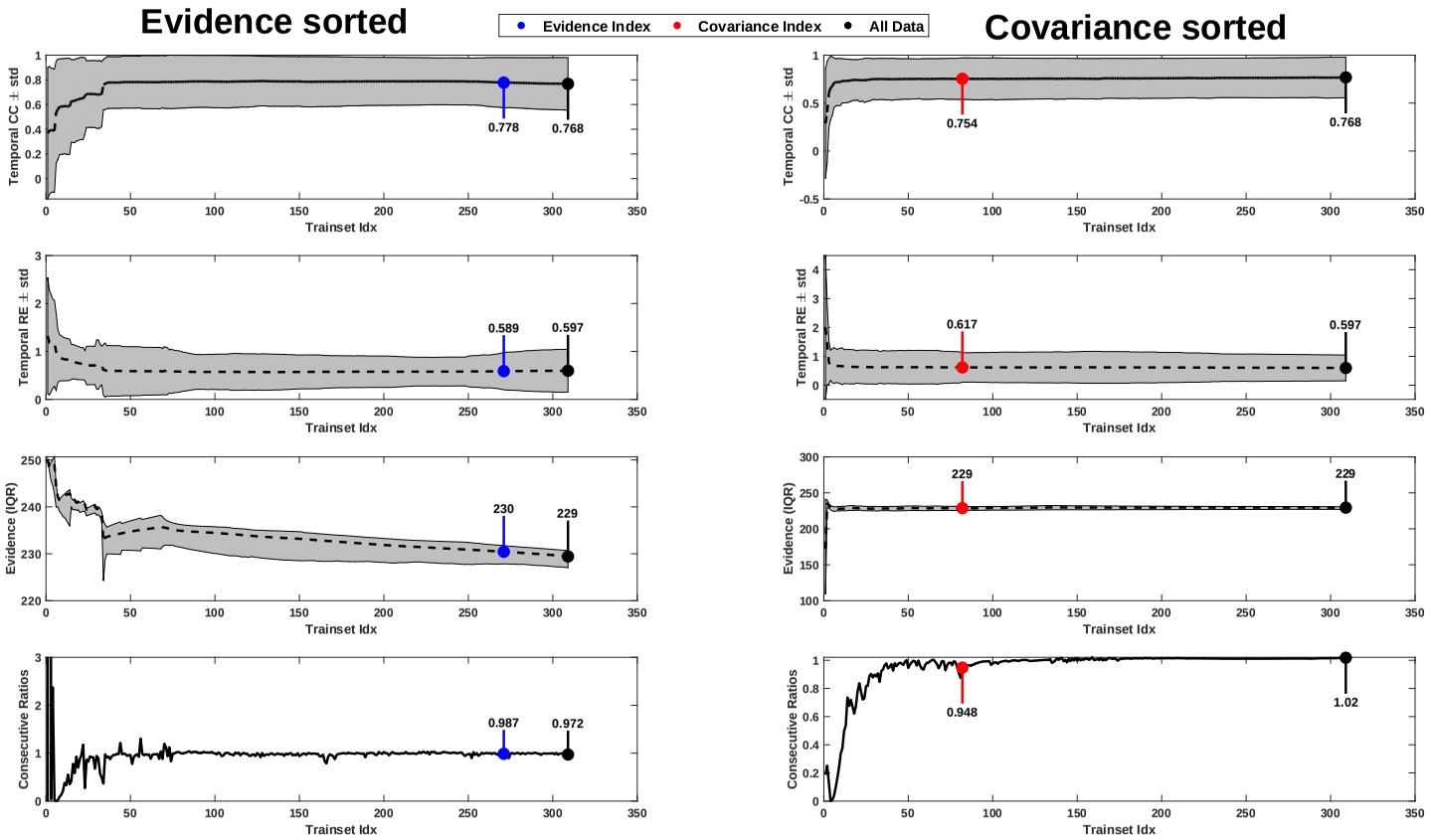

Figure 4.5: The trend of the temporal metrics, evidence and the consecutive condition number ratio for test data 6. The training set indices pointed out by Algorithm 3 is labelled with the corresponding value of the quantity. The whole dataset is used as a benchmark. The mean of the metrics are shown as dashed line and the gray regions represent the standard deviation. For the evidence metric, dashed-line depicts median and gray area shows the region between lower and upper quartile. For covariance method, the evidence is shown to provide the trend of the metric where the expansion stops for informative purposes.

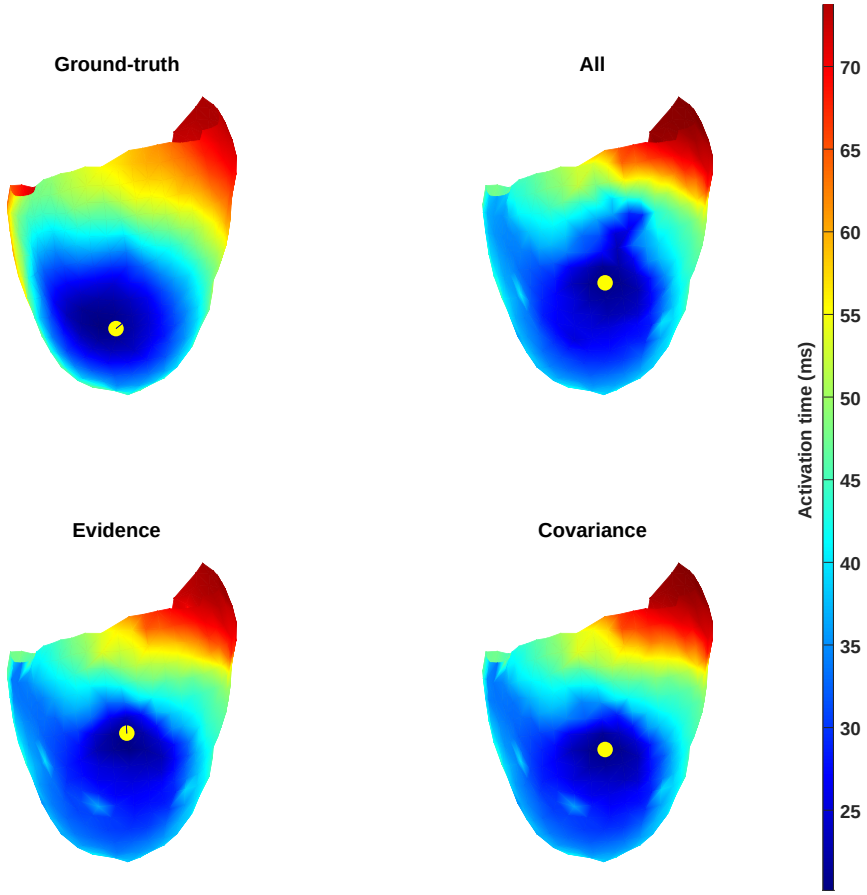

Figure 4.6: AT maps computed from 3 different algorithms plotted on the epicardial surface. The pacing locations, the minimum AT point, is marked with a yellow dot.

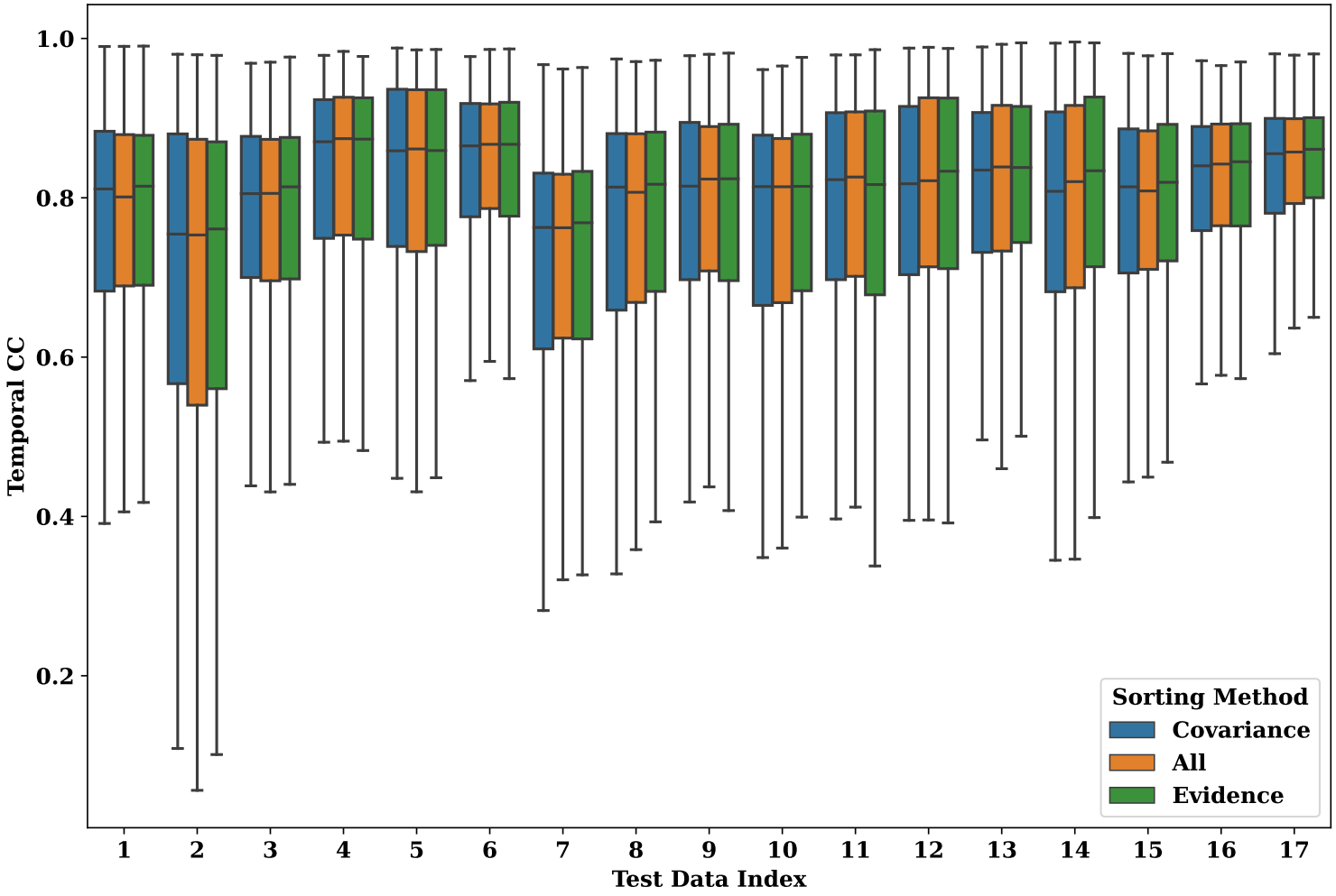

Figure 4.7: Temporal correlation coefficient distribution of 17 test beats for 3 different training datasets.

4.4 Discussion

In this study two methods are proposed for sorting the training set beats sorted by their (proposed) capabilities of resulting in better performance. The evidence approach generates a different training data for every inference case due to its definition involving the measurements.

The covariance approach, on the other hand, generated a single training dataset from the whole available training database. The covariance approach, by achieving the competitive performance to that of the whole training dataset. The condition number of the covariance matrix is closely related to the principal component analysis (PCA) [158]. PCA is a dimension reduction technique. It calculates the eigenvalues of the covariance (scatter in PCA terminology) matrix to find the dimension having the most scatter. The dimensions corresponding to the highest eigenvalues carry more information about the variance of the data, hence the data can be represented in lower number of dimensions. The covariance approach proposed here, optimizes the implicit cross-correlation (variance in the i.i.d. epicardial potential case) patterns, formulated by the condition number of the covariance. By doing so, the variability coming from different stimulating location are automatically considered, and spatial variance is estimated as unbiased as possible for any arbitrarily paced data one the same geometry. Although the test data contain the realizations drawn from different distributions, the selected subset of covariance condition number minimizer data was able to represent 4 different distribution of training data's spatial covariance and is performant on all distributions on the test data.

It is important to note that this study proposed a method to evaluate the training data information content in the context of prior model formation in MAP-based ECGI. It does not provide the "best" composition in a given database. In real life scenarios, the approach can be used to determine the sufficiency of limited training data for the estimation. Furthermore, the iterative nature of it allows an online scheme where every incoming training data can be assessed continuously.

4.5 Limitations and Future Work

The proposed procedure is only applied to the Bayesian-MAP formulated inverse problem of electrocardiography. Following items should be tested to generalize the usage of the procedure to other settings:

- Due to the choice of Gaussian priors, the covariance matrices appeared directly in the solution. It is important to validate the performance under different choice of priors.
- The experiments are conducted utilizing one dataset, due to the limited data that can be accessed in the field of ECGI. The experiments should be repeated with other available datasets.
- In the experiments, the potentials simulations are conducted with one geometry and the geometric errors are not accounted for in this study. The method should be tested in an environment where the geometry is also a control variable.

As an advantage, the utilization of the approach can be tested in a similar framework for a different problem, such as Bayesian-MAP based image restoration problem with Gaussian priors. Since the forward and inverse models are arbitrary and there is no specific assumption imposed on them, this step will increase the reliability of the generalization of the method to other inverse problems with different forward operators.

CHAPTER 5

PHYSICS-BASED AI-ASSISTED SOLUTION TO ECGI

In Section 2.7.2.2, the current learning-based approaches were explained. None of them combined the physics-based knowledge with just using the forward model in the original signal and measurement domain. In this section, the inverse problem is reformulated to be integrated with learning-based approach to avoid explicitly defining the prior. For this, **Half Quadratic Splitting** (HQS) method is used to split the variables on the problem, following the approach introduced in [159]. One of the recent attempts to use the approach in the setting of inverse problems by proposed by Zhang *et al.* [160]. They utilized a UNet [161] CNN for the proximal update step for the image restoration and single image super-resolution problem.

5.1 Theory

The inverse problem formulation defined in Eqn. (2.5) can be formulated by utilizing an implicit prior instead of assuming the shape of the prior. In such cases, variable splitting methods allows us to formulate the problem so that we can obtain the solution by alternatively optimizing the data fidelity term and the regularization term that corresponds to the a priori information we have about the oracle. In HQS method, the optimization equation given in Eqn. (2.8) is transformed into an optimization problem with the introduction of intermediate variable $\mathbf{z}$ and regularization parameter μ. The new constrained problem can be formulated as follows:

$$\hat{\mathbf{x}} = \arg\min_{\mathbf{x}} ||\mathbf{y} - \mathbf{A}\mathbf{x}||_2^2 + \mu\mathbf{R}(\mathbf{z}), \quad s.t. \ \ \mathbf{x} = \mathbf{z} \tag{5.1}$$

Then the problem can be formulated as an unconstrained problem as in Eqn. (5.2).

$$\mathbf{J}(\mathbf{x}, \mathbf{z}) = \frac{1}{2}||\mathbf{y} - \mathbf{A}\mathbf{x}||_2^2 + \mu\mathbf{R}(\mathbf{z}) + \frac{\lambda}{2}||\mathbf{x} - \mathbf{z}||_2^2 \tag{5.2}$$

Eqn. (5.2) can be split into two equations for alternating optimization on variables $\mathbf{x}$ and $\mathbf{z}$:

$$\mathbf{x_{k+1}} = \arg\min_{\mathbf{x}} \; ||\mathbf{y} - \mathbf{A}\mathbf{x}||_2^2 \; + \; \lambda||\mathbf{x} - \mathbf{z_k}||^2 \tag{5.3a}$$

$$\mathbf{z_{k+1}} = \arg\min_{\mathbf{z}} \; \frac{\lambda}{2}||\mathbf{z} - \mathbf{x_{k+1}}||_2^2 \; + \; \mu\mathbf{R}(\mathbf{z}) \tag{5.3b}$$

The expression in Eqn. (5.3a) measures how reconstruction matches the observation, hence data-fidelity. The solution to this expression can be found analytically as follows:

$$\mathbf{x_{k+1}} = (\mathbf{A^T}\mathbf{A} + \lambda\mathbf{I})^{-1}(\mathbf{A^T}\mathbf{y} + \lambda\mathbf{z_k}) \tag{5.4}$$

which is a Tikhonov variant that seeks a solution around a previous estimate. Equivalently, one can also consider the least squares solution to the augmented system as follows:

$$\mathbf{x_{k+1}} = \arg\min_{\mathbf{x}} ||\begin{bmatrix} \mathbf{A} \\ \sqrt{\lambda}\mathbf{I} \end{bmatrix}\mathbf{x} - \begin{bmatrix} \mathbf{y} \\ \sqrt{\lambda}\mathbf{z_k} \end{bmatrix}||_2^2 \tag{5.5}$$

When the regularization term in Eqn. (5.3b) is rewritten as in Eqn. (5.6a), the optimization step corresponds to denoising the image with Gaussian i.i.d. denoiser with noise level $\sqrt{\frac{\mu}{\lambda}}$ according to Bayesian probability [160], due to the $\mathcal{L}_2$-norm-squared data fidelity term with the implicit forward operator identity.

$$\mathbf{z_{k+1}} = \arg\min_{\mathbf{z}} \; \frac{1}{2\left(\sqrt{\frac{\mu}{\lambda}}\right)^2}||\mathbf{z} - \mathbf{x_{k+1}}||_2^2 \; + \; \mu\mathbf{R}(\mathbf{z}) \tag{5.6a}$$

$$\mathbf{z_{k+1}} = \text{Denoiser}\left(\mathbf{x_{k+1}}, \sqrt{\frac{\mu}{\lambda}}\right) \tag{5.6b}$$

This step is a proximal update that tries to minimize the regularization penalty in the proximity of the previous estimate coming from the data-fidelity update. In the ideal scenario, this regularization function is an indicator function where:

$$\mathbf{R}(\mathbf{z}) = \begin{cases} 0, & \text{if } \mathbf{z} \in \mathcal{X} \\ \infty, & \text{otherwise} \end{cases}$$

where $\mathcal{X}$ is the subspace where epicardial potentials live.

The alternating optimization steps for variables $\mathbf{z}$ and $\mathbf{k}$ are applied to incorporate the physics (the forward model) of the problem and the implicit prior to be learned by a denoiser neural network. The regularization term is going to be kept implicit, so that the CNN learns to apply proximal operator on the subspace that is unknown to us. For comparison, in the zero-order-Tikhonov where the regularization term is $\mathbf{R}(\mathbf{z}) = ||\mathbf{z}||_{\mathbf{2}}^{\mathbf{2}}$, this step would correspond to minimizing the energy of the solution in the proximity of the inverse estimate.

5.2 Method

To apply the formulation to the inverse problem of ECG, some pre-processing procedures should be performed. In this study,

- The reordering of epicardial nodes to increase the spatial correlation of the randomly stacked potentials
- Data normalization and reshaping to assure proper training of the neural network with LSTM and convolution layers

steps are carried out.

5.2.1 Node reordering in the unstructured grid

Due to the nature of the coordinate systems on which the signals in these problems are defined, CNN is a good choice to learn the prior. However, measurements and epicar-

dial signals of the ECGI inverse problem are defined on unstructured grids. The CNN kernels might indeed be able to learn the temporal dependencies in the matrix form of the epicardial signals in Eqn. (2.6). However, spatial features cannot be extracted this way since the ordering of the epicardial nodes, hence the rows of the matrix X, are arbitrarily numbered in the geometries' mesh generation stage. To overcome this and utilize CNNs for denoising, an algorithm to reorder the node numbering is implemented. The algorithm aims to decrease the mean of neighborhood orders in a convolutional neural network kernel, so that the kernels defined in regular grids can learn the features of the spatially relevant signals on the geometry. The neighborhood order between two nodes is defined by the number of edges in the shortest connecting path on the geometry graph. This node-sorting algorithm can be seen in Algorithm 4.

Algorithm 4 Skip-neighbor order minimizing node renumbering.

Require: Heart Geometry with N Nodes, StartOrder

Calculate neighborhood orders for every node up to 21st order.[1]
Number node 1 as 1 in the new ordering (CenterNode).
Remove the current node from the remaining nodes.
Add removed node to used nodes.
while There are still nodes to be renumbered **do**
  Assign new indices to the 1st-order, not-used neighbors of the CenterNode.
  Remove them from the remaining nodes and add them to the used nodes.
  Assign new indices to the 2nd-order, not-used neighbors of the CenterNode.
  Remove them from the remaining nodes and add them to the used nodes.
  Order ← StartOrder
  while Order < 22 **do**
    Calculate not-used, Orderth neighbors.
    for *node* in Orderth neighborhoods **do**
      if node is not renumbered yet **then**
        CenterNode ← *node*
        CenterNode added to used nodes and removed from remaining nodes.
      end if
    end for
    if CenterNode changed **then**
      break
    else
      Order ← Order + 1
    end if
  end while
end while
return New Numbering

To compare the original sorting, the consecutive neighborhood orders between consecutive nodes in the numbering are plotted in Figure 5.1. As it can be observed, the mean cost difference is negligible between 2 scenarios. However, the resorting

[1] Experimentally found order that contains the furthest node for every beat

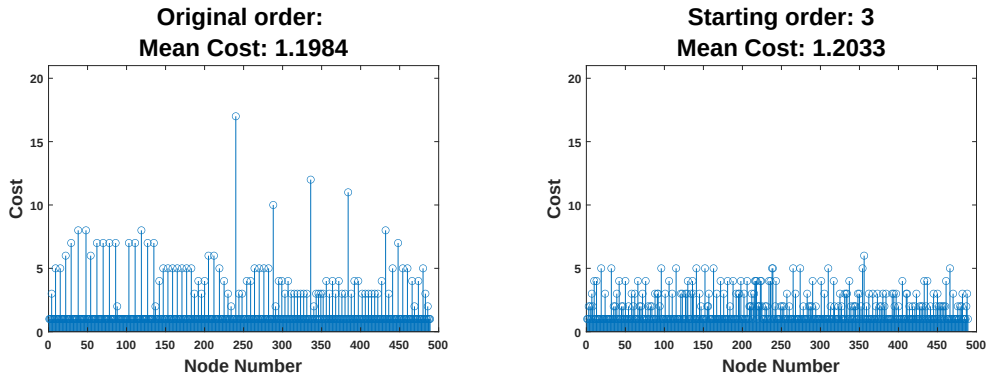

(a) Original Sorting

(b) Start Order: 3

Figure 5.1: Comparison of consecutive neighborhood orders in regular grid.

Table 5.1: Cross-neighborhoods for 3 sample nodes.

Node numbers	N1	N2	N3
N1	0	2	4
N2	2	0	3
N3	4	3	0

allowed us to minimize the distance in terms of neighborhood orders between consecutive nodes based on the numbering. The mean discontinuity was 4.65 before resorting, and it is reduced to 2.93. The calculated cost is the measure of mean cross-neighborhood orders given a window of 6, which matches the spatial dimension of the convolutional kernels in the CNN. For each consecutive 6 nodes, all the 15 $(C(6,2))$ order-differences are calculated, and the mean of neighborhood order distance is computed by subtracting one from each of the calculated entries, considering that obtaining a first order neighbor in the Euclidean grid is the best possible scenario. A sample calculation for cross-neighborhood cost can be seen in Table 5.1. The neighborhood orders between nodes N1, N2 and N3 are calculated. As expected, the diagonals are zero and the neighborhood matrix is symmetric. From the values in red, which corresponds to the cross-neighborhood orders, 1 is subtracted and the mean of them are calculated. In this specific case, the cost is calculated to be 2.

Figure 5.2 shows the distribution of the resorted nodes based on color. It can be

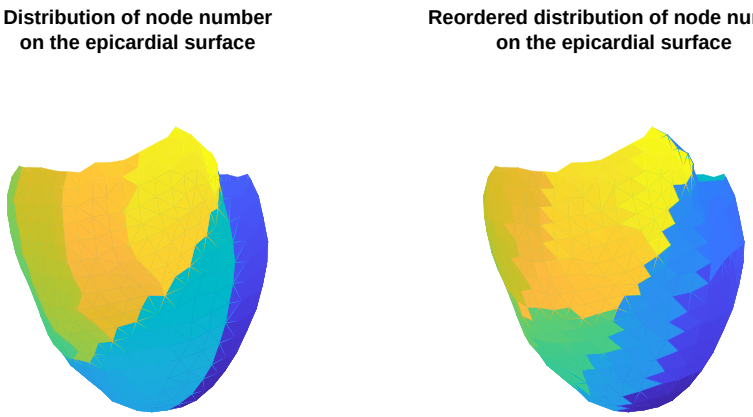

Figure 5.2: Spatial distributions of reordered nodes.

clearly observed that in the resorted geometry, the color discontinuities are smoother, which is an implication of node numbering is more suitable for the keeping the consecutively-numbered nodes correlated.

5.2.2 Unrolling the optimization

Equations (5.3a) and (5.3b) are optimized with via the data fidelity block corresponding to Eqn. (5.4) and the CNN denoiser network.

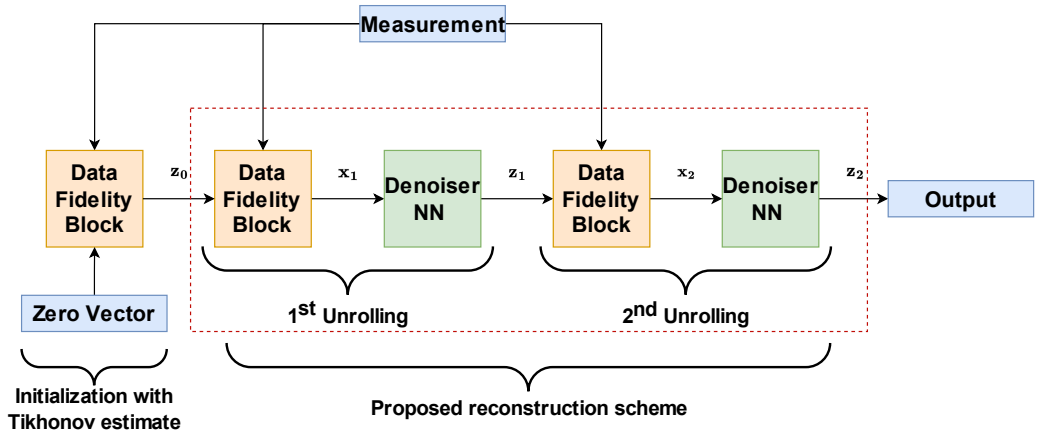

Figure 5.3: A sample architecture for HQS method for two unrolling iterations.

The data-fidelity block corresponds to the Tikhonov solution, when $\mathbf{z}_k$ in Eqn. (5.4) is taken as all 0 vector as in the earliest (the leftmost) block of the scheme given in Figure 5.3.

5.2.3 Data-Fidelity Block

The Tikhonov-variant operation that corresponds to data-fidelity block has only one design parameter. Along multiple iterations, depending on the noise level of the estimates, the regularization parameter that balances the trade-off between the data-model mismatch and the distance from the current estimate should be set.

The initial estimate to the input of this block, $\mathbf{x_0}$, is experimented with zero vector and zero-order Tikhonov estimate. For the first two blocks that produce the initial estimate and the **DFBlock** of first unrolling iteration, these values are determined using one of the most used classical methods in ECGI. The L-curve technique, which is highly convenient for finding the regularization parameter in BEM formulated problems [162], is used to find a convenient range of regularization parameter λ in Eqn. (5.3a). In this method, the norm of the constraint and the residual are plotted in logarithmic scale and the point that has the highest curvature is selected as the optimal point. These quantities are computed for each of the training sample in the dataset and the mean values are used to plot the L-curve in Figure 5.4.

Since the ground-truth data is already known, post-reconstruction metrics are also calculated with different regularization parameters to perform sanity check on what is found in the L-curve. The parameter sweep is conducted the same as before in the L-curve, by exponentially sweeping a wider region at first as in Figure 5.4a and then zooming into the promising region and performing a linear sweep as in Figure 5.4b. The resultant curves for parameter selection can be seen in Figures 5.5 and 5.6. In these experiments, for all the training data, CC and RE are calculated, and their mean values are plotted. These figures imply that the optimal parameter should be in the proximity of 1.75×10^{-4}, where CC peaks and RE has its lowest value.

The experiments conducted on the training data for both experiments showed that in 72% of the data, two-times Tikhonov estimation penalized with the previous estimate, *i.e.*, initialization with zero-order-Tikhonov estimate, resulted in better mean temporal RE. The optimal selection of regularization parameter for the zero-order Tikhonov estimate (the initial estimate in Figure 5.3) is 1.75×10^{-4}. The L-curve results also match this optimal parameter. Hence, the training process is initiated with the esti-

mates computed with this regularization parameter. The regularization parameter of the **DFBlock** in the first unrolling iteration is left initialized as this value and left as a trainable parameter to be learned by the neural network.

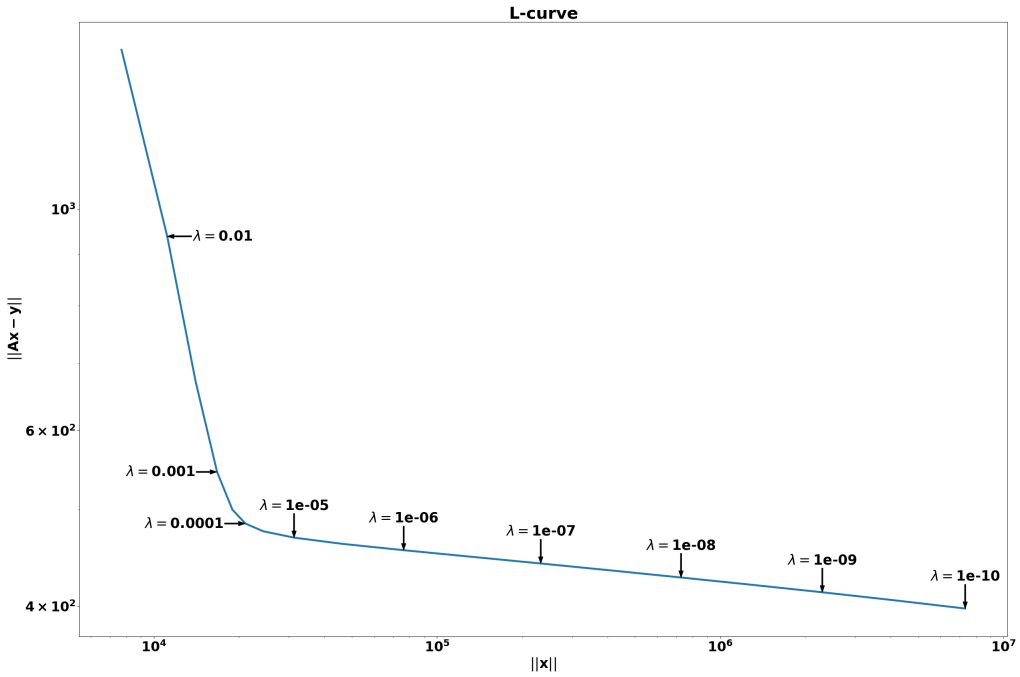

(a) Exponential Sweep

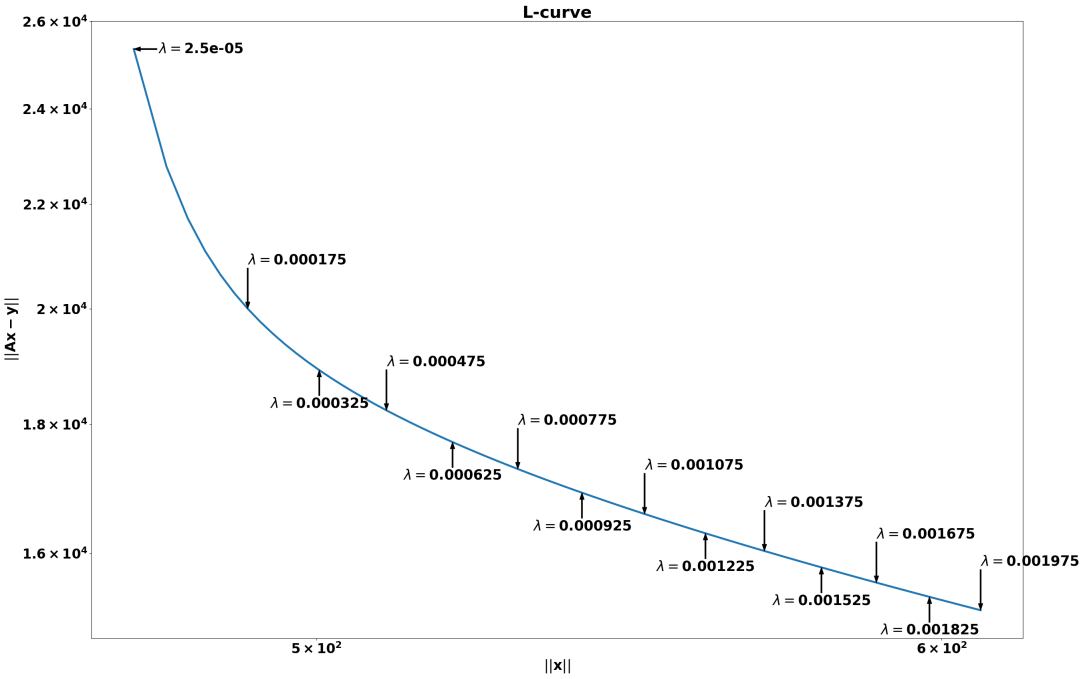

(b) Linear Sweep

Figure 5.4: L-Curve for exponential and linear sweeps.

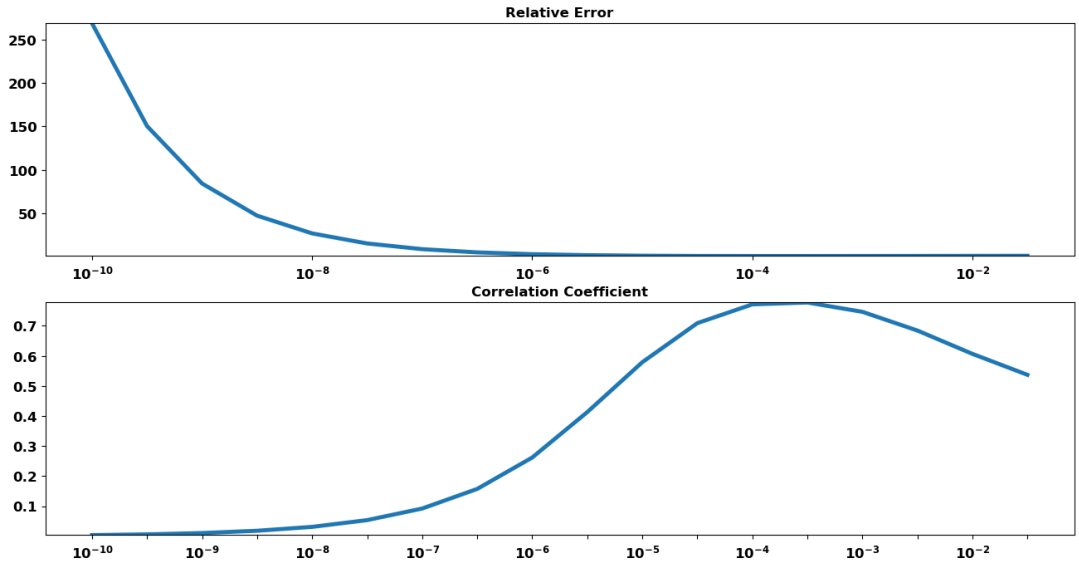

Figure 5.5: Exponential sweep of regularization parameter and post-reconstruction metrics for the whole training dataset. The mean values of RE and CC are plotted.

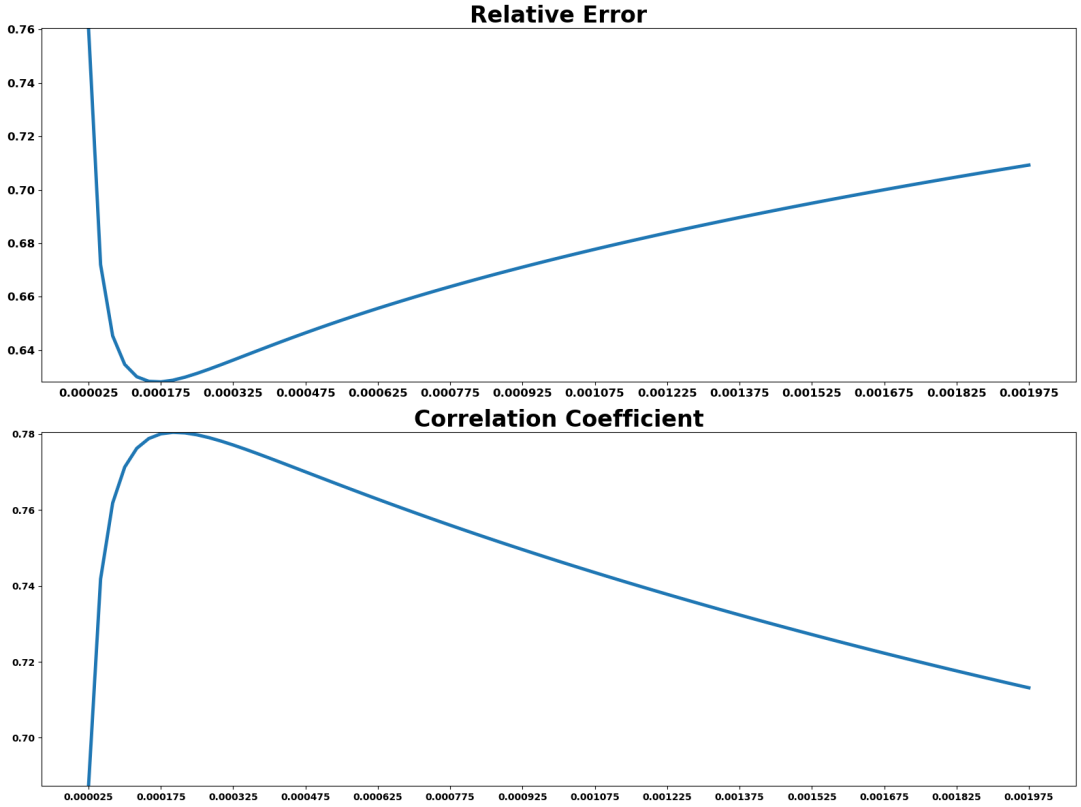

Figure 5.6: Linear sweep in a broader range of regularization parameters and post-reconstruction metrics for the whole training dataset. The mean values of RE and CC are plotted.

5.2.4 Convolutional Neural Network

As mentioned before, the denoising step Eqn. (5.3b) is to be performed by a neural network, in particular, a CNN. In this section, the model architecture and the training configuration is going be presented.

5.2.4.1 Model architecture

The utilized base design for the neural network is also inspired from UNet with the following modifications:

- A residual skip connection is added between input and output.
- A residual skip connection is added to the convolutional blocks utilized in the same level encoder-decoder blocks.
- The number of convolutional kernels (output channel parameter in PyTorch) is not specified as increasing powers of two, instead used custom and manually set channel numbers.

The CNN model and the regularization parameter of the data-fidelity block are optimized by the Adam optimizer with learning rates 10^{-4} and 10^{-8} respectively. The learning rate (LR) of the regularization parameter is intentionally set to provide slow update to avoid the sensitivity of the solution to the regularization parameter. The model parameters are updated after every batch of data is forward-fed to the network, whereas the update period for the regularization parameter is one per every epoch. This approach also guarantees that the sensitive parameter does not get updated with just one batch of data, which may deviate the solution for other batches further. Instead, the gradient is accumulated and the mean of the total gradient to every batch is applied to the regularization parameter.

The first training experiment setup is as follows:

- LR_{model}: 10^{-4}
- $\text{LR}_{\text{Reg. param}}$: 10^{-8}

- Optimizer: Adam
- Loss: Mean squared error
- Batch size: 64
- Scheduler Patience: 50
- Scheduler Factor: 0.2
- Scheduler monitor: Validation loss

5.2.4.2 Neural Network Architecture

The general architecture of the UNet model is given in Figure 5.7. Following that, the layer-wise components of the main blocks of the UNet are given in Figure 5.8. The convolutional block of the network has two convolutions, two batch normalization layers following the convolutions, ReLU activations and a subsequent dropout layer after the first nonlinearity. Furthermore, there is a skip connection that concatenates the input of the convolutional block and the first set of features coming from the dropout layer. The encoder block is composed of one convolutional block whose output is connected to the same level decoder block and the max pooling layer. The decoder block, on the other hand, utilizes a 1D transpose convolution with kernel size and stride equal to 2, resulting in a sequence upsampled by 2. After the transpose convolution, the output depthwise concatenated to the features coming from the same-level encoder via skip connection and there is a convolutional block that halves the number of channels in the concatenation.

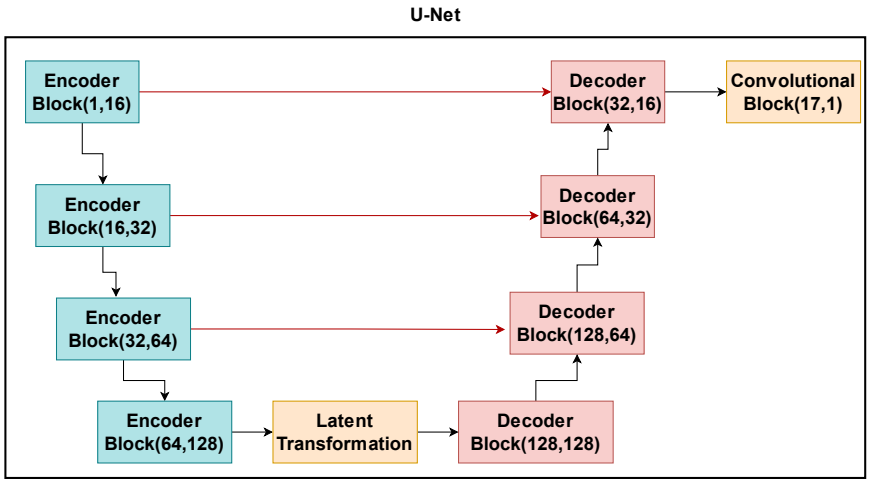

Figure 5.7: The general architecture of the proposed UNet.

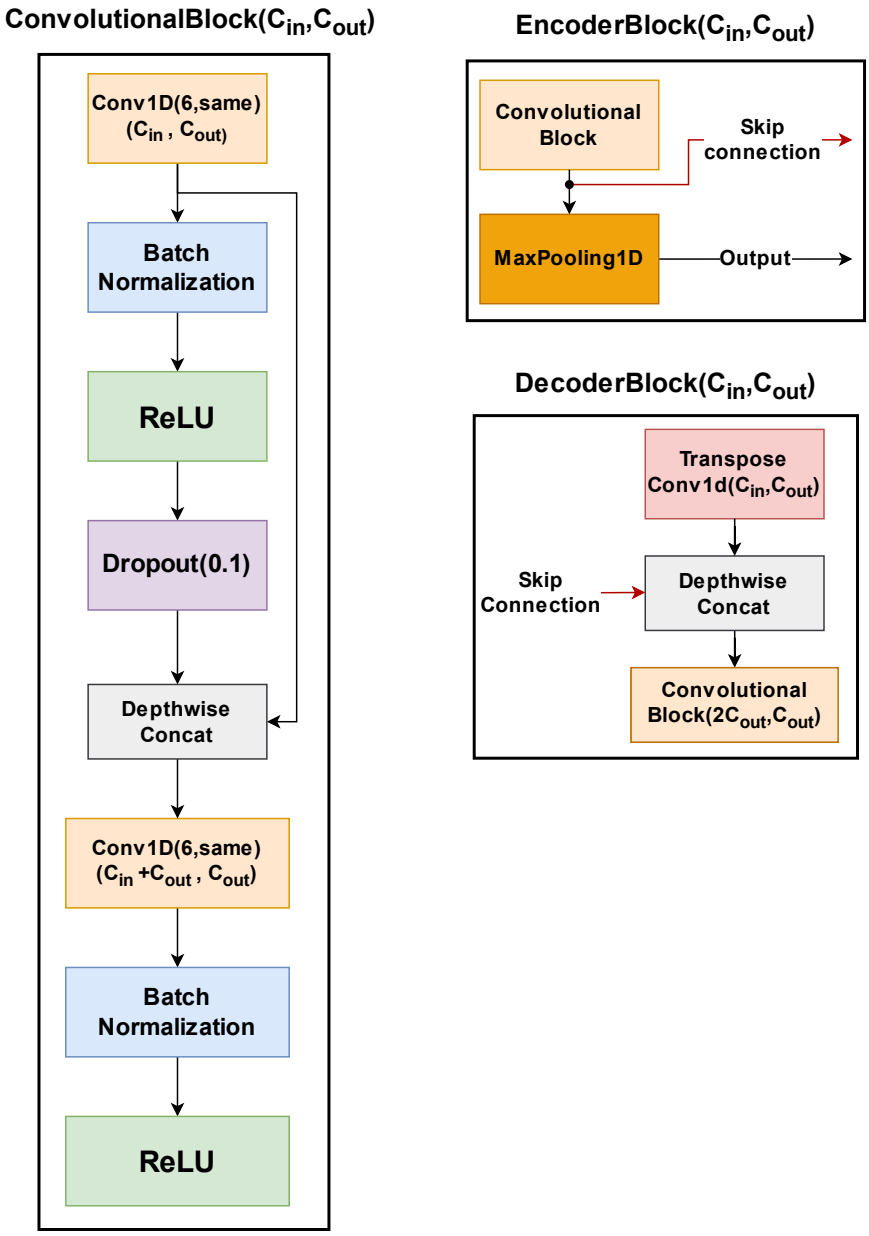

Figure 5.8: Layer-wise components of the U-Net architecture.

There are 4 encoder and 4 decoder blocks utilized in the proposed network. There is a convolutional block at the end of the tensor flow to transform the output of the decoder so that the output has only one channel, just like the input. Between the level-4 encoder and decoder a transformation block is used to apply a transformation on the encoded features in the latent space.

There are three model architectures proposed for the denoiser neural network. Differ-

ent layers for transformation blocks are utilized. For the transformation block, first a **ConvolutionalBlock(128,128)** is utilized. This network only utilized the spatial features of the signals to learn the prior. To learn a spatio-temporal prior **LSTM-Block** is used in the latent transformation. In addition to these, another scenario is implemented with Long-Short-Term Memory (LSTM) units. In addition to the **ConvolutionalBlock(128,128)** as the latent transformation, two LSTM layers are utilized at the input and the output layers of the UNet. This scheme provides the configuration for the network to learn the temporal prior directly at the signal space, rather than the latent space.

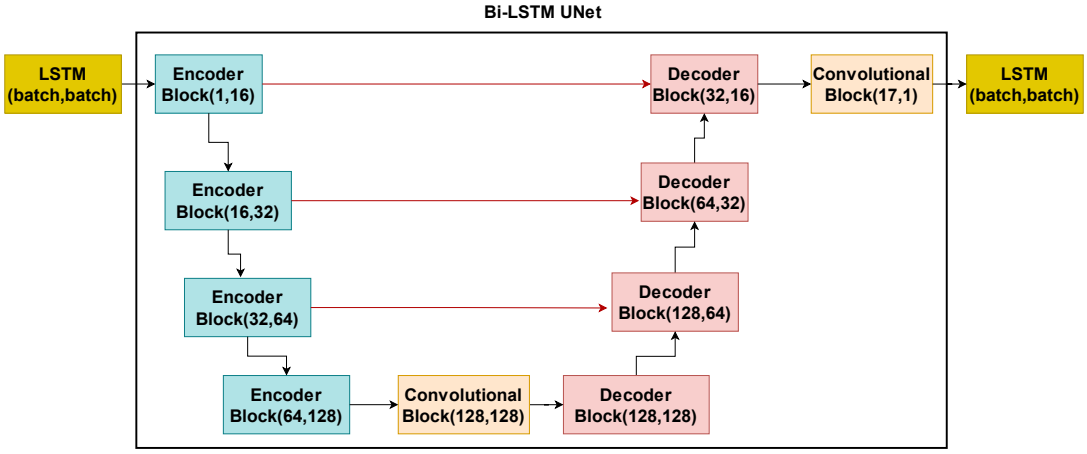

Figure 5.9: The Bi-LSTM UNet architecture.

5.2.4.3 Data Preparation

The epicardial and thorax data simulations are conducted as explained in Chapter 3. The data from experiments have shape $[N \times t_i]$ where t_i corresponds to the number of time instances EGMs were captured for training data i and N corresponds to the number of source locations, *i.e.* vertices of the geometry, to be reconstructed on the epicardial surface. Due to the variations in t_i, *i.e.*, due to the fact that each data have different time lengths, there are two options for setting the input data dimension:

- **Procedure 1:** Treating time dimension as the batch dimension, so that the neural networks' layer sizes can be independent of this variation. Hence, the data is reshaped to $\big[B, 1, N\big]$ where B corresponds to the batch size or the time in-

stances and N corresponds to the number of spatial features, *i.e.* nodes. The unsqueezed second dimension is added for the proper operation of convolutional layers implemented in PyTorch [163].

- **Procedure 2:** Finding an optimum range of EGM segment and an algorithm for generating batches to deal with time-length variability, and building the network based on this pre-determined length.

Depending on the types of layers of network used to learn the implicit prior, the approach used to generate batches is determined. The networks that learn only the spatial prior can exploit the flexibility of the first procedure. The options that utilize the temporal correlation of the signals require the model to input the training data in fixed shape. Hence, a procedure to generate fixed size batches from the training data having different shapes is needed.

For **Procedure 2**, Algorithm 5 is implemented to generate batches of desired size from the training data of various length. First, a batch size is determined and is given as an input to the algorithm. The algorithm completes the data whose time dimension is smaller than this size is completed to desired batch size by cyclic concatenation. If the training data contains more number of time instances, then it is split into mini-batches of the desired batch size, starting from the first time instance. The lat incomplete batch is completed by prepending the previous time instances.

In addition, to accelerate the neural network training, the inputs are normalized into the range of $[0\ 1]$. For training data $\mathbf{X}$, this is conducted as follows:

- $\mathbf{X} \leftarrow \mathbf{X} - \min(\mathbf{X}) \rightarrow$ The input is shifted into the range $[0, \underbrace{\max(\mathbf{X}) - \min(\mathbf{X})}_{\text{Peak-to-peak amplitude}}]$
- $\mathbf{X} \leftarrow \frac{\mathbf{X}}{\text{peak-to-peak amplitude}}$

Depending on the type of the **Latent Transformation** utilized in these networks, the data is fed-forward to network differently. The transformation blocks are as follows:

- **ConvolutionalBlock(128,128):** In this case, different time instances are processed separately as different batches. The temporal dependency of the signals

Algorithm 5 Training Data Creation.

Require: A training database with N beats, **batchsize**

for Beat in the training set **do**
  $t \leftarrow$ time length of the beat
  if $t <$**batchsize then**
    Repeat the beat in the time dimension $\lceil \frac{t}{\textbf{batchsize}} \rceil$ times
    return Take the first **batchsize** time instances starting from $t = 0$
  else if $t =$**batchsize then**
    return Beat itself
  else
    Split the beat into equal pieces of size **batchsize** and save
    Generate a final overlapping sequence of length **batchsize** from the end of the beat and save
    Concatenate saved beats in another dimension
    return The concatenated tensor
  end if
end for

are not exploited in the learning process, hence only spatial prior is learned thorough this configuration. Hence, **Procedure 1** is employed in the batch generation.

- **LSTMBlock:** This scenario enables network to learn the temporal dependency between the encoded features in the latent space of the network. This requires the network layers to be initialized as the same **batchsize** used in **Procedure 2**.

The normalized inputs are fed into the neural network and the output of the networks are denormalized using the inverse process, by first amplifying by previously saved peak-to-peak amplitude and then shifted by the minimum of the input. In the inference step, same normalization and denormalization steps are applied to the test data. Depending on the type of the neural network the normalization is performed differently:

- **Spatial normalization:** In the networks that learn only the spatial prior, the

normalization is performed along the spatial dimension of the input data. Hence, this approach is utilized with **Procedure 1**.

- **Spatiotemporal normalization:** Since the spatial normalization causes signals to lose temporal correlation, due to the fact that the peak-to-peak amplitude of the spatial distribution changes over time, the spatiotemporal normalization is performed in the networks which learn the spatiotemporal prior. In this approach, the whole training batch is normalized, instead of each of the independent time instances. This normalization is applied on the batches generated via **Procedure 2**.

The train-validation split of the data is performed randomly with a fixed random seed to avoid the random performance alterations due to the random split. The train-validation ratio was set to 0.05, hence 15 test beats are used for validation and 294 beats are used for training. The batch generation (Algorithm 5) is conducted on these split datasets differently to prevent batches from the training data being in validation data.

5.2.5 Architectural Evolution and Empirical Validation Results

In this section, the form of the final proposal for the neural network architecture is validated by showing the performance of the previous models and model benchmarking.

Figure 5.10 shows a scenario that corresponds to a reasonable validation data generalization, utilizing only spatial features of the data. Results in Figure 5.11 may indicate that the spatially encoded features do not possess any correlation along the temporal axis. Hence, it might be better to learn the temporal correlation in the signal domain. On the other hand, when the temporal correlations are taken into account as described in the scenario in Figure 5.11, the temporal correlation coefficient peaked at 0.99. Exploiting both spatial correlation in neighboring reordered nodes and the consecutive time frames enabled model to fit data really well and simultaneously provided remarkable validation results. Hence, Bi-LSTM Spatial UNet, is used to perform the inference on the test data.

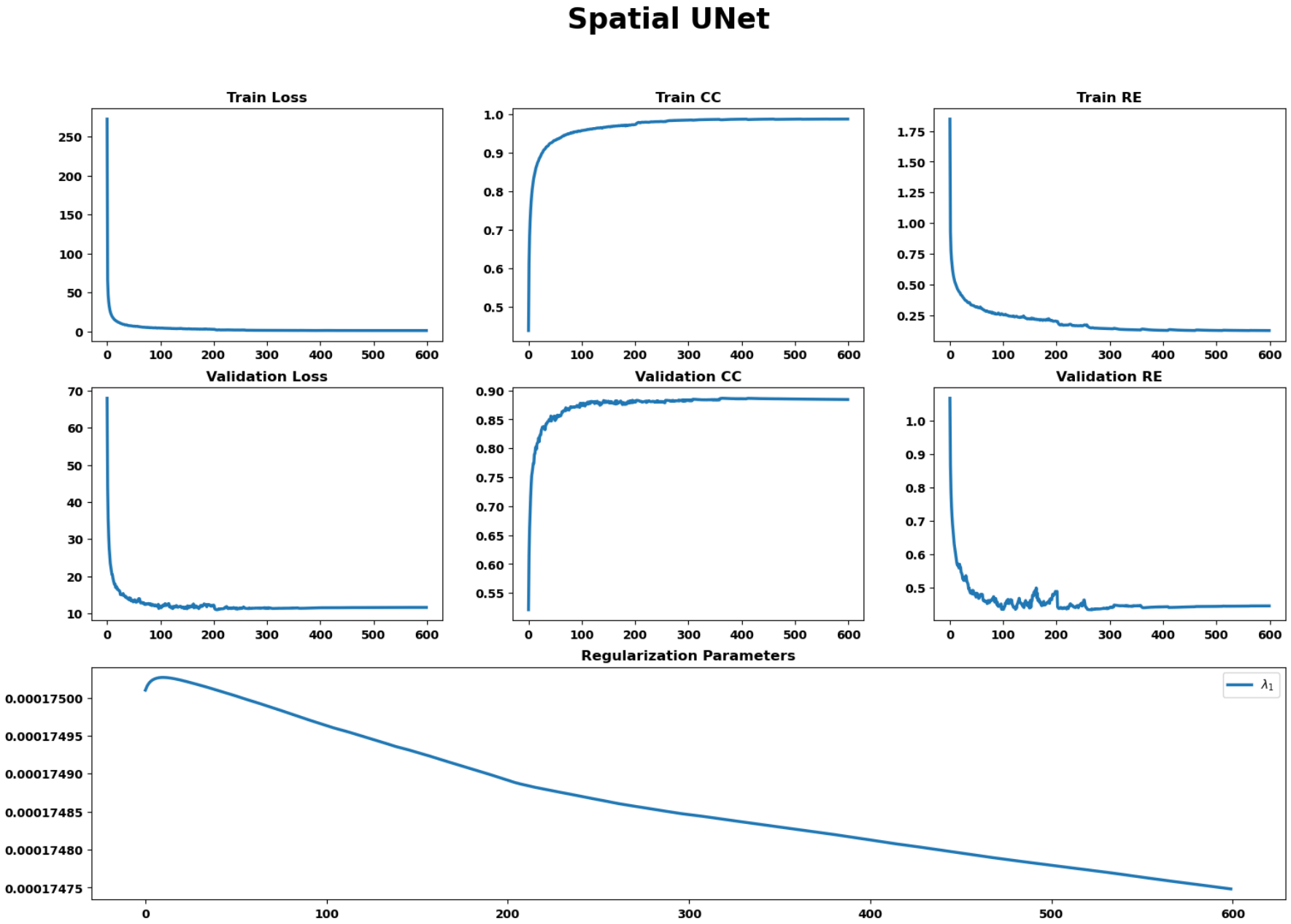

Figure 5.10: The correlation coefficient for training and validation data achieved 0.91 and 0.71. Mean relative error for training data was recorded 0.29 whereas it was 0.60 for the validation data.

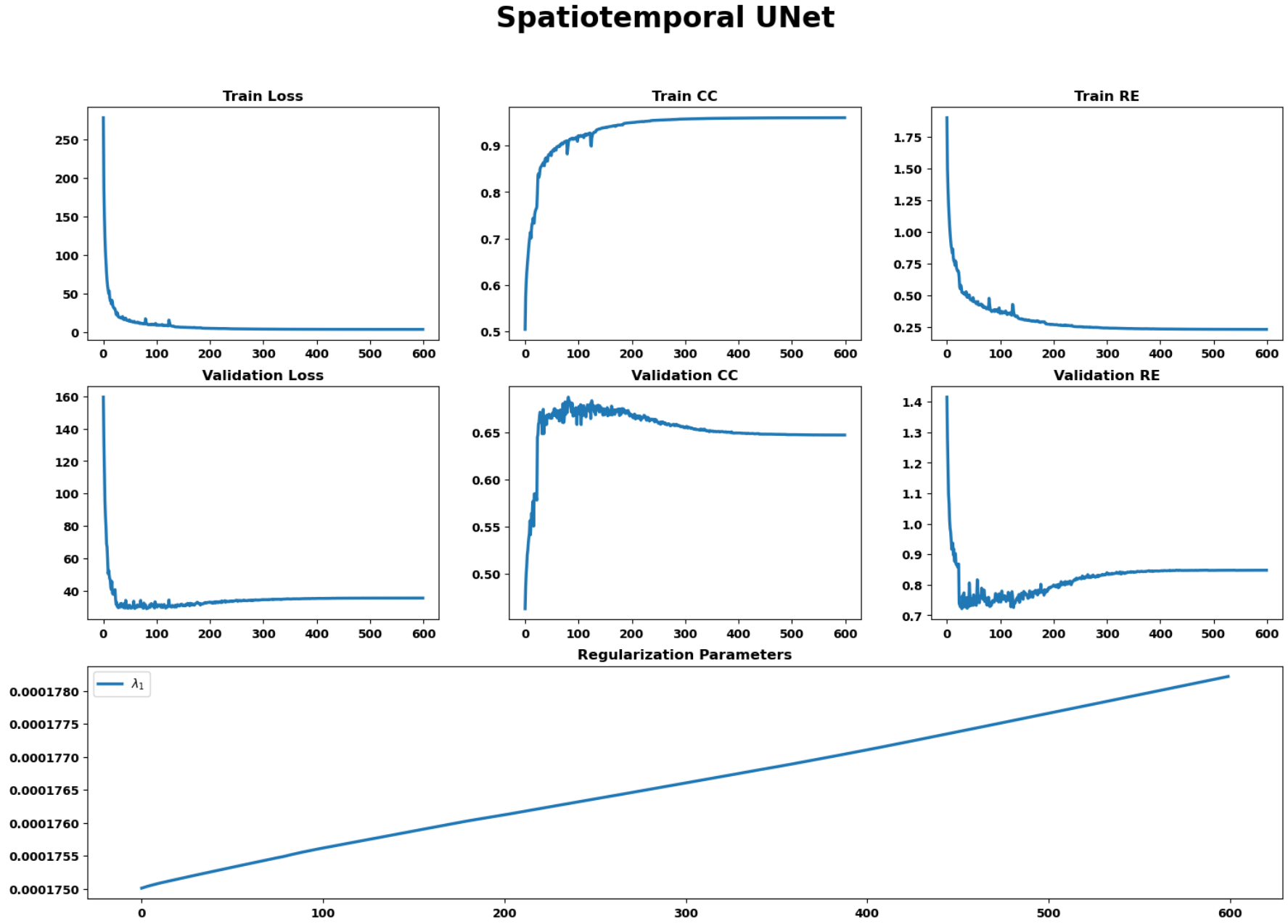

Figure 5.11: Although the model fits training data sufficiently, achieving 0.95 correlation coefficient, it had difficulties in generalizing the performance to validation data. The same observation can be made for relative errors: 0.23 and 0.84 for the last epoch.

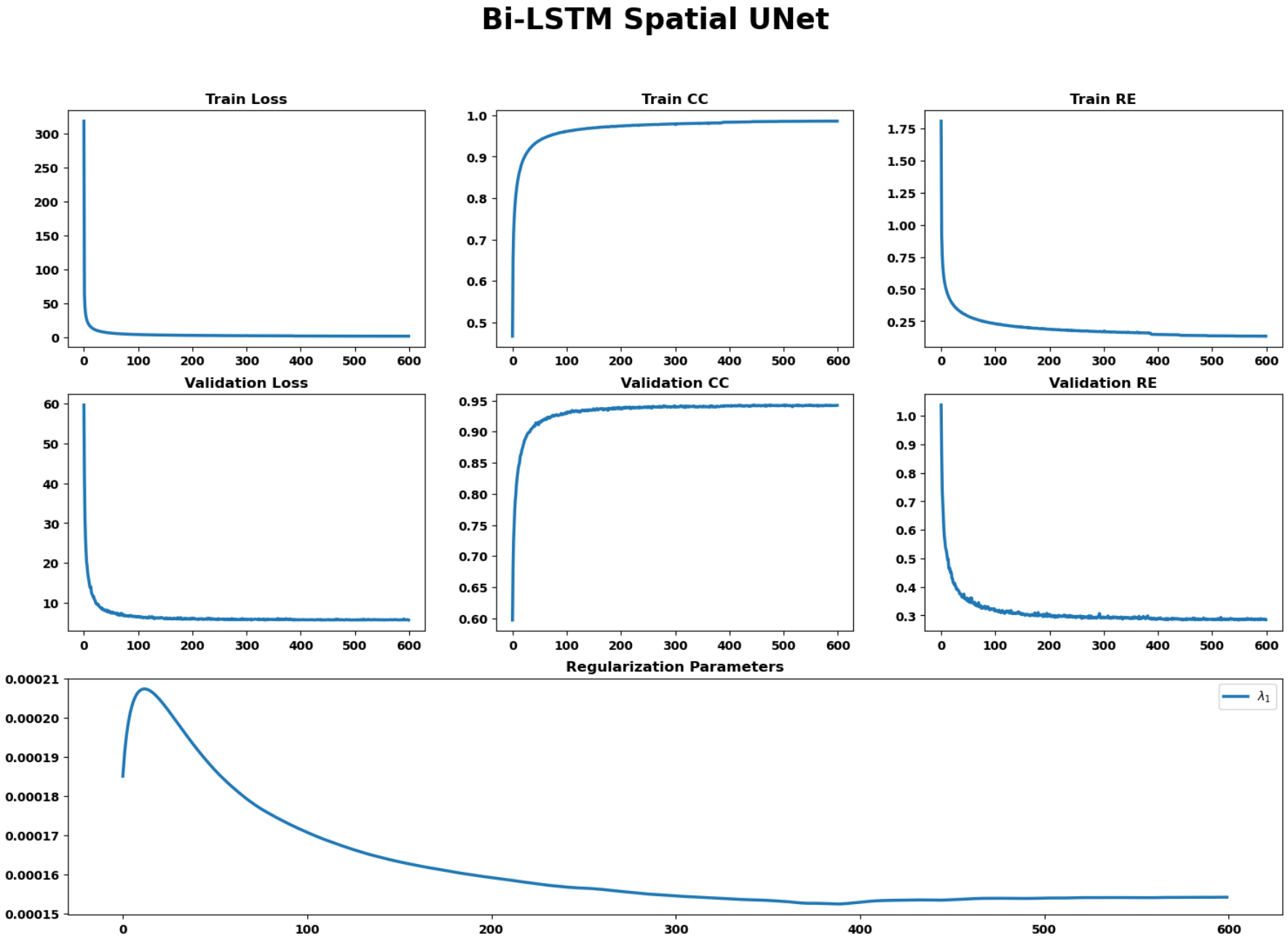

Figure 5.12: Trend of the temporal reconstruction metrics during training. The model fits training data well. Mean training and validation correlation coefficient at the last epoch is 0.99 and 0.89 respectively. The performance loss in terms of relative error is higher than the correlationwise loss.

To decide the batch size, which directly affects the model architecture, a series of experiments are run and the train and validation results are inspected.

Table 5.2: Performance of Bi-LSTM UNet with different batch size configurations.

Batch size	Train CC	Train RE	Validation CC	Validation RE	Train Loss	Validation Loss
16	0.963	0.205	0.848	0.486	3.121	13.203
32	0.965	0.202	0.912	0.349	3.410	7.698
64	0.967	0.195	0.929	0.319	3.552	6.746
128	0.945	0.257	0.888	0.397	4.116	7.807

The results clearly showed that 64 as batch size is the optimal choice to capture the temporal correlations in the training data, hence the batch size parameters of the architectures that learn spatiotemporal prior are fixed.

5.3 Predictions on Test Data

The proposed method's performance is compared with the zero-order Tikhonov regularization and Bayesian MAP estimation using the same training data for prior model estimation using 4 EGM reconstruction metrics, activation time CC and localization error. These results, in median (IQR) representation, are collected under three tables as temporal metrics in Table 5.3, spatial metrics in Table 5.4 and activation time related metrics in Table 5.5. The most performant method's result is given in **bold** font.

In all the test data, the proposed method outperformed the remaining methods. On average, NN improves the reconstructions of Tikhonov by 21.2% and MAP by 14.8% in terms of temporal RE. The temporal CC is observed to be the highest for the NN for every test beat, and it resulted in an average of approximately 0.1 improvement in the CC. The improvement is more obvious when temporal REs provided by NN and Tikhonov are compared, which is decrement by 0.16 on average.

When spatial metrics are analyzed, it is observed that the proposed method provides

more stable and consistent reconstruction throughout different time instances of the beat, greatly improving the IQR at least by 33%. This can also be observed in Figure 5.13, where spatial CC is plotted in box plots. The qualitative analysis immediately shows that the distributions provided by NN are much more compact when compared to the remaining metrics. Other distributions for three remaining metrics can be found in Section 7.3. Both the improved median and best-case temporal metrics, along with the compact distribution of spatial metrics clear shows the benefit of learning temporal prior.

Table 5.3: Temporal Metrics for Test Data using different reconstruction methods in median(IQR) representation.

Test	Temporal CC			Temporal RE		
Data	Proposed	MAP	Tikhonov	Proposed	MAP	Tikhonov
1	**0.86(0.22)**	0.76(0.21)	0.75(0.26)	**0.50(0.34)**	0.62(0.26)	0.63(0.31)
2	**0.83(0.30)**	0.73(0.39)	0.79(0.35)	**0.57(0.45)**	0.70(0.42)	0.67(0.39)
3	**0.86(0.17)**	0.73(0.24)	0.80(0.16)	**0.51(0.27)**	0.66(0.25)	0.61(0.24)
4	**0.88(0.19)**	0.84(0.18)	0.83(0.26)	**0.63(0.29)**	0.71(0.38)	0.73(0.31)
5	**0.91(0.19)**	0.85(0.25)	0.85(0.23)	**0.56(0.17)**	0.70(0.29)	0.74(0.29)
6	**0.91(0.12)**	0.83(0.18)	0.83(0.15)	**0.45(0.31)**	0.57(0.25)	0.61(0.26)
7	**0.83(0.23)**	0.72(0.29)	0.68(0.37)	**0.57(0.10)**	0.68(0.31)	0.72(0.35)
8	**0.86(0.22)**	0.75(0.29)	0.69(0.47)	**0.51(0.14)**	0.66(0.35)	0.68(0.46)
9	**0.88(0.21)**	0.75(0.27)	0.75(0.24)	**0.49(0.36)**	0.64(0.26)	0.67(0.25)
10	**0.86(0.22)**	0.74(0.33)	0.70(0.40)	**0.52(0.37)**	0.63(0.31)	0.68(0.33)
11	**0.88(0.24)**	0.76(0.32)	0.79(0.26)	**0.53(0.36)**	0.62(0.33)	0.67(0.31)
12	**0.88(0.22)**	0.80(0.33)	0.78(0.33)	**0.53(0.32)**	0.60(0.31)	0.69(0.39)
13	**0.90(0.18)**	0.82(0.20)	0.81(0.24)	**0.45(0.39)**	0.59(0.28)	0.64(0.37)
14	**0.89(0.17)**	0.81(0.32)	0.76(0.33)	**0.49(0.36)**	0.59(0.33)	0.67(0.40)
15	**0.88(0.17)**	0.80(0.20)	0.79(0.19)	**0.51(0.34)**	0.61(0.25)	0.63(0.26)
16	**0.88(0.14)**	0.77(0.15)	0.75(0.21)	**0.47(0.28)**	0.61(0.23)	0.65(0.28)
17	**0.88(0.14)**	0.81(0.14)	0.76(0.20)	**0.47(0.30)**	0.57(0.23)	0.65(0.29)
Med (IQR)	**0.88(0.02)**	0.78(0.06)	0.79(0.05)	**0.50(0.05)**	0.61(0.06)	0.66(0.05)

Table 5.4: Spatial Metrics for Test Data using Different Reconstruction Methods.

Test	Spatial CC			Spatial RE		
Data	Proposed	MAP	Tikhonov	Proposed	MAP	Tikhonov
1	**0.80(0.10)**	0.73(0.33)	0.73(0.23)	**0.60(0.13)**	0.69(0.30)	0.70(0.23)
2	**0.86(0.08)**	0.67(0.20)	0.78(0.25)	**0.51(0.13)**	0.74(0.18)	0.63(0.26)
3	**0.86(0.12)**	0.69(0.30)	0.77(0.26)	**0.53(0.18)**	0.75(0.24)	0.69(0.30)
4	**0.79(0.18)**	0.69(0.41)	0.68(0.38)	**0.64(0.28)**	0.71(0.38)	0.73(0.31)
5	**0.83(0.11)**	0.75(0.27)	0.69(0.34)	**0.56(0.17)**	0.70(0.29)	0.74(0.29)
6	**0.87(0.16)**	0.76(0.33)	0.78(0.34)	**0.50(0.23)**	0.64(0.31)	0.64(0.33)
7	**0.82(0.13)**	0.70(0.31)	0.63(0.35)	**0.55(0.10)**	0.67(0.16)	0.71(0.20)
8	**0.85(0.13)**	0.71(0.28)	0.70(0.23)	**0.52(0.14)**	0.67(0.20)	0.68(0.13)
9	**0.87(0.11)**	0.69(0.30)	0.57(0.41)	**0.51(0.17)**	0.74(0.24)	0.76(0.29)
10	**0.78(0.22)**	0.66(0.27)	0.57(0.39)	**0.58(0.28)**	0.72(0.27)	0.76(0.32)
11	**0.80(0.22)**	0.69(0.33)	0.66(0.38)	**0.59(0.22)**	0.73(0.28)	0.76(0.27)
12	**0.79(0.26)**	0.70(0.52)	0.68(0.59)	**0.62(0.29)**	0.72(0.36)	0.75(0.35)
13	**0.87(0.15)**	0.81(0.31)	0.79(0.20)	**0.49(0.21)**	0.60(0.32)	0.62(0.19)
14	**0.84(0.11)**	0.80(0.64)	0.77(0.39)	**0.53(0.23)**	0.59(0.43)	0.65(0.29)
15	**0.85(0.03)**	0.75(0.20)	0.78(0.15)	**0.53(0.07)**	0.68(0.20)	0.63(0.16)
16	**0.88(0.06)**	0.78(0.25)	0.73(0.23)	**0.47(0.15)**	0.64(0.28)	0.66(0.25)
17	**0.87(0.08)**	0.82(0.23)	0.74(0.18)	**0.50(0.18)**	0.59(0.28)	0.64(0.21)
Med (IQR)	**0.85(0.05)**	0.70(0.08)	0.71(0.10)	**0.53(0.06)**	0.69(0.09)	0.68(0.10)

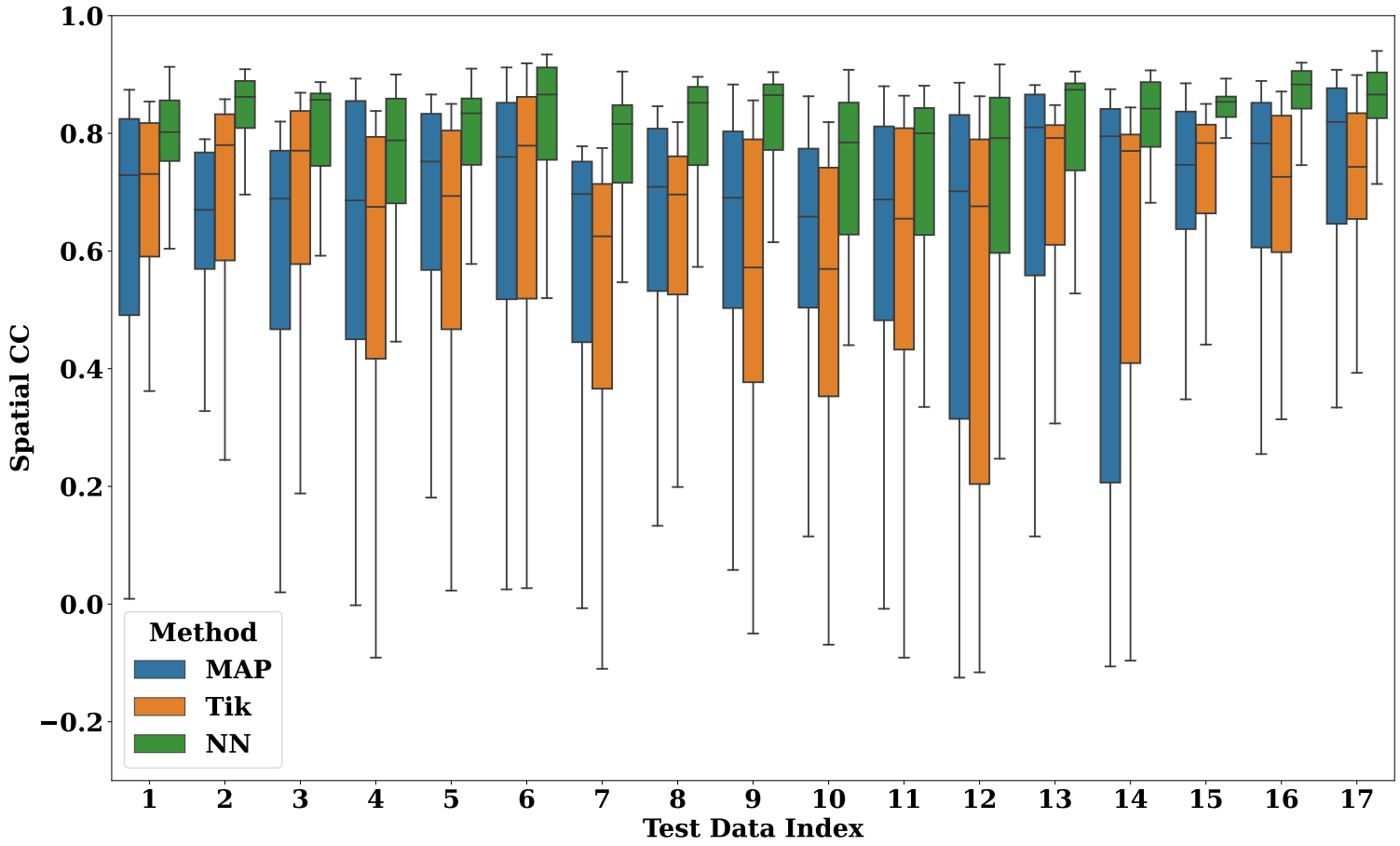

Figure 5.13: Comparison of spatial CC metrics. The proposed method is abbreviated as “NN”. Apart from both the upper boundary of IQR and the best reconstruction is higher than the other methods, it can be clearly observed that the spatial metrics has more compact distribution in NN approach. This indicates that the spatial maps matches are much consistent throughout the beat due to the utilization of the temporal prior.

Table 5.5: ATCC and Localization Error for Test Data using Different Reconstruction Methods.

Test	AT CC			Localization Error		
Data	Proposed	MAP	Tikhonov	Proposed	MAP	Tikhonov
1	**0.99**	0.97	0.96	26.93	**17.31**	**17.31**
2	**0.98**	0.94	**0.98**	**5.36**	10.64	15.30
3	**0.98**	0.94	**0.98**	22.61	**18.62**	23.62
4	0.89	**0.95**	0.92	**5.15**	7.33	8.55
5	0.83	**0.94**	0.91	10.58	11.84	**7.74**
6	**1.00**	0.97	0.98	**5.06**	20.22	14.70
7	**0.99**	0.91	0.84	**0.00**	12.31	12.31
8	**0.92**	0.73	0.80	26.19	**24.36**	**24.36**
9	**0.97**	0.95	0.89	**5.11**	20.65	29.52
10	**0.98**	0.91	0.62	**5.81**	21.23	30.39
11	**0.97**	**0.97**	0.94	**8.52**	21.18	26.87
12	**0.98**	**0.98**	0.97	**12.41**	13.80	12.26
13	**0.99**	0.98	**0.99**	**4.84**	5.02	7.42
14	**0.99**	0.98	**0.99**	**0.00**	8.53	5.31
15	0.96	**0.97**	0.94	**4.53**	7.98	5.46
16	**0.99**	0.96	0.94	**21.96**	35.54	33.77
17	**0.94**	**0.94**	0.92	**13.62**	28.41	14.57
Med (IQR)	**0.98(0.02)**	0.95(0.03)	0.94(0.07)	**5.8(8.6)**	17.0(10.5)	14.7(16.6)

The activation time computation, as a post-processing step, is realized to compare the performance of the proposed method to the classical methods. On average, NN method outperformed MAP by 3% and Tikhonov by 4% in terms of activation time CC. The approach again provided the more compact CC distribution on average. Furthermore, it significantly outperformed the classical methods at localizing the pacing site of the test beats. The proposed approach yielded a reduction in error by a factor of one third compared to the alternative methods, showcasing its superior performance and efficacy. In test data 4 and 5, the NN reconstructions resulted in less localization error, although the activation time correlation was lower. From this, one can deduce that the proposed method can reconstruct the epicardial signals better at the earlier activated stages. Although the correlation is lower due to the errors in the reconstruction of later activated time instances, the signals at the nodes that have smaller activation time is reconstructed better. This fact can be observed in Figure 5.14. The regions where the activation time maps show smaller values is earlier activated regions. In these points, the proposed approach produced a wider region of red values, which implies the lower RE and successful temporal reconstructions.

From the proximity of the pacing site, NN produced lower RE maps compared to the remaining classical methods. Hence, this figure justifies the "inconsistency" between the activation time CC and LE. The corresponding EGM reconstruction is illustrated in Figure 5.15.

In Figure 5.15, the initial observation is that all the methods caused time latency with respect to the ground truth in the reconstruction process. Another observation is the fluctuating EGMs in the Tikhonov solution. This is actually caused by the temporally-independently corrupted test data. Due to the direct matrix multiplication for the inverse computation which does not enforce any temporal constraint, Tikhonov and MAP solution generated EGM solutions that have zigzag patterns. Due to the Bi-LSTM structure in the proposed method, the temporal prior is learned and successfully used for denoising, producing smoother EGMs along the time dimension.

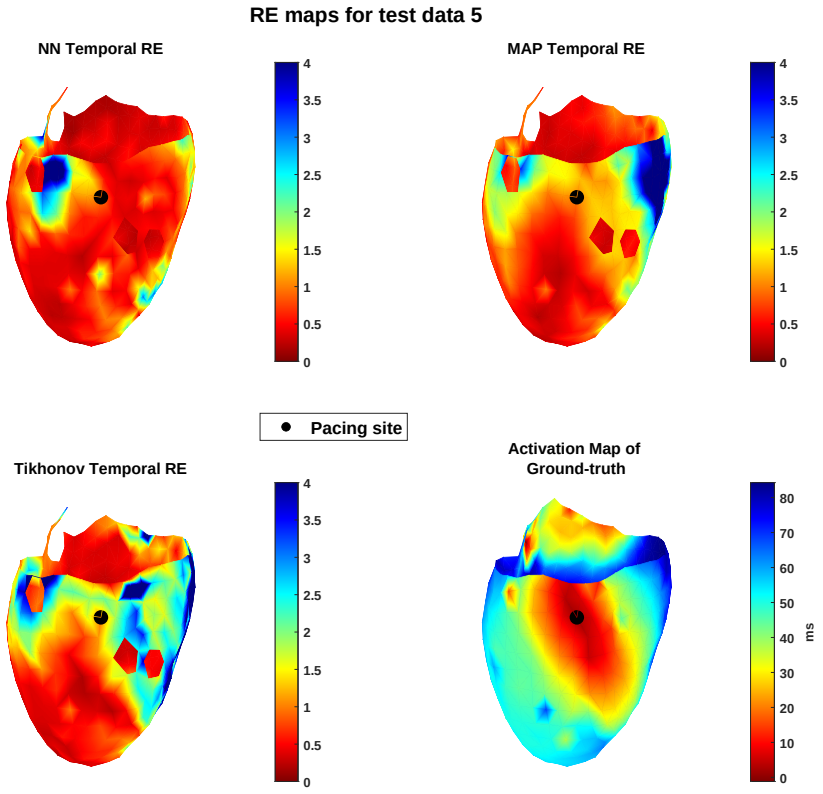

Figure 5.14: The temporal relative error maps given by 3 different reconstruction techniques and the corresponding activation map computed from the test signal. The earlier activated regions (shown by red in the bottom right figure) are shown in red for a wider region in NN method (top left).

5.4 Discussion

In this chapter, a method is proposed to augment the physics based model with the learned prior. The approach, in terms of both EGM reconstruction metrics and AT metrics, outperformed the zero-order Tikhonov and the Bayesian MAP approach using the same training data. This result can be attributed to the level of complexity of the constraint each approach imposes on the solution. The Tikhonov regularization confines the solution space to signals having small energy, whereas MAP estimation models the prior distribution of the epicardial potentials as Gaussian and outputs the solution that maximizes the posterior pdf, *i.e.*, finds the most likely solution given the

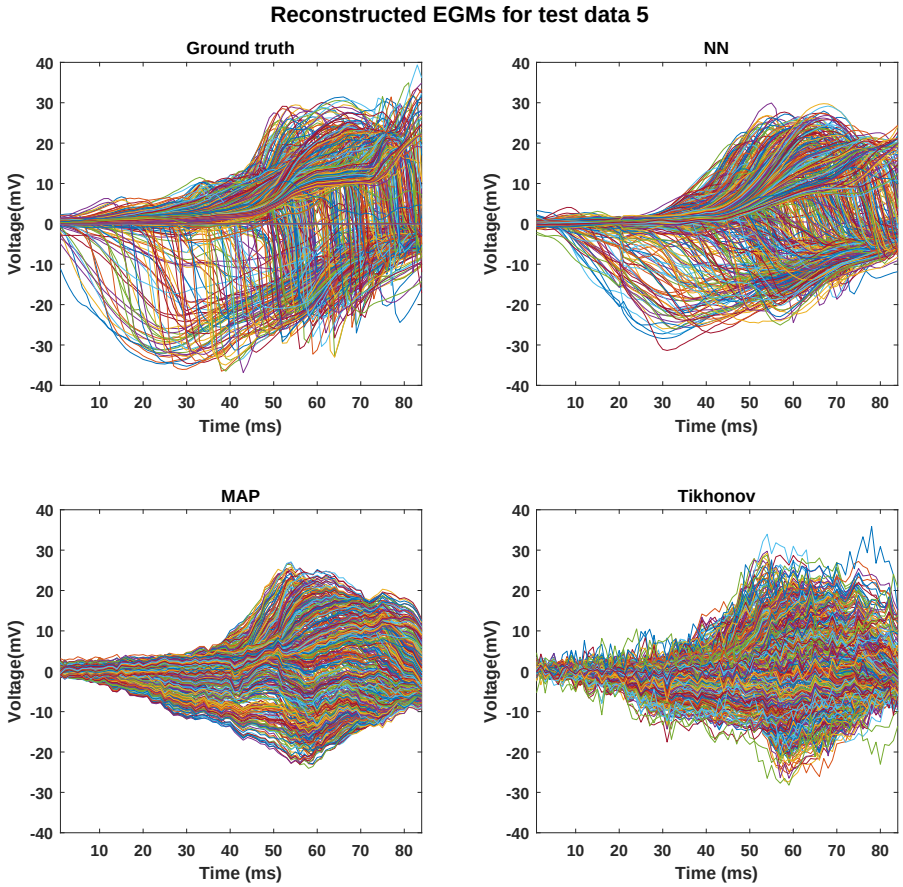

Figure 5.15: EGM reconstructions by different approaches and test data 5.

measurements. The proposed method starts with a zero-order Tikhonov estimate, and estimate another solution in the proximity of this solution. Following that, the CNN is applied as a proximal operator that corresponds to the learned spatio-temporal prior of the epicardial signals. Although there is a drop in the test performance with respect to the training data performance as usual, the experiments showed that the model was able to generalize to priors from other experiments.

5.4.1 Limitations and Future work

In this study, both the training data and test data are corrupted with 20dB SNR noise. Hence, the model's sensitivity to noise in training and inference phases are not inspected. Furthermore, the measurements are simulated with an inhomogeneous for-

ward model and the inverse solution is performed with a homogenous forward model. In all these experiments, a single forward model is used. The model's effect on $\mathbf{x_1}$ in Figure 5.3, which is denoised by the CNN to produce the final estimation, can be expressed as follows:

$$\mathbf{x_1} = \left(\mathbf{A^T A} + \lambda \mathbf{I}\right)^{-1} \left(\mathbf{I} + \lambda (\mathbf{A^T A} + \lambda \mathbf{I})^{-1}\right) \mathbf{A^T y} \tag{5.7}$$

$$= \left((\mathbf{A^T A} + \lambda \mathbf{I})^{-1} + \lambda (\mathbf{A^T A} + \lambda \mathbf{I})^{-2}\right) \mathbf{A^T y} \tag{5.8}$$

$$= {\mathbf{A}_\lambda}^\dagger \mathbf{y} \tag{5.9}$$

This is why the model learned to denoise a colored noise (which is amplified by the pseudo-inverse matrix that corresponds to the equation Eqn. (5.4)), unlike what the formulation in Eqn. (5.1) implies (a white Gaussian). Due to the $\mathcal{L}_2$-norm data-fidelity term, the denoiser was supposed to be denoise an i.i.d Gaussian noise. If we were to increase the number of iterations, the CNN can be claimed to converge to a state that performs this task. However, since the optimization is unrolled for only one iteration, the noise removed by the CNN depends on the forward matrix $\mathbf{A}$. The sensitivity of the method to the forward model should be quantified by future studies.

CHAPTER 6

CONCLUSION

This thesis has presented two studies that aim to improve the solution methods to the inverse problem of ECG, where intelligent ways of training data assessment and improvement of the accuracy and performance of ECGI by blending data-driven techniques with solid physics-based models are explored. The efforts of this exploration is divided into two distinct studies, each shedding light on a different facet of ECGI.

6.1 Evidence and Covariance-based Training Data Selection

In the first study, we focused on the pivotal role of training data in shaping the effectiveness of ECGI. Depending on the formulation, the training data is used to estimate the prior model parameters, estimate the state transition matrix of the Kalman filter and the initial estimate for the state vectors and for learning the prior distribution or conditional distribution of the data [96, 137, 141].

Previous studies in the field of ECGI adapted different ways of utilizing the training data which can be summarized as follows:

- The whole available data is utilized without any selection, especially in limited data scenarios such as training the neural networks [137].
- Believing that the priors that match the estimated solution more are more successful in the reconstruction, the training data to estimate the prior is sampled from the proximity of the estimated pacing location of the solution by using Euclidean distance or the neighborhood distance [105, 106].

In this study, the training data's representation capability of the prior distribution was assessed in the Bayesian MAP estimation setting. Introducing the evidence approach and the covariance approach, we aimed to fine-tune how training data is used. The evidence approach demonstrated its flexibility by creating custom training data for each scenario, highlighting its adaptability. The covariance approach, on the other hand, tapped into the patterns hidden in data's cross-correlations, essentially refining how we estimate spatial variance. We found that, the covariance approach was able to achieve a statistically similar performance by utilizing only one fourth of the training data by estimating the spatial covariance as unbiased as possible within the available training database. Considering that the variance imbalance results from different stimulation locations, our results match the previous results stating that the wider pacing location coverage on the epicardial surface while forming the training data resulted in better performance. Our method proposed a systematic way of achieving this. In conclusion, these methods offer a roadmap for making the most of training data, helping ECGI researchers determine the sufficiency of representation of training data for accurate ECGI.

6.2 Physics-based AI-assisted Imaging

The second study took the initial step to redefine model-based ECGI by blending the best of physics-based models with data-driven learning. By merging the classic Tikhonov regularization with modern Convolutional Neural Networks (CNNs), a reconstruction method is proposed with careful organization of data that is defined on an irregular grid, that outperformed traditional approaches. By learning the indicator function in both spatial and temporal directions, the method provided a better regularization than the classical methods that only used the spatial correlations to represent the prior. This resulted in improved temporal metrics and more consistent spatial performance throughout the test beat's time instances, which is implied by the more compact distribution of the spatial reconstruction metrics. These results also verified the neural networks are generalizable to different prior distributions under one forward model if the training data has sufficient diversity.

This approach differs from the latest efforts to incorporate neural networks in the field

of ECGI in these aspects:

- Most of the studies used end-to-end training approaches that requires neural networks to learn both the reconstruction process and the prior [137, 138]. Our approach utilized the BEM generated forward model and a neural network to split the whole reconstruction process to analytical and proximal operators. Hence, neural networks are just used for learning the prior space where the epicardial signals lie.

- The data is directly used in the form it is measured. Unlike [140], there was no pre-processing in the data to transform the domain of the signals to a regular grid. Likewise, there are attempts to define the geometries as graphs and learn the spatiotemporal prior in the graph domain [141]. This method requires some custom graph convolutional operations, which are more computationally expensive and the physics-based relationship is learned in this scheme. Instead, we compute the physics-based operator from the geometry information we already have in a less-costly way and use this forward operator directly in the reconstruction with regular neural network layers. Since, the physics-based operator is computed, the number of required parameters in the neural network to learn the prior is less than the approach utilizing graphs. Although this approach is mainly proposed to improve the patient generalization, the networks are again fine-tuned with different patient data before the inference [143].

- Lastly, measured epicardial potentials and simulated torso potentials are utilized in this study. Most of the studies that utilize large amount of training data use generated (synthetic) training data to train their networks. In the method proposed in this thesis, the neural network was able to perform as a proximal operator that corresponds to the prior of measured signals requiring no need for preprocessing.

As future extensions of this initial work, the method's sensitivity to noise and forward model should be quantitatively assessed. In this configuration, the methodology only allows the generalization of geometric error, such as rotated, shifted or slightly scaled version of the same geometry. Using plug-and-play reconstruction scheme, the

study should be improved to determine the generalizability of the trained network to different forward models.

6.3 Conclusion

The possible approaches to improve the solution to the inverse problem of ECG are proposed and discussed in this thesis study. The take-off message from the thesis was it is possible to achieve

- the same performance by utilizing a small portion of training data intelligently.
- higher performance by using intelligent methods to learn the prior distributions of the epicardial potentials from the data using the building-blocks that is appropriate for the nature of the epicardial potentials.

The works presented here are initial studies that are going to need the proof of generalization to other configurations in the inverse problem. Nevertheless, these preliminary findings lay the foundation for broader generalizations across various scenarios in the realm of the inverse problem of ECGI.

CHAPTER 7

APPENDIX

7.1 Bayesian MAP solution

This section is left for the derivation of Bayesian MAP solution with Gaussian prior and independent identically distributed Gaussian noise that is uncorrelated with the measurements.

$$p(\mathbf{x}) = \frac{1}{(2\pi)^{\frac{N}{2}}|\mathbf{C_x}|^{\frac{1}{2}}} e^{-\frac{1}{2}(\mathbf{x}-\bar{\mathbf{x}})\mathbf{C_x}^{-1}(\mathbf{x}-\bar{\mathbf{x}})^T} \tag{7.1}$$

$$p(\mathbf{n}) = \frac{1}{(2\pi)^{\frac{M}{2}}|\sigma_\mathbf{n}^2\mathbf{I}|^{\frac{1}{2}}} e^{-\frac{1}{2}(\mathbf{n})\sigma_\mathbf{n}^2\mathbf{I}(\mathbf{n})^T} \tag{7.2}$$

$$\tag{7.3}$$

The covariance of $\mathbf{y}$ can be obtained as follows:

$$\mathbf{C_y} = \mathbb{E}\big[(\mathbf{y}-\bar{\mathbf{y}})(\mathbf{y}-\bar{\mathbf{y}})^T\big] \tag{7.4}$$

$$\bar{\mathbf{y}} = \mathbf{A}\bar{\mathbf{x}} \implies (\mathbf{y}-\bar{\mathbf{y}}) = \mathbf{A}\underbrace{(\mathbf{x}-\bar{\mathbf{x}})}_{\mathbf{x}_0} + \mathbf{n} \tag{7.5}$$

$$\mathbf{C_y} = \mathbb{E}\big[(\mathbf{A}\mathbf{x}_0+\mathbf{n})(\mathbf{A}\mathbf{x}_0+\mathbf{n})^T\big] \tag{7.6}$$

$$\mathbf{C_y} = \mathbb{E}\big[\mathbf{A}\mathbf{x}_0\mathbf{x}_0^T\mathbf{A}^T\big] + \mathbb{E}\big[\mathbf{n}\mathbf{n}^T\big] + \underbrace{\mathbb{E}\big[\mathbf{A}\mathbf{x}_0\mathbf{n}^T + \mathbf{n}\mathbf{x}_0^T\mathbf{A}^T\big]}_{\substack{\text{Cancels out due to uncorrelatedness} \\ \text{and zero-mean noise}}} \tag{7.7}$$

$$\mathbf{C_y} = \mathbf{A}\mathbf{C_x}\mathbf{A}^T + \mathbf{C_n} \tag{7.8}$$

The MAP solution is the solution that maximizes the posterior probability:

$$\hat{\mathbf{x}} = \arg\max_{\mathbf{x}} \ \mathbf{p}(\mathbf{x}\backslash\mathbf{y}) \tag{7.9}$$

$$= \arg\max_{\mathbf{x}} \ \frac{\mathbf{p}(\mathbf{y}\backslash\mathbf{x})\mathbf{p}(\mathbf{x})}{\int \mathbf{p}(\mathbf{y}\backslash\mathbf{x})\mathbf{p}(\mathbf{x})d\mathbf{x}} \tag{7.10}$$

The denominator of the Eqn. (7.10) is independent of the variable $\mathbf{x}$. Using the monotonicity of the logarithm function, Eqn. (7.9) can be rewritten as follows:

$$\hat{\mathbf{x}} = \arg\max_{\mathbf{x}} \ \log(\mathbf{p}(\mathbf{x}\backslash\mathbf{y})) \tag{7.11}$$

$$\hat{\mathbf{x}} = \arg\max_{\mathbf{x}} \ \log(\mathbf{p}(\mathbf{x})) + \log(\mathbf{p}(\mathbf{y}\backslash\mathbf{x})) \tag{7.12}$$

The only remaining term that needs to be explicitly defined is the conditional pdf $\mathbf{p}(\mathbf{y}\backslash\mathbf{x})$. This expression corresponds to the distribution of $\mathbf{y}$ for a given $\mathbf{x}$. With this observation, the conditional pdf can be written as follows:

$$\mathbf{p}(\mathbf{y}\backslash\mathbf{x}) = \frac{1}{(2\pi)^{\frac{N}{2}}|\mathbf{C_n}|^{\frac{1}{2}}} e^{-\frac{1}{2}(\mathbf{y}-\mathbf{A}\mathbf{x})\mathbf{C_n}^{-1}(\mathbf{y}-\mathbf{A}\mathbf{x})^T} \tag{7.13}$$

Inserting Equations (7.1) and (7.13) into Eqn. (7.12), we end up with the following optimization expression:

$$\hat{\mathbf{x}} = \arg\max_{\mathbf{x}} \ -\frac{1}{2}(\mathbf{y}-\mathbf{A}\mathbf{x}^T)\mathbf{C_n}^{-1}(\mathbf{y}-\mathbf{A}\mathbf{x}) - \frac{1}{2}(\mathbf{x}-\bar{\mathbf{x}})\mathbf{C_x}^{-1}(\mathbf{x}-\bar{\mathbf{x}})^T \tag{7.14}$$

$$\hat{\mathbf{x}} = \arg\min_{\mathbf{x}} \ \underbrace{(\mathbf{y}-\mathbf{A}\mathbf{x}^T)\mathbf{C_n}^{-1}(\mathbf{y}-\mathbf{A}\mathbf{x}) + (\mathbf{x}-\bar{\mathbf{x}})\mathbf{C_x}^{-1}(\mathbf{x}-\bar{\mathbf{x}})^T}_{\mathbf{J}(\mathbf{x})} \tag{7.15}$$

$$\nabla_{\mathbf{x}}\mathbf{J}(\mathbf{x}) = -\mathbf{2}\mathbf{A}^{\mathbf{T}}\mathbf{C_n}^{-\mathbf{1}}\mathbf{y} + 2\mathbf{A}^{\mathbf{T}}\mathbf{C_n}^{-\mathbf{1}}\mathbf{A}\mathbf{x} + 2\mathbf{C_x}^{-\mathbf{1}}(\mathbf{x}-\bar{\mathbf{x}}) \triangleq 0 \text{ at } \mathbf{x} = \hat{\mathbf{x}} \tag{7.16}$$

The Bayesian MAP solution can be expressed in closed form as:

$$\hat{\mathbf{x}}_{\mathbf{MAP}} = \left(\mathbf{A}^{\mathbf{T}}\mathbf{C}_{\mathbf{n}}^{-\mathbf{1}}\mathbf{A} + \mathbf{C}_{\mathbf{x}}^{-\mathbf{1}}\right)^{-1}(\mathbf{A}^{\mathbf{T}}\mathbf{C}_{\mathbf{n}}^{-\mathbf{1}}\mathbf{y} + \mathbf{C}_{\mathbf{x}}^{-\mathbf{1}}\bar{\mathbf{x}}) \tag{7.17}$$

7.2 Chapter 4 Results

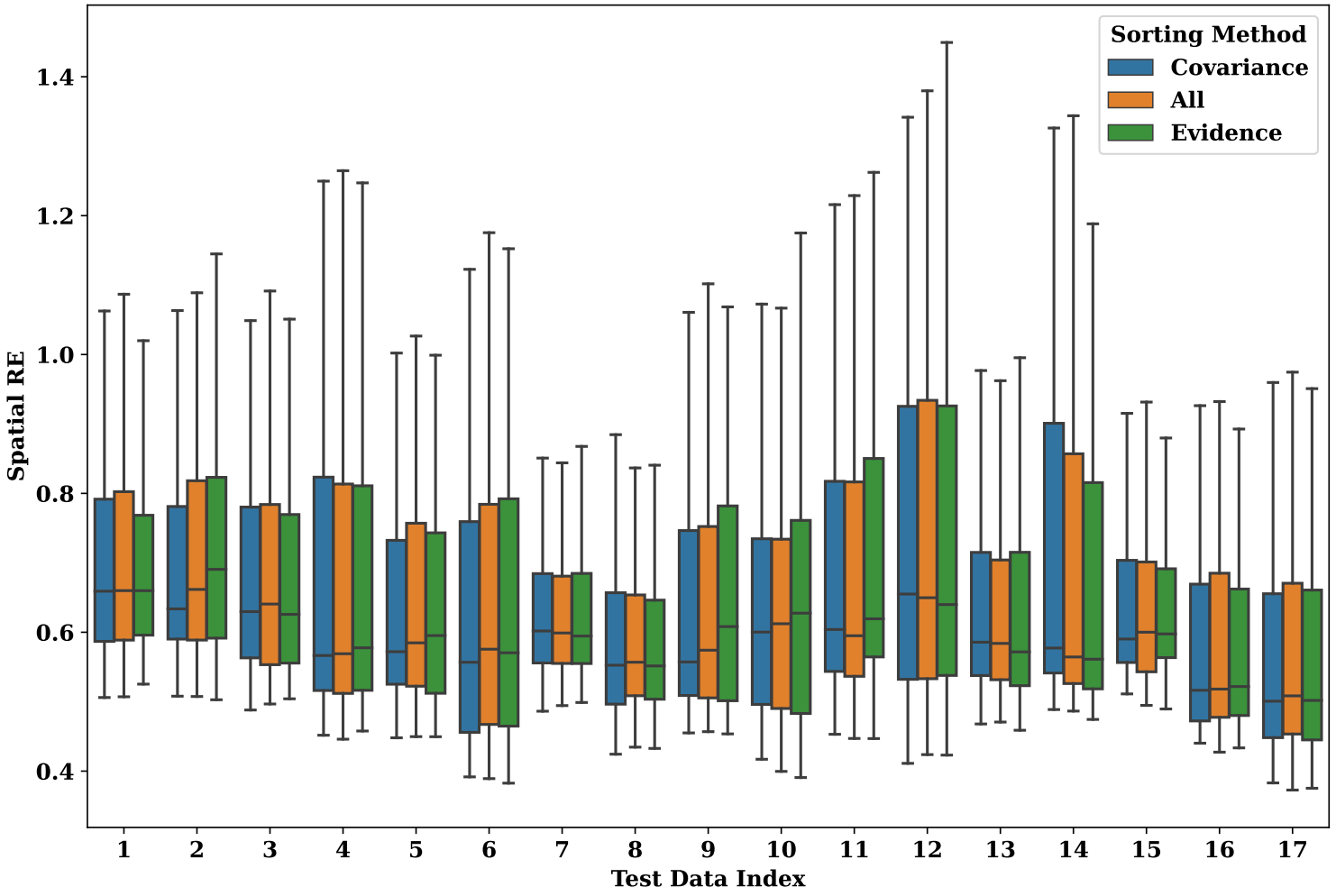

Figure 7.1: Spatial RE distributions of 17 test beats for 3 training data selection methods.

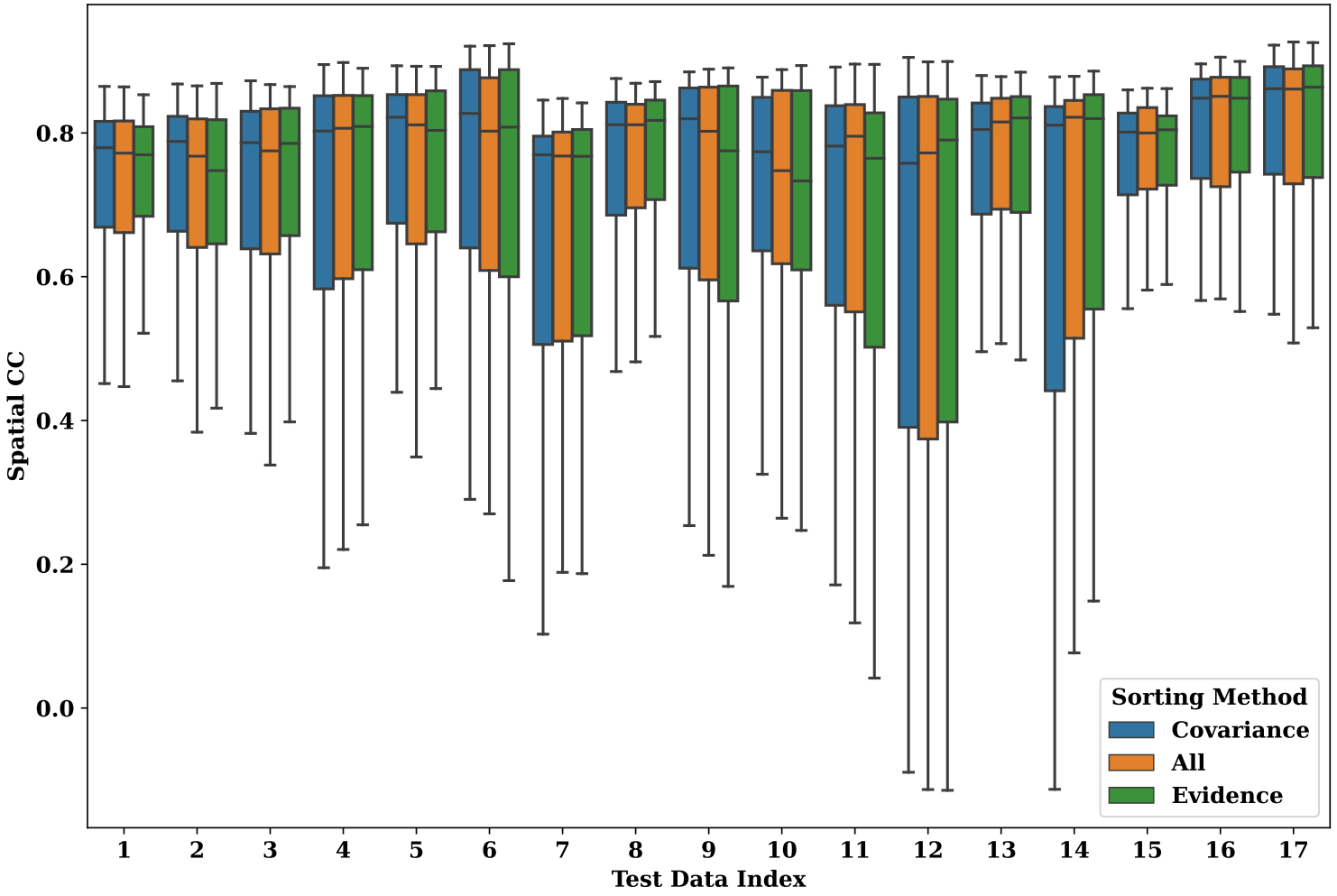

Figure 7.2: Spatial CC distributions of 17 test beats for 3 training data selection methods.

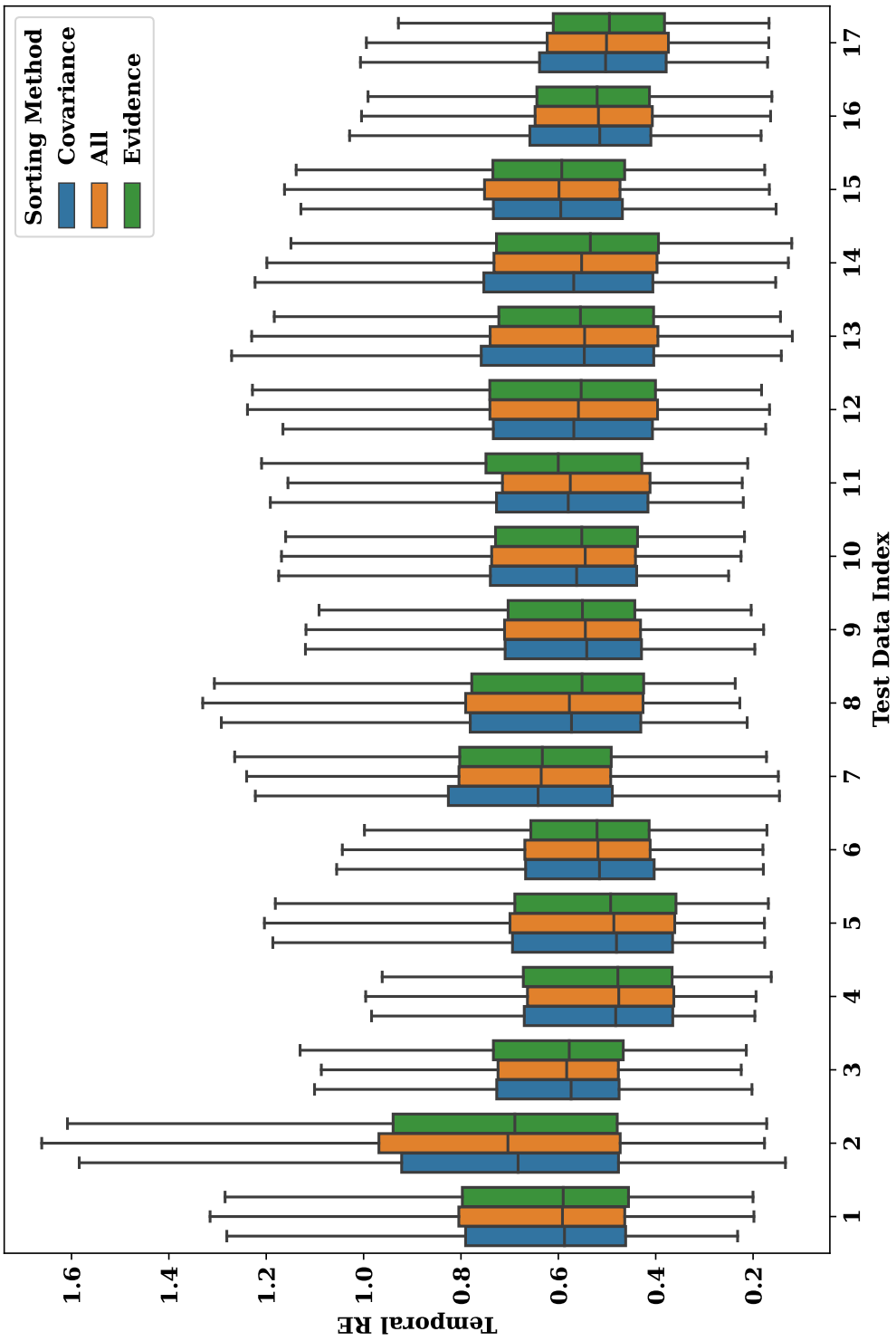

Figure 7.3: Temporal RE distributions of 17 test beats for 3 training data selection methods.

7.3 Chapter 5 Results

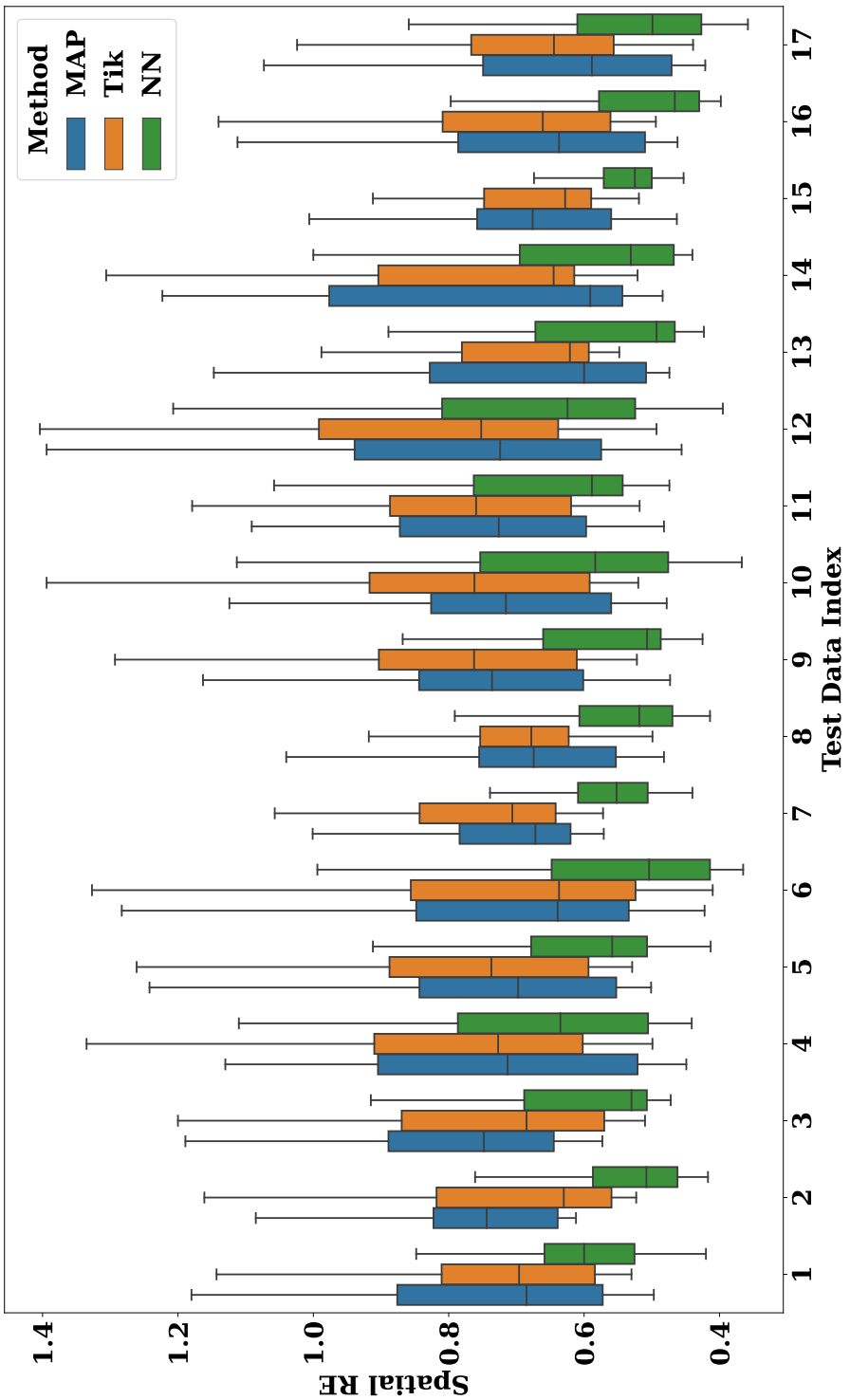

Figure 7.4: Spatial RE distributions of 17 test beats for 3 training inverse problem methods.

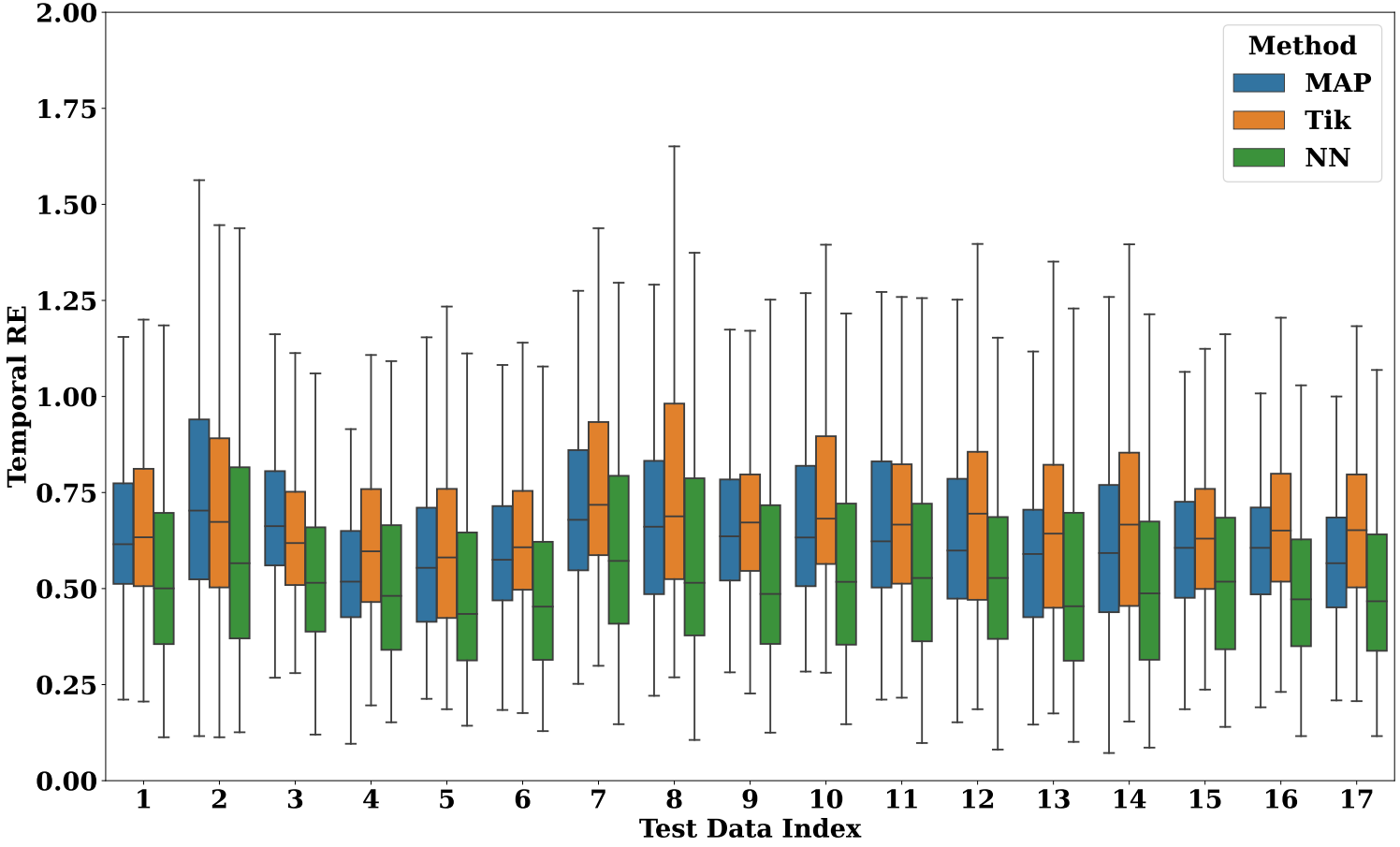

Figure 7.5: Spatial CC distributions of 17 test beats for 3 training inverse problem methods.

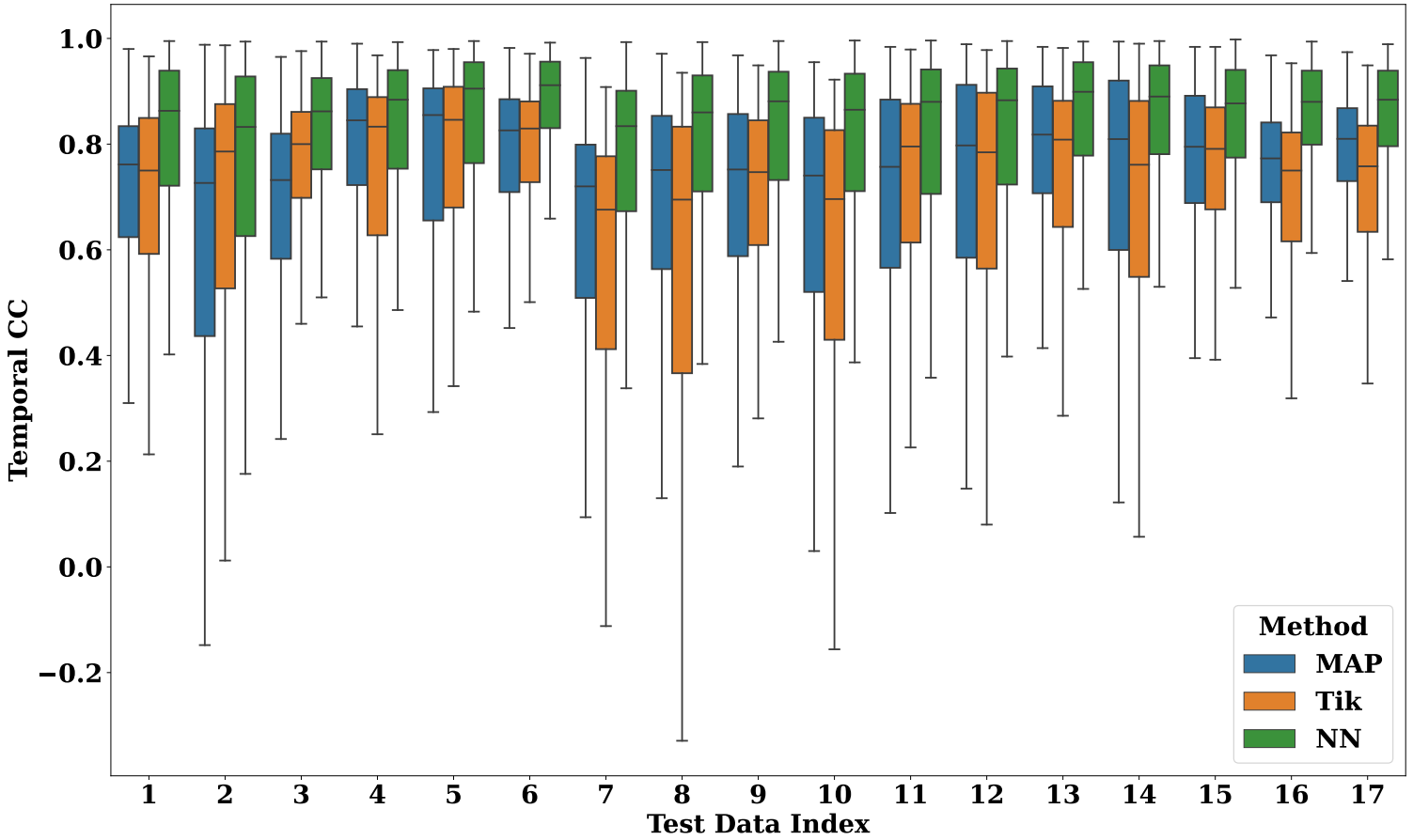

Figure 7.6: Temporal CC distributions of 17 test beats for 3 inverse problem methods.

REFERENCES

[1] A. Krishnan, H. Sharma, D. Yuan, A. F. Trollope, and L. Chilton, "The Role of Epicardial Adipose Tissue in the Development of Atrial Fibrillation, Coronary Artery Disease and Chronic Heart Failure in the Context of Obesity and Type 2 Diabetes Mellitus: A Narrative Review," *Journal of Cardiovascular Development and Disease*, vol. 9, no. 7, p. 217.

[2] Britannica, "Cross-section of the human heart." Online. [Accessed: July 14, 2023].

[3] A. O. Grant, "Cardiac Ion Channels," *Circulation: Arrhythmia and Electrophysiology*, vol. 2, no. 2, pp. 185–194.

[4] J. Malmivuo and R. Plonsey, *Bioelectromagnetism. 6. The Heart*, pp. 119–130. 01 1995.

[5] S. K. Saini and R. Gupta, "Artificial intelligence methods for analysis of electrocardiogram signals for cardiac abnormalities: State-of-the-art and future challenges," *Artificial Intelligence Review*, vol. 55, no. 2, pp. 1519–1565.

[6] M. Rodrigo, "Non-invasive identification of atrial fibrillation drivers."

[7] A. J. Graham, M. Orini, E. Zacur, G. Dhillon, H. Daw, N. T. Srinivasan, J. D. Lane, A. Cambridge, J. Garcia, N. J. O'Reilly, S. Whittaker-Axon, P. Taggart, M. Lowe, M. Finlay, M. J. Earley, A. Chow, S. Sporton, M. Dhinoja, R. J. Schilling, R. J. Hunter, and P. D. Lambiase, "Simultaneous Comparison of Electrocardiographic Imaging and Epicardial Contact Mapping in Structural Heart Disease," *Circulation: Arrhythmia and Electrophysiology*, vol. 12, no. 4, p. e007120.

[8] D. Ravì, C. Wong, F. Deligianni, M. Berthelot, J. Andreu-Perez, B. Lo, and G.-Z. Yang, "Deep Learning for Health Informatics," *IEEE journal of biomedical and health informatics*, vol. PP.

[9] K. Gregor and Y. LeCun, "Learning fast approximations of sparse coding," in *Proceedings of the 27th international conference on international conference on machine learning*, pp. 399–406, 2010.

[10] K. H. Jin, M. T. McCann, E. Froustey, and M. Unser, "Deep Convolutional Neural Network for Inverse Problems in Imaging," *IEEE Transactions on Image Processing*, vol. 26, no. 9, pp. 4509–4522.

[11] M. Cluitmans, D. H. Brooks, R. MacLeod, O. Dössel, M. S. Guillem, p. u. family=Dam, given=Peter M., J. Svehlikova, B. He, J. Sapp, L. Wang, and L. Bear, "Validation and Opportunities of Electrocardiographic Imaging: From Technical Achievements to Clinical Applications," *Frontiers in Physiology*, vol. 9.

[12] J. A. Bergquist, W. W. Good, B. Zenger, J. D. Tate, L. C. Rupp, and R. S. MacLeod, "The electrocardiographic forward problem: A benchmark study," *Computers in Biology and Medicine*, vol. 134, p. 104476.

[13] L. R. Bear, P. R. Huntjens, R. D. Walton, O. Bernus, R. Coronel, and R. Dubois, "Cardiac electrical dyssynchrony is accurately detected by noninvasive electrocardiographic imaging," *Heart Rhythm*, vol. 15, no. 7, pp. 1058–1069.

[14] W. H. Organization, "Cardiovascular diseases (cvds) fact sheet." `https://www.who.int/news-room/fact-sheets/detail/cardiovascular-diseases-(cvds)`. [Accessed: July 4, 2023].

[15] C. for Disease Control and Prevention, "Heart disease facts." `https://www.cdc.gov/heartdisease/facts.htm`. [Accessed: July 4, 2023].

[16] A. B. Parker III, B. F. Waller, and L. E. Gering, "Usefulness of the 12-lead electrocardiogram in detection of myocardial infarction: Electrocardiographic-anatomic correlations—Part II," *Clinical Cardiology*, vol. 19, no. 2, pp. 141–148.

[17] P. A. Friedman, "Novel mapping techniques for cardiac electrophysiology," *Heart*, vol. 87, no. 6, pp. 575–582.

[18] L. M. Miller and A. Gal, "Chapter 10 - Cardiovascular System and Lymphatic Vessels1," in *Pathologic Basis of Veterinary Disease (Sixth Edition)* (J. F. Zachary, ed.), pp. 561–616.e1, Mosby.

[19] V. Mahadevan, "Anatomy of the heart," *Surgery (Oxford)*, vol. 36, no. 2, pp. 43–47.

[20] N. C. for Biotechnology Information, "The heart - ncbi bookshelf." https://www.ncbi.nlm.nih.gov/books/NBK545195/#:~:text=The%20heart%20muscle%20is%20the,function%20of%20the%20cardiac%20pump., 2021. Accessed: July 12, 2023.

[21] R. H. Whitaker, "Anatomy of the heart," *Medicine*, vol. 38, no. 7, pp. 333–335.

[22] A. L. Hodgkin and A. F. Huxley, "A quantitative description of membrane current and its application to conduction and excitation in nerve," *The Journal of Physiology*, vol. 117, no. 4, pp. 500–544.

[23] G. W. Beeler and H. Reuter, "Reconstruction of the action potential of ventricular myocardial fibres," *The Journal of Physiology*, vol. 268, no. 1, pp. 177–210.

[24] C. H. Luo and Y. Rudy, "A model of the ventricular cardiac action potential. Depolarization, repolarization, and their interaction.," *Circulation Research*, vol. 68, no. 6, pp. 1501–1526.

[25] C. H. Luo and Y. Rudy, "A dynamic model of the cardiac ventricular action potential. I. Simulations of ionic currents and concentration changes," *Circulation Research*, vol. 74, no. 6, pp. 1071–1096.

[26] G. M. Faber and Y. Rudy, "Action Potential and Contractility Changes in [Na+]i Overloaded Cardiac Myocytes: A Simulation Study," *Biophysical Journal*, vol. 78, no. 5, pp. 2392–2404.

[27] P. Colli Franzone, L. Guerri, M. Pennacchio, and B. Taccardi, "Spread of excitation in 3-D models of the anisotropic cardiac tissue. II. Effects of fiber architecture and ventricular geometry," *Mathematical Biosciences*, vol. 147, no. 2, pp. 131–171.

[28] M. Seyedebrahimi, "Simulation of transmembrane potential propagation in three dimensional ventricular tissue using aliev panfilov model," Master's thesis, Middle East Technical University, 2015.

[29] J. Nagumo, S. Arimoto, and S. Yoshizawa, "An Active Pulse Transmission Line Simulating Nerve Axon," *Proceedings of the IRE*, vol. 50, no. 10, pp. 2061–2070.

[30] R. R. Aliev and A. V. Panfilov, "A simple two-variable model of cardiac excitation," *Chaos, Solitons & Fractals*, vol. 7, no. 3, pp. 293–301.

[31] D. Brooks and R. MacLeod, "Electrical imaging of the heart," *IEEE Signal Processing Magazine*, vol. 14, no. 1, pp. 24–42.

[32] I. Menown, G. Mackenzie, and A. Adgey, "Optimizing the initial 12-lead electrocardiographic diagnosis of acute myocardial infarction," *European Heart Journal*, vol. 21, no. 4, pp. 275–283.

[33] F. G. Yanowitz, G. M. Vincent, R. L. Lux, M. Merchant, L. S. Green, and J. Abildskov, "Application of body surface mapping to exercise testing: S-t80 isoarea maps in patients with coronary artery disease," *The American Journal of Cardiology*, vol. 50, no. 5, pp. 1109–1113, 1982.

[34] B. Taccardi, "Body surface mapping and cardiac electric sources: A historical survey," *Journal of electrocardiology*, vol. 23, pp. 150–154, 1990.

[35] B. Taccardi, B. B. Punske, R. L. Lux, R. S. MacLEOD, P. R. Ershler, T. J. Dustman, and Y. Vyhmeister, "Useful lessons from body surface mapping," *Journal of Cardiovascular Electrophysiology*, vol. 9, no. 7, pp. 773–786, 1998.

[36] M. R. Robinson and N. Curzen, "Electrocardiographic body surface mapping: potential tool for the detection of transient myocardial ischemia in the 21st century?," *Annals of Noninvasive Electrocardiology*, vol. 14, no. 2, pp. 201–210, 2009.

[37] J. Abildskov, M. Burgess, R. L. Lux, and R. F. Wyatt, "Experimental evidence for regional cardiac influence in body surface isopotential maps of dogs.," *Circulation research*, vol. 38, no. 5, pp. 386–391, 1976.

[38] H. Oguri, R. L. Lux, M. J. Burgess, R. F. Wyatt, and J. A. Abildskov, "Body surface distribution of QRS deflection areas in experimental ventricular preexcitation," *Journal of Electrocardiology*, vol. 13, no. 3, pp. 237–243.

[39] S. R. McMechan, G. MacKenzie, J. Allen, G. T. Wright, G. J. Dempsey, M. Crawley, J. Anderson, and A. A. J. Adgey, "Body surface ECG potential maps in acute myocardial infarction," *Journal of Electrocardiology*, vol. 28, pp. 184–190.

[40] Z. Cai, J. Li, K. Luo, X. Zhang, Y. Wang, and J. Zhang, "Design and experimental verification of a recording scheme for body surface potential mapping," in *2017 Chinese Automation Congress (CAC)*, pp. 3973–3976.

[41] R. C. Barr, M. S. Spach, and G. S. Herman-Giddens, "Selection of the Number and Positions of Measuring Locations for Electrocardiography," *IEEE Transactions on Biomedical Engineering*, vol. BME-18, no. 2, pp. 125–138.

[42] R. L. Lux, C. R. Smith, R. F. Wyatt, and J. Abildskov, "Limited lead selection for estimation of body surface potential maps in electrocardiography," *IEEE Transactions on Biomedical Engineering*, vol. BME-25, no. 3, pp. 270–276, 1978.

[43] L. Parreira, P. Carmo, P. Adragao, S. Nunes, A. Soares, R. Marinheiro, M. Budanova, S. Zubarev, M. Chmelevsky, J. Pinho, A. Ferreira, D. Cavaco, H. Marques, and P. A. Goncalves, "Electrocardiographic imaging (ECGI): What is the minimal number of leads needed to obtain a good spatial resolution?," *Journal of Electrocardiology*, vol. 62, pp. 86–93.

[44] J. Bergquist, L. Rupp, B. Zenger, J. Brundage, A. Busatto, and R. S. MacLeod, "Body Surface Potential Mapping: Contemporary Applications and Future Perspectives," *Hearts (Basel, Switzerland)*, vol. 2, no. 4, pp. 514–542.

[45] R. M. Gulrajani, "The forward and inverse problems of electrocardiography," *IEEE Engineering in Medicine and Biology Magazine*, vol. 17, no. 5, pp. 84–101, 1998.

[46] R. Gulrajani, *Bioelectricity and biomagnetism*. Wiley, 1998.

[47] "3D Navigation System | Biosense Webster."

[48] Y. Yamashita, "Theoretical Studies on the Inverse Problem in Electrocardiography and the Uniqueness of the Solution," *IEEE Transactions on Biomedical Engineering*, vol. BME-29, no. 11, pp. 719–725.

[49] Y. Kim and W. J. Tompkins, "Forward and inverse high-frequency electrocardiography," *Medical and Biological Engineering and Computing*, vol. 19, no. 1, pp. 11–22.

[50] C. L. Rogers and T. C. Pilkington, "Free-Moment Current Dipoles in Inverse Electrocardiography," *IEEE Transactions on Biomedical Engineering*, vol. BME-15, no. 4, pp. 312–323.

[51] R. O. Martin and T. C. Pilkington, "Unconstrained Inverse Electrocardiography: Epicardial Potentials," *IEEE Transactions on Biomedical Engineering*, vol. BME-19, no. 4, pp. 276–285.

[52] R. C. Barr, M. Ramsey, and M. S. Spach, "Relating Epicardial to Body Surface Potential Distributions by Means of Transfer Coefficients Based on Geometry Measurements," *IEEE Transactions on Biomedical Engineering*, vol. BME-24, no. 1, pp. 1–11.

[53] "A simulation study of the effects of torso inhomogeneities on electrocardiographic potentials, using realistic heart and torso models.."

[54] Y. S. Dogrusoz, N. Rasoolzadeh, B. Ondrusova, P. Hlivak, J. Zelinka, M. Tysler, and J. Svehlikova, "Comparison of dipole-based and potential-based ECGI methods for premature ventricular contraction beat localization with clinical data," *Frontiers in Physiology*, vol. 14.

[55] S. Schuler, M. Schaufelberger, L. R. Bear, J. A. Bergquist, M. J. M. Cluitmans, J. Coll-Font, O. N. Onak, B. Zenger, A. Loewe, R. S. MacLeod, D. H. Brooks, and O. Dossel, "Reducing Line-of-block Artifacts in Cardiac Activation Maps Estimated Using ECG Imaging: A Comparison of Source Models and Estimation Methods," *IEEE Transactions on Biomedical Engineering*, vol. 69, no. 6, pp. 2041–2052.

[56] R. Doste, R. Sebastian, J. F. Gomez, D. Soto-Iglesias, A. Alcaine, L. Mont, A. Berruezo, D. Penela, and O. Camara, "In silico pace-mapping: Prediction of left vs. right outflow tract origin in idiopathic ventricular arrhythmias with patient-specific electrophysiological simulations," *Europace: European Pacing, Arrhythmias, and Cardiac Electrophysiology: Journal of the Working*

Groups on Cardiac Pacing, Arrhythmias, and Cardiac Cellular Electrophysiology of the European Society of Cardiology, vol. 22, no. 9, pp. 1419–1430.

[57] R. Plonsey and D. B. Heppner, "Considerations of quasi-stationarity in electrophysiological systems," *The bulletin of mathematical biophysics*, vol. 29, no. 4, pp. 657–664.

[58] R. MacLeod and D. Brooks, "Recent progress in inverse problems in electrocardiology," *IEEE Engineering in Medicine and Biology Magazine*, vol. 17, no. 1, pp. 73–83.

[59] M. Liaskos, M. A. Savelonas, P. A. Asvestas, M. G. Lykissas, and G. K. Matsopoulos, "Bimodal CT/MRI-Based Segmentation Method for Intervertebral Disc Boundary Extraction," *Information*, vol. 11, no. 9, p. 448.

[60] K.Pradeep and C.Narayanan, "Segmentation of Fused CT and MRI Images with Brain Tumor," *International Journal of Engineering Research & Technology*, vol. 1, no. 6.

[61] M. Fernández-Corazza, L. Beltrachini, N. Von Ellenrieder, and C. H. Muravchik, "Analysis of parametric estimation of head tissue conductivities using electrical impedance tomography," *Biomedical Signal Processing and Control*, vol. 8, no. 6, pp. 830–837, 2013.

[62] J. K. Seo, O. Kwon, and E. J. Woo, "Magnetic resonance electrical impedance tomography (mreit): conductivity and current density imaging," in *Journal of Physics: Conference Series*, vol. 12, p. 140, IOP Publishing, 2005.

[63] R. J. Halter, A. Hartov, J. A. Heaney, K. D. Paulsen, and A. R. Schned, "Electrical impedance spectroscopy of the human prostate," *IEEE Transactions on Biomedical Engineering*, vol. 54, no. 7, pp. 1321–1327, 2007.

[64] D. Dean, T. Ramanathan, D. Machado, and R. Sundararajan, "Electrical impedance spectroscopy study of biological tissues," *Journal of electrostatics*, vol. 66, no. 3-4, pp. 165–177, 2008.

[65] B. Milan Horáček and J. C. Clements, "The inverse problem of electrocardiography: A solution in terms of single- and double-layer sources on the epicardial surface," *Mathematical Biosciences*, vol. 144, no. 2, pp. 119–154.

[66] Y. Wang and Y. Rudy, "Application of the method of fundamental solutions to potential-based inverse electrocardiography," *Annals of biomedical engineering*, vol. 34, pp. 1272–1288, 2006.

[67] O. Bouhamama, M. Potse, L. Bear, and L. Weynans, "A Patchwork Method to Improve the Performance of Current Methods for Solving the Inverse Problem of Electrocardiography," *IEEE Transactions on Biomedical Engineering*, vol. 70, no. 1, pp. 55–66.

[68] M. Seger, G. Fischer, R. Modre, B. Messnarz, F. Hanser, and B. Tilg, "Lead field computation for the electrocardiographic inverse problem—finite elements versus boundary elements," *Computer Methods and Programs in Biomedicine*, vol. 77, no. 3, pp. 241–252.

[69] H. Antes, "A Short Course on Boundary Element Methods,"

[70] "How Accurate Is Inverse Electrocardiographic Mapping?."

[71] J. Salinet, R. Molero, F. S. Schlindwein, J. Karel, M. Rodrigo, J. L. Rojo-Álvarez, O. Berenfeld, A. M. Climent, B. Zenger, F. Vanheusden, J. G. S. Paredes, R. MacLeod, F. Atienza, M. S. Guillem, M. Cluitmans, and P. Bonizzi, "Electrocardiographic Imaging for Atrial Fibrillation: A Perspective From Computer Models and Animal Experiments to Clinical Value," *Frontiers in Physiology*, vol. 12.

[72] C. Ramanathan, P. Jia, R. Ghanem, D. Calvetti, and Y. Rudy, "Noninvasive Electrocardiographic Imaging (ECGI): Application of the Generalized Minimal Residual (GMRes) Method," *Annals of Biomedical Engineering*, vol. 31, no. 8, pp. 981–994.

[73] M. Milanic, V. Jazbinsek, g.-i. family=Wang, given=DF, J. Sinstra, g.-i. family=MacLeod, given=RS, g.-i. family=Brooks, given=DH, and R. Hren, "Evaluation of approaches to solving electrocardiographic imaging problem," in *2009 36th Annual Computers in Cardiology Conference (CinC)*, pp. 177–180.

[74] D. L. Young, C. C. Tsai, C. W. Chen, and C. M. Fan, "The method of fundamental solutions and condition number analysis for inverse problems

of Laplace equation," *Computers & Mathematics with Applications*, vol. 55, no. 6, pp. 1189–1200.

[75] J. A. Bergquist, B. Zenger, W. W. Good, L. C. Rupp, L. R. Bear, and R. S. MacLeod, "Novel Experimental Preparation to Assess Electrocardiographic Imaging Reconstruction Techniques," in *2020 Computing in Cardiology*, pp. 1–4.

[76] Ö. N. Onak and Y. S. Doğrusöz, "Performance of tikhonov regularization with different constraints in electrocardiographic imaging," in *2020 28th Signal Processing and Communications Applications Conference (SIU)*, pp. 1–4, IEEE, 2020.

[77] S. Ghosh and Y. Rudy, "Application of L1-norm regularization to epicardial potential solution of the inverse electrocardiography problem," *Annals of Biomedical Engineering*, vol. 37, no. 5, pp. 902–912.

[78] P. C. Hansen, *Rank-deficient and discrete ill-posed problems: numerical aspects of linear inversion*. SIAM, 1998.

[79] Y. S. Dogrusoz, "Statistical estimation applied to electrocardiographic imaging," in *2019 12th International Conference on Measurement*, pp. 2–9, IEEE, 2019.

[80] D. P. O'Leary and J. A. Simmons, "A bidiagonalization-regularization procedure for large scale discretizations of ill-posed problems," *SIAM Journal on Scientific and Statistical Computing*, vol. 2, no. 4, pp. 474–489, 1981.

[81] Y. Saad and M. H. Schultz, "Gmres: A generalized minimal residual algorithm for solving nonsymmetric linear systems," *SIAM Journal on scientific and statistical computing*, vol. 7, no. 3, pp. 856–869, 1986.

[82] M. Jiang, L. Xia, G. Shou, and M. Tang, "Combination of the LSQR method and a genetic algorithm for solving the electrocardiography inverse problem," *Physics in Medicine & Biology*, vol. 52, no. 5, p. 1277.

[83] G. Shou, L. Xia, M. Jiang, Q. Wei, F. Liu, and S. Crozier, "Truncated Total Least Squares: A New Regularization Method for the Solution of ECG

Inverse Problems," *IEEE Transactions on Biomedical Engineering*, vol. 55, no. 4, pp. 1327–1335.

[84] A. N. Tikhonov and V. I. A. Arsenin, "Solutions of Ill-Posed Problems," *Halsted*, 1977.

[85] O. Onak and Y. S. Dogrusoz, "Performance of Tikhonov Regularization with Different Constraints in Electrocardiographic Imaging," in *2020 28th Signal Processing and Communications Applications Conference (SIU)*, pp. 1–4.

[86] R. Molero, J. Reventós-Presmanes, I. Roca, L. Mont, A. M. Climent, and M. S. Guillem, "Impact of noise on electrocardiographic imaging resolution with zero order tikhonov regularization and l-curve optimization," in *2022 Computing in Cardiology (CinC)*, vol. 498, pp. 1–4, IEEE, 2022.

[87] T. Oostendorp, A. Oosterom, and G. Huiskamp, "Interpolation on a triangulated 3D surface," *Journal of Computational Physics*, vol. 80, pp. 331–343.

[88] J. Kaipio and S. Erkki, *Statistical and Computational Inverse Problems*. Springer, 2004.

[89] Y. Serinagaoglu, D. H. Brooks, and R. S. MacLeod, "Bayesian solutions and performance analysis in bioelectric inverse problems," *IEEE Transactions on Biomedical Engineering*, vol. 52, no. 6, pp. 1009–1020, 2005.

[90] Y. Serinagaoglu, D. H. Brooks, and R. S. MacLeod, "Improved performance of Bayesian solutions for inverse electrocardiography using multiple information sources," *IEEE Transactions on Biomedical Engineering*, vol. 53, no. 10, pp. 2024–2034, 2006.

[91] J. C. Mosher, M. E. Spencer, R. M. Leahy, and P. S. Lewis, "Error bounds for EEG and MEG dipole source localization," *Electroensephalography and Clinical Neurophysiology*, vol. 86, pp. 303–321, 1993.

[92] G. Russell, R. Srinivasan, and D. Tucker, "Bayesian estimates of error bounds for EEG source imaging," *IEEE Transactions on Medical Imaging*, vol. 17, no. 6, pp. 1084–1089.

[93] C. H. Muravchik and A. Nehorai, "EEG/MEG error bounds for a static dipole source with a realistic head model," *IEEE Trans. on Sig. Proc.*, vol. 49, no. 3, pp. 470–484, 2001.

[94] S. M. Kay, *Fundamentals of Statistical Signal Processing: Estimation Theory*, ch. 10-12. New Jersey, USA: Prentice-Hall, Inc., 1993.

[95] L. Wang, K. C. Wong, H. Zhang, H. Liu, and P. Shi, "Noninvasive Computational Imaging of Cardiac Electrophysiology for 3-D Infarct," *IEEE Transactions on Biomedical Engineering*, vol. 58, no. 4, pp. 1033–1043.

[96] T. Erenler and Y. S. Doğrusöz, "A Learning Based Statistical Approach for Combining Multiple Measurements in Electrocardiographic Imaging," in *2018 Computing in Cardiology Conference (CinC)*, vol. 45, pp. 1–4.

[97] Y. S. Dogrusoz, "Statistical Estimation Applied to Electrocardiographic Imaging," in *2019 12th International Conference on Measurement*, pp. 2–9.

[98] Y. Goussard, D. Joly, and P. Savard, "Time-Recursive Solution to the Inverse Problem of Electrocardiography,"

[99] D. Brooks, G. Ahmad, R. MacLeod, and G. Maratos, "Inverse electrocardiography by simultaneous imposition of multiple constraints," *IEEE Transactions on Biomedical Engineering*, vol. 46, no. 1, pp. 3–18.

[100] F. Greensite, "The temporal prior in bioelectromagnetic source imaging problems," *IEEE Transactions on Biomedical Engineering*, vol. 50, no. 10, pp. 1152–1159.

[101] J. A. Bergquist, J. Coll-Font, B. Zenger, L. C. Rupp, W. W. Good, D. H. Brooks, and R. S. MacLeod, "Simultaneous Multi-heartbeat ECGI Solution with a Time-Varying Forward Model: A Joint Inverse Formulation," in *Functional Imaging and Modeling of the Heart* (D. B. Ennis, L. E. Perotti, and V. Y. Wang, eds.), Lecture Notes in Computer Science, pp. 493–502, Springer International Publishing.

[102] M. J. M. Cluitmans, R. L. M. Peeters, P. G. A. Volders, and R. L. Westra, "Realistic training data improve noninvasive reconstruction of heart-surface

potentials," in *2012 Annual International Conference of the IEEE Engineering in Medicine and Biology Society*, pp. 6373–6376.

[103] Y. Serinagaoglu and U. Aydin, "Imaging the electrical activity of the heart using a Kalman filter based approach: Comparison of results using different STM's," in *2009 IEEE International Symposium on Biomedical Imaging: From Nano to Macro*, pp. 153–156.

[104] Y. S. Dogrusoz and T. Erenler, "Use of Simulated Data for the Estimation of Prior Models in Kalman Filter-Based ECGI," in *2020 Computing in Cardiology*, pp. 1–4.

[105] T. Erenler and Y. S. Dogrusoz, "Effects of Prior Data on the Inference and Filtering Based Electrocardiographic Imaging," in *2019 Computing in Cardiology (CinC)*, pp. Page 1–Page 4.

[106] E. Ozkoc, E. Sunger, K. Ugurlu, and Y. S. Dogrusoz, "Prior Model Selection in Bayesian MAP Estimation-Based ECG Reconstruction," in *2021 13th International Conference on Measurement*, pp. 142–145.

[107] M. N. Wernick, Y. Yang, J. G. Brankov, G. Yourganov, and S. C. Strother, "Machine Learning in Medical Imaging," *IEEE Signal Processing Magazine*, vol. 27, no. 4, pp. 25–38.

[108] R. Tenderini, S. Pagani, A. Quarteroni, and S. Deparis, "PDE-Aware Deep Learning for Inverse Problems in Cardiac Electrophysiology," *SIAM Journal on Scientific Computing*, vol. 44, no. 3, pp. B605–B639.

[109] H. Yu, L. T. Yang, Q. Zhang, D. Armstrong, and M. J. Deen, "Convolutional neural networks for medical image analysis: State-of-the-art, comparisons, improvement and perspectives," *Neurocomputing*, vol. 444, pp. 92–110.

[110] N. Tajbakhsh, J. Y. Shin, S. R. Gurudu, R. T. Hurst, C. B. Kendall, M. B. Gotway, and J. Liang, "Convolutional Neural Networks for Medical Image Analysis: Full Training or Fine Tuning?," *IEEE Transactions on Medical Imaging*, vol. 35, no. 5, pp. 1299–1312.

[111] X.-M. Zhang, L. Liang, L. Liu, and M.-J. Tang, "Graph Neural Networks and Their Current Applications in Bioinformatics," *Frontiers in Genetics*, vol. 12.

[112] A. Dosovitskiy, L. Beyer, A. Kolesnikov, D. Weissenborn, X. Zhai, T. Unterthiner, M. Dehghani, M. Minderer, G. Heigold, S. Gelly, J. Uszkoreit, and N. Houlsby, "An Image is Worth 16x16 Words: Transformers for Image Recognition at Scale."

[113] E. U. Henry, O. Emebob, and C. A. Omonhinmin, "Vision Transformers in Medical Imaging: A Review."

[114] S. Nabavi, A. Ejmalian, M. E. Moghaddam, A. A. Abin, A. F. Frangi, M. Mohammadi, and H. S. Rad, "Medical imaging and computational image analysis in COVID-19 diagnosis: A review," *Computers in Biology and Medicine*, vol. 135, p. 104605.

[115] M. T. McCann, K. H. Jin, and M. Unser, "Convolutional Neural Networks for Inverse Problems in Imaging: A Review," *IEEE Signal Processing Magazine*, vol. 34, no. 6, pp. 85–95.

[116] K. Zhang, W. Zuo, Y. Chen, D. Meng, and L. Zhang, "Beyond a Gaussian Denoiser: Residual Learning of Deep CNN for Image Denoising," *IEEE Transactions on Image Processing*, vol. 26, no. 7, pp. 3142–3155.

[117] K. Schawinski, C. Zhang, H. Zhang, L. Fowler, and G. K. Santhanam, "Generative adversarial networks recover features in astrophysical images of galaxies beyond the deconvolution limit," *Monthly Notices of the Royal Astronomical Society: Letters*, vol. 467, no. 1, pp. L110–L114.

[118] D. Li and Z. Wang, "Video Superresolution via Motion Compensation and Deep Residual Learning," *IEEE Transactions on Computational Imaging*, vol. 3, no. 4, pp. 749–762.

[119] S. U. Dar, M. Yurt, M. Shahdloo, M. E. Ildiz, B. Tinaz, and T. Çukur, "Prior-Guided Image Reconstruction for Accelerated Multi-Contrast MRI via Generative Adversarial Networks," *IEEE Journal of Selected Topics in Signal Processing*, vol. 14, no. 6, pp. 1072–1087.

[120] D. Liang, J. Cheng, Z. Ke, and L. Ying, "Deep Magnetic Resonance Image Reconstruction: Inverse Problems Meet Neural Networks," *IEEE Signal Processing Magazine*, vol. 37, no. 1, pp. 141–151.

[121] M. Zhang, S. Gu, and Y. Shi, "The use of deep learning methods in low-dose computed tomography image reconstruction: a systematic review," *Complex & intelligent systems*, vol. 8, no. 6, pp. 5545–5561, 2022.

[122] M. Genzel, I. Gühring, J. Macdonald, and M. März, "Near-exact recovery for tomographic inverse problems via deep learning," in *International Conference on Machine Learning*, pp. 7368–7381, PMLR, 2022.

[123] A. Coxson, I. Mihov, Z. Wang, V. Avramov, F. B. Barnes, S. Slizovskiy, C. Mullan, I. Timokhin, D. Sanderson, A. Kretinin, *et al.*, "Machine learning enhanced electrical impedance tomography for 2d materials," *Inverse Problems*, vol. 38, no. 8, p. 085007, 2022.

[124] G. Xu, B. Zhang, H. Yu, J. Chen, M. Xing, and W. Hong, "Sparse synthetic aperture radar imaging from compressed sensing and machine learning: Theories, applications, and trends," *IEEE Geoscience and Remote Sensing Magazine*, vol. 10, no. 4, pp. 32–69, 2022.

[125] B. M. Afkham, J. Chung, and M. Chung, "Learning regularization parameters of inverse problems via deep neural networks," *Inverse Problems*, vol. 37, no. 10, p. 105017.

[126] J. Whang, E. Lindgren, and A. Dimakis, "Composing Normalizing Flows for Inverse Problems," in *Proceedings of the 38th International Conference on Machine Learning*, pp. 11158–11169, PMLR.

[127] A. Bora, A. Jalal, E. Price, and A. G. Dimakis, "Compressed Sensing using Generative Models," in *Proceedings of the 34th International Conference on Machine Learning*, pp. 537–546, PMLR.

[128] Y. Song, L. Shen, L. Xing, and S. Ermon, "Solving Inverse Problems in Medical Imaging with Score-Based Generative Models," 6 2022. arXiv:2111.08005.

[129] M. Duff, N. D. F. Campbell, and M. J. Ehrhardt, "Regularising Inverse Problems with Generative Machine Learning Models," 6 2022. arXiv:2107.11191.

[130] C. Luo, "Understanding Diffusion Models: A Unified Perspective."

[131] J. Ho, A. Jain, and P. Abbeel, "Denoising Diffusion Probabilistic Models," in *Advances in Neural Information Processing Systems*, vol. 33, pp. 6840–6851, Curran Associates, Inc.

[132] B. Song, S. M. Kwon, Z. Zhang, X. Hu, Q. Qu, and L. Shen, "Solving Inverse Problems with Latent Diffusion Models via Hard Data Consistency," 7 2023. arXiv:2307.08123.

[133] H. Chung, B. Sim, D. Ryu, and J. C. Ye, "Improving Diffusion Models for Inverse Problems using Manifold Constraints," *Advances in Neural Information Processing Systems*, vol. 35, pp. 25683–25696.

[134] H. Chung, B. Sim, and J. C. Ye, "Come-Closer-Diffuse-Faster: Accelerating Conditional Diffusion Models for Inverse Problems Through Stochastic Contraction," pp. 12413–12422, 2022. Proceedings of the IEEE/CVF Conference on Computer Vision and Pattern Recognition.

[135] H. Chung and J. C. Ye, "Score-based diffusion models for accelerated MRI," *Medical Image Analysis*, vol. 80, p. 102479.

[136] A. Güngör, S. U. Dar, Ş. Öztürk, Y. Korkmaz, H. A. Bedel, G. Elmas, M. Ozbey, and T. Çukur, "Adaptive diffusion priors for accelerated mri reconstruction," *Medical Image Analysis*, p. 102872, 2023.

[137] T. Bacoyannis, B. Ly, N. Cedilnik, H. Cochet, and M. Sermesant, "Deep learning formulation of electrocardiographic imaging integrating image and signal information with data-driven regularization," *EP Europace*, vol. 23, no. Supplement_1, pp. i55–i62, 2021.

[138] N. Pilia, S. Schuler, M. Rees, G. Moik, D. Potyagaylo, O. Dössel, and A. Loewe, "Non-invasive localization of the ventricular excitation origin without patient-specific geometries using deep learning," *Artificial Intelligence in Medicine*, p. 102619.

[139] S. Schuler, N. Pilia, D. Potyagaylo, and A. Loewe, "Cobiveco: Consistent biventricular coordinates for precise and intuitive description of position in the heart – with MATLAB implementation," *Medical Image Analysis*, vol. 74, p. 102247.

[140] K.-W. Chen, L. Bear, and C.-W. Lin, "Solving Inverse Electrocardiographic Mapping Using Machine Learning and Deep Learning Frameworks," *Sensors*, vol. 22, no. 6, p. 2331.

[141] X. Jiang, S. Ghimire, J. Dhamala, Z. Li, P. K. Gyawali, and L. Wang, "Learning Geometry-Dependent and Physics-Based Inverse Image Reconstruction," in *Medical Image Computing and Computer Assisted Intervention – MICCAI 2020* (A. L. Martel, P. Abolmaesumi, D. Stoyanov, D. Mateus, M. A. Zuluaga, S. K. Zhou, D. Racoceanu, and L. Joskowicz, eds.), Lecture Notes in Computer Science, pp. 487–496, Springer International Publishing.

[142] X. Jiang, J. Tate, J. Bergquist, A. Narayan, R. MacLeod, and L. Wang, "Uncertainty Quantification of Cardiac Position on Deep Graph Network ECGI," in *2022 Computing in Cardiology (CinC)*, vol. 498, pp. 1–4.

[143] X. Jiang, M. Toloubidokhti, J. Bergquist, B. Zenger, W. W. Good, R. S. MacLeod, and L. Wang, "Improving Generalization by Learning Geometry-Dependent and Physics-Based Reconstruction of Image Sequences," *IEEE Transactions on Medical Imaging*, vol. 42, no. 2, pp. 403–415.

[144] J. A. Bergquist, W. W. Good, B. Zenger, J. D. Tate, and R. S. MacLeod, "Optimizing the Reconstruction of Cardiac Potentials Using a Novel High Resolution Pericardiac Cage," in *2019 Computing in Cardiology (CinC)*, pp. 1–4.

[145] M. J. M. Cluitmans, P. Bonizzi, J. M. H. Karel, M. Das, B. L. J. H. Kietselaer, J. M. M. J. de, F. W. Prinzen, R. L. M. Peeters, R. L. Westra, and P. G. A. Volders, "In Vivo Validation of Electrocardiographic Imaging," *JACC: Clinical Electrophysiology*, vol. 3, no. 3, pp. 232–242.

[146] M. Cluitmans, D. H. Brooks, R. MacLeod, O. Dössel, M. S. Guillem, p. u. family=Dam, given=Peter M., J. Svehlikova, B. He, J. Sapp, L. Wang, and L. Bear, "Validation and Opportunities of Electrocardiographic Imaging: From Technical Achievements to Clinical Applications," *Frontiers in Physiology*, vol. 9.

[147] K. Bujnarowski, P. Bonizzi, M. Cluitmans, R. Peeters, and J. Karel, "CT-Scan Free Neural Network-Based Reconstruction of Heart Surface Potentials From ECG Recordings," in *2020 Computing in Cardiology*, pp. 1–4.

[148] M. H. Jarrahi, A. Memariani, and S. Guha, "The Principles of Data-Centric AI (DCAI)," 11 2022. arXiv:2211.14611.

[149] R. MacLeod, B. Taccardi, and R. Lux, "Electrocardiographic mapping in a realistic torso tank preparation," in *Proceedings of 17th International Conference of the Engineering in Medicine and Biology Society*, vol. 1, pp. 245–246 vol.1.

[150] A. Wirgin, "The inverse crime," 1 2004. arXiv:math-ph/0401050.

[151] P. C. Stanley, T. C. Pilkington, and M. N. Morrow, "The Effects of Thoracic Inhomogeneities on the Relationship Between Epicardial and Torso Potentials," *IEEE Transactions on Biomedical Engineering*, vol. BME-33, no. 3, pp. 273–284, 1986.

[152] C. Ramanathan and Y. Rudy, "Electrocardiographic imaging: II. Effect of torso inhomogeneities on noninvasive reconstruction of epicardial potentials, electrograms, and isochrones," *Journal of Cardiovascular Electrophysiology*, vol. 12, no. 2, pp. 241–252, 2001.

[153] B. Erem, J. Coll-Font, R. M. Orellana, P. Stovícek, and D. H. Brooks, "Using transmural regularization and dynamic modeling for noninvasive cardiac potential imaging of endocardial pacing with imprecise thoracic geometry," *IEEE transactions on medical imaging*, vol. 33, no. 3, pp. 726–738.

[154] J. Duchateau, M. Potse, and R. Dubois, "Spatially Coherent Activation Maps for Electrocardiographic Imaging," *IEEE Transactions on Biomedical Engineering*, vol. 64, no. 5, pp. 1149–1156.

[155] K. Ugurlu, "Graphical user interface for the computation and visualization of the cardiac activation times," in *31st IEEE Conference on Signal Processing and Communications Applications*, pp. 1–4, IEEE, 2023.

[156] U. Aydin and Y. Serinagaoglu, "A kalman filter based approach to reduce the effects of geometric errors and the measurement noise in the inverse ECG problem," *Med Biol Eng Comput.*, vol. 49, no. 9, pp. 1003–1013, 2011.

[157] T. Erenler and Y. Serinagaoglu, "A learning based statistical approach for combining multiple measurements in electrocardiographic imaging," in *Computing in Cardiology*, 2018.

[158] S. Wold, K. Esbensen, and P. Geladi, "Principal component analysis," *Chemometrics and intelligent laboratory systems*, vol. 2, no. 1-3, pp. 37–52, 1987.

[159] D. Zoran and Y. Weiss, "From learning models of natural image patches to whole image restoration," in *2011 International Conference on Computer Vision*, pp. 479–486.

[160] K. Zhang, W. Zuo, S. Gu, and L. Zhang, "Learning Deep CNN Denoiser Prior for Image Restoration," pp. 3929–3938, 2017. Proceedings of the IEEE Conference on Computer Vision and Pattern Recognition.

[161] O. Ronneberger, P. Fischer, and T. Brox, "U-net: Convolutional networks for biomedical image segmentation," in *International Conference on Medical image computing and computer-assisted intervention*, pp. 234–241, Springer, 2015.

[162] J. Chamorro-Servent, R. Dubois, M. Potse, and Y. Coudière, "Improving the Spatial Solution of Electrocardiographic Imaging: A New Regularization Parameter Choice Technique for the Tikhonov Method," in *Functional Imaging and Modelling of the Heart* (M. Pop and G. A. Wright, eds.), Lecture Notes in Computer Science, pp. 289–300, Springer International Publishing.

[163] A. Paszke, S. Gross, F. Massa, A. Lerer, J. Bradbury, G. Chanan, T. Killeen, Z. Lin, N. Gimelshein, L. Antiga, A. Desmaison, A. Köpf, E. Yang, Z. DeVito, M. Raison, A. Tejani, S. Chilamkurthy, B. Steiner, L. Fang, J. Bai, and S. Chintala, "Pytorch: An imperative style, high-performance deep learning library," 2019.